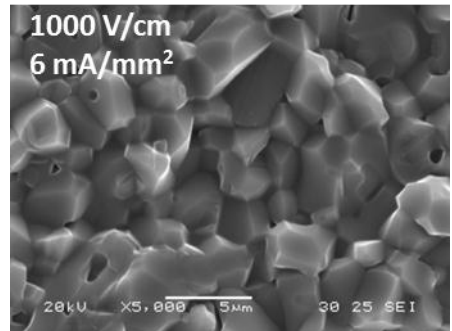
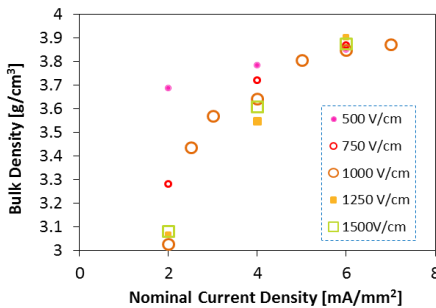
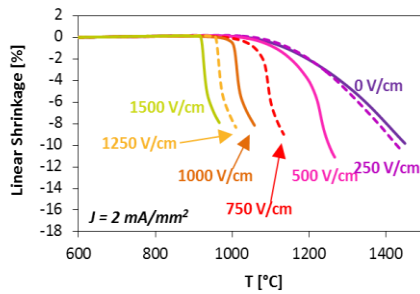




Doctoral School in Materials, Mechatronics
and Systems Engineering

Flash Sintering of Alumina-based Ceramics

Mattia Biesuz



FLASH SINTERING OF ALUMINA-BASED CERAMICS

Name

E-mail: mattia.biesuz@unitn.it

Approved by:

Prof. Vincenzo M. Sglavo, Advisor
Department of Industrial Engineering
University of Trento, Italy

Ph.D. Commission:

Prof. Giandomenico Sorarù,
Department of Industrial Engineering
University of Trento, Italy.

Prof. Rodrigo Moreno,
Instituto de Ceramica y Vidrio
Spain.

Prof. Enrico Bernardo,
Department of Industrial Engineering
University of Padova, Country.

University of Trento,
Department of Industrial Engineering

April 2017

University of Trento - Department of Industrial Engineering

Doctoral Thesis

Mattia Biesuz - 2017

Published in Trento (Italy) – by University of Trento

To my uncle Giancarlo

Abstract

Flash sintering is an electrical field-assisted consolidation technology and represents a very novel technique for producing ceramic materials, which allows to decrease sensibly both processing temperature and time. Starting from 2010, when flash sintering was discovered, different ceramic materials with a wide range of electrical properties have been successfully densified.

Up to date, the research on flash sintering has been mainly focused on ionic and electronic conductors and on semiconductor ceramics. In the present work, we studied the flash sintering behavior of a resistive technical ceramic like alumina also in the presence of magnesia silicate glass phase typically used for activating liquid phase sintering. The materials were studied by using different combinations of electric field and current density. Physical, structural and microstructural properties of sintered samples were extensively investigated by Archimedes' method, SEM, XRD, XPS and photoluminescence spectroscopy. Light emission and electrical behavior during the flash process were studied, as well.

The results point out the applicability of flash sintering to alumina and glass-containing alumina using electrical-field in excess of 500 V/cm, allowing an almost complete densification at temperatures lower than 1000°C. Different densification mechanisms were pointed out in the two systems, namely "solid state flash sintering" and "liquid phase flash sintering" for pure alumina and glass containing alumina, respectively. The glass addition allows a significant reduction of the current and power dissipation needed for densification, by promoting liquid phase sintering.

The results suggest that unconventional mass transport phenomena are activated by the current flow in the ceramic body and they can be very likely attributed to partial reduction of the oxide induced by the electrical current. The hypothesis that the oxide

gets partially reduced during DC-flash sintering experiments is supported by several experimental findings.

Finally, strong affinities between flash sintering and other physical processes, like dielectric breakdown, were pointed out.

Table of contents

Abstract	i
Table of contents	iii
1 Introduction	9
1.1 Sintering of ceramics	9
1.2 Flash sintering principles	11
1.3 Proposed mechanisms for flash sintering	18
1.4 Flash sintering: Phenomenology	22
1.4.1 Thermal runaway and Joule heating	22
1.4.2 Sintering and microstructures	33
1.4.3 Electrical behavior	40
1.4.4 Light emission	42
1.4.5 Textures and new phases	44
1.5 Materials densified by flash sintering	45
1.6 Flash sintering and related technologies	48
1.6.1 Flash sintering of tape casted layers	48
1.6.2 Travelling electrodes	49
1.6.3 Hyper-flash and double flash	49
1.6.4 Contactless Flash Sintering (CFS)	50
1.6.5 Flash Spark Plasma Sintering (FSPS)	51
1.6.6 Field-Assisted Sintering Technique (FAST)	53
1.6.7 Flash reactions	54
2 Aim of the work	56
3 Experimental procedures	57
3.1 Materials and samples preparation	57
3.2 Experimental set-up n. 1	59
3.3 Experimental set-up n. 2	60
3.4 Conventional Sintering	62
3.5 Characterization	62
3.5.1 Microstructure	62
3.5.2 Phase analysis	62
3.5.3 Density measurement	62

3.5.4 XPS 63	
3.5.5 Photoluminescence spectroscopy.....	63
4 Results and Discussion	64
4.1 Flash sintering of alumina	64
4.1.1 Densification behavior and microstructural evolution.....	64
4.1.2 Electrical behavior	78
4.1.3 Photoemission during Flash Sintering	106
4.1.4 Flash Sintering and Dielectric Breakdown.....	115
4.1.5 Electrode Material Effect	123
4.2 Flash sintering of glass-containing alumina.....	130
4.2.1 Densification behavior and Microstructural Evolution	130
4.2.2 Electrical behavior and onset for flash sintering	141
5 Conclusions	157
6 Future Perspectives.....	159
List of abbreviation and acronyms	160
References.....	161
Scientific Production	175
Participation to Congresses, Schools and Workshops	177
Teaching Activities	179

1 Introduction

1.1 Sintering of ceramics

Ceramics are inorganic, non-metallic materials characterized by unique combination of physical, mechanical, thermal and functional properties. In general, they are lighter and harder than metals, more resistant at high temperatures, to creep, to wear and to corrosion. Despite their inherent brittleness, they can be toughened and are characterized by high stiffness and mechanical strength, finding many structural applications, from buildings to refractories, from aerospace industry to cutting tools etc.. In the last decades great interest has also been risen by functional ceramics for their outstanding piezoelectric, electrical, magnetic and biological properties[1,2].

Different processing routes have been developed for obtaining ceramic materials; for example, coatings can be obtained via CVD, PVD, TRD, sputtering methods; porous ceramics can be processed from sol-gel, xerogel, aerogel techniques. However, the production of bulk ceramic is much more complicated. In fact, ceramics are brittle, hard and characterized by high melting temperature thus they can not be casted (with the exception of some ZAS refractories) or easily machined by plastic deformation or cheap removal. For all these reasons, ceramic materials manufacturing involves powder shaping and a high temperature powder consolidation process, called sintering[3]. The firing process is crucial when discussing about ceramics; in fact, controlling the firing parameters (time, temperature, atmosphere) it is possible to change the final properties of the sintered body: relative density, mechanical strength, toughness, grain size, electrical, magnetic and functional properties[2,3].

Sintering is a process based on diffusion, and therefore needs high temperatures and quite long time (in the order of hours) [3]. Indeed, the firing temperature depends from the composition of the material; it ranges between 800 - 1300°C for traditional ceramics (bricks, porcelain, earthenware...) but could reach temperature up to 1900°C for several advanced ceramics. Therefore, sintering is characterized by high costs, which are both economic and environmental.

In 2007, the European Commission approved a " Reference Document on Best Available Techniques in the Ceramic Manufacturing Industry"[4]. In this work, the

consumption for different class of ceramics is summarized. In all the cases, some MJ are needed for each kg of final product as shown in Table I. One should consider that the main part of the energy is consumed during the sintering process; i.e. considering the production of MgO refractory 3.0-6.3 MJ/kg are needed only for firing, while the overall energy consumption lays between 3.5-7.15 MJ/kg [4].

Today the larger part of energy required for the firing process is provided by the combustion of “natural gas, liquefied petroleum gas (propane and butane) and fuel oil EL ...; while heavy fuel oil, liquefied natural gas (LNG), biogas/biomass, electricity and solid fuels (e.g. coal, petroleum coke) can also play a role as energy sources for burners”[4]. The energy cost of natural gas is around 0.1 €/kWh, that means that the firing process requires 0.05 - 0.2 € for kg of ceramic. These values seems to be quite low but one should consider that only in Italy the refractory production in 2011 was 486,336 tons and the production of tableware was 13,200 [5]. Hence, the energy cost for refractory production in Italy can be estimated in the order of several millions of euros. This value is only referred to the energy cost, the actual cost of the firing process should account also for plant cost and maintenance. Typically the price of a tunnel kiln for porcelain/tableware is in the order of 500,000-1,000,000 €.

Therefore, it is crucial, both for economic and environmental reasons, to explore new ways for reducing sintering time and temperature of ceramics. Among the different possibilities field-assisted sintering in general, and flash sintering in particular, represents a very promising route.

Table I: Energy consumption for manufacturing different class of ceramics [4].

Material	Energy Consumption [MJ/kg]
Roof Tiles	1.90 - 2.95
Masonry Bricks	1.50 - 2.50
Porcelain Tableware	4.50 - 7.00
Vitrified Clay Pipes	6.19 - 7.86
MgO refractories	3.50- 7.15

1.2 Flash sintering principles

Flash Sintering (FS) is a consolidation technology which allows to reduce the temperature needed for densifying ceramics by hundreds of degrees [6,7]. In some cases the reduction of the firing temperature approaches 1000°C[8,9]. Additionally, in FS experiments the densification occurs in few seconds (or minutes) much more quickly than in the conventional processes, which usually require hours. The reduction of the processing times and temperature by FS is, in general, larger than what can be obtained using other innovative sintering technologies, like SPS or hot press (Figure 1).

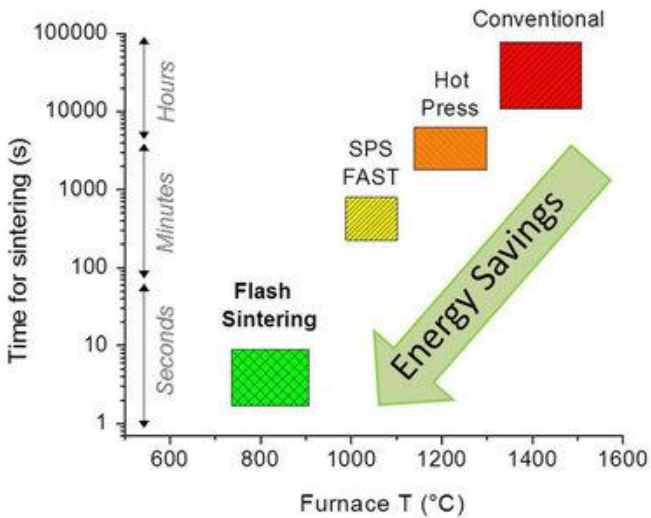


Figure 1: Typical time and temperature for sintering YSZ using different technologies. Taken from [10].

The advantages of FS are not only related to the evident reduction of the energetic and economic costs for sintering. In fact, the reduced sintering time and temperature could allow to densify outside the equilibrium materials [11] or materials showing undesired phase transitions at high temperature. Additionally, flash sintering can be very effective for sintering ceramics that produce volatile species, like potassium niobate [12]. Therefore, FS represents a possible route for producing materials that

cannot be obtained via conventional processes. Additionally, the short treating time allows to obtain dense ceramics with very limited grain coarsening.

Flash sintering is a very novel sintering technique, the first paper on this argument having been published in 2010 by Cologna et al.[6]. FS belongs to the family of Field-assisted Sintering Technology (FAST), where the combination of electric field/current application and temperature allows a rapid densification.

FS presents some peculiar characteristic when compared with other field-assisted routes like Spark Plasma Sintering (SPS). The main difference is that in FS process the current is forced to flow within the specimen whereas in SPS the sample is contained in a graphite die which, being usually more conductive than the ceramic, is responsible for the current flow. Hence, the heat generation mechanism is pretty different in FS and SPS. In SPS the die is heated by Joule effect, then the sample is heated by radiation/conduction from the die. Conversely, heat generation within the green specimen takes place in FS, as a result of the current flow. For this reason the heating rate involved in the two processes are pretty different, up to 10^3 °C/min for SPS, in the order of 10^4 °C/min for FS [13]. Actually, the current flow within the specimen during sintering can not be considered the only discriminant characteristic for defining flash sintering. In fact, also in many SPS processes of metal powder the current mainly flow within the metal (often more conductive than the graphite die). Therefore, we need to improve the definition of FS.

An accurate analysis of the scientific literature on this topic allows to define flash sintering as a very rapid sintering phenomenon (few seconds/minutes) accompanied by a current flow within the sample and by the so called “flash event”.

The flash event is characterized by three phenomenological effects:

- i. The sample is quickly heated by an internal Joule effect[13–15];
- ii. The material shows a transition from insulator to conductor-like[6–8,16];
- iii. The sample starts to emit light[17–20].

If these three phenomena occur together, the Flash Event (FE) takes place. In some materials like titania and zirconia during the FE also texture [21] and new phases emersion have been observed[22]. However, these have been recorded just in two materials and cannot be considered as a general characteristic of the flash event.

The flash event is not strictly related to sintering and it can be observed also in dense specimens. FE has been reproduced also in different pre-sintered materials with different level of densification (SiC [23], LSCF[24], YSZ [9,25] ...). Of course, we can not talk of flash sintering in this case since the material is already dense. Nevertheless, if FE is reproduced on a green body, a very rapid densification occurs and the process can be identified as flash sintering.

Therefore, we can state that *"Flash sintering is a field assisted sintering technique, characterized by a current flow within the specimen and showing a very rapid densification, a drop of electrical resistivity, a quick internal heating of the specimen by Joule effect and a strong light emission"*.

The experimental set up for flash sintering is not complex and expensive; it is usually constituted by four main parts(Figure 2):

- i. Electrical furnace;
- ii. Power source;
- iii. Multimeter;
- iv. Displacement sensor.

The green specimen is connected by two metallic wires to the power source and to a multimeter, which allows to record the electrical parameters (tension and current). The main part of FS experiments have been conducted using DC field, but many work using AC are available in the scientific literature. The contact between the green specimen and the metal electrode is often improved by adding some conductive pastes (like Pt or Ag...). The choice of the metal wire used as electrode should be done considering several constrains. First, the materials should be conductive, it should resist to oxidation (most FS experiments are carried out in air) and it should have an high melting temperature. For all these reasons the material most commonly used is platinum or Pt-alloys. Nevertheless, for flash sintering experiments in inert atmosphere also graphite or SiC electrodes can be used or, if the treating temperature is limited, stainless steel, silver or Ni alloy are a suitable choice. After the sample is connected to the electrodes, it is introduced on a furnace and heated up until the flash event is reproduced. The sintering process can be

monitored by measuring the sintering shrinkage using a displacement sensor (like an LVDT[26]) or making a video with a CCD camera (Figure 2).

Different sample shapes have been employed in FS experiments. The specimens used in the first FS experiments were characterized by a dog bone shape with two holes at the opposite side of the specimen. The electrodes are forced within these holes. This shape is quite complex and find limited technological applications; nevertheless, this is the best choice for studying the process. In fact, the dog bone shape reduces many problems observed during FS like current concentrations. So, the samples result homogeneous in their cross-section and the conductivity evolution can be easily studied. The second geometry used in flash experiment is bar-like. In this case the metallic wire is wrapped around the external part of the green specimen. The third used geometry corresponds to cylindrical pellets. The electrodes are often constituted by metallic disks or grids pushed in contact with the pellet faces. Also in this case the application of a conductive paste can be very effective for reducing sparking at metal/electrode interface or for improving the homogeneity of the sintered body. Nevertheless, especially if stocky geometry are used (high diameter/height ratio) current concentrations are very likely to be formed leading to a non-homogeneous sintering process[27].

Although the technology behind flash sintering is quite simple its interpretation in much more complex. Many process parameters can influence the flash sintering behavior. The main ones are summarized in Figure 4. The different operative condition can influence the onset temperature for flash sintering, the densification behavior and the microstructure. The effect of each parameter will be discussed in the followings sections of this process review.

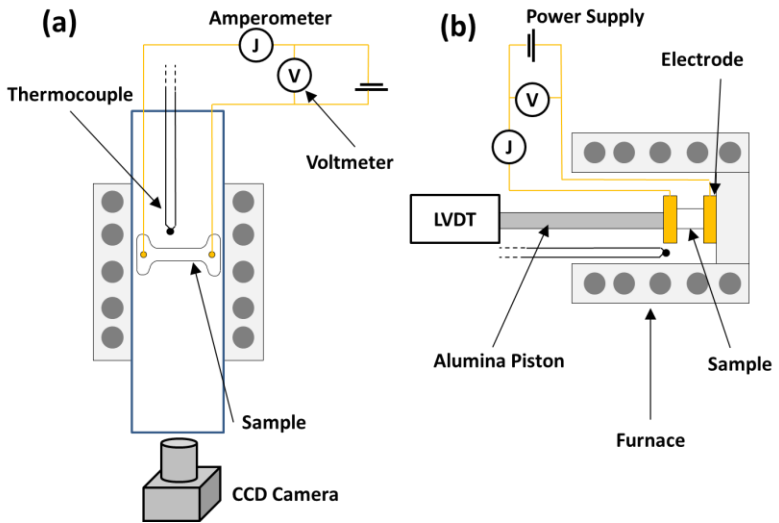


Figure 2: Two possible experimental set up for flash sintering experiments: the sintering can be monitored by a CCD camera (a) or by an LVDT sensor (b).

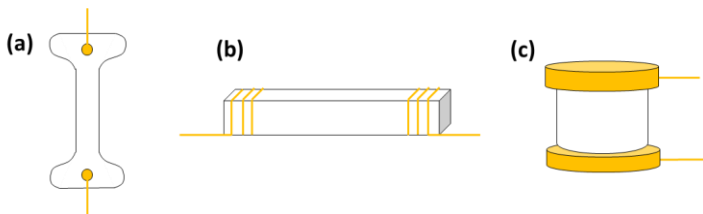


Figure 3: Possible sample shape for flash sintering experiments: dog bone (a), bar (b) and cylindrical pellet (b).

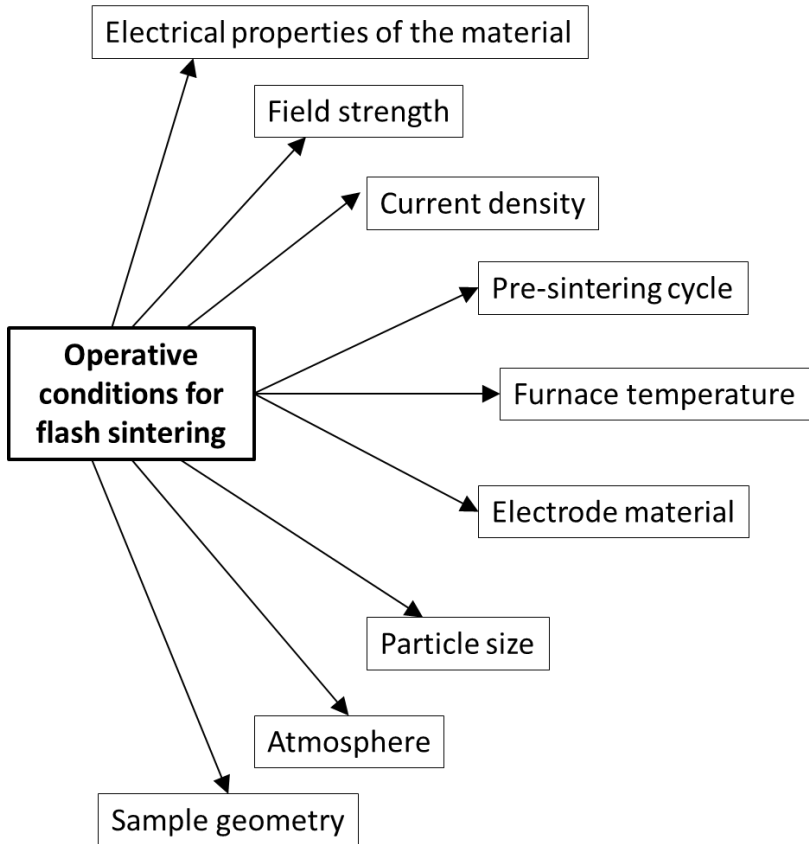


Figure 4: Process parameters that influence the flash sintering behavior.

Flash sintering experiments can be carried out applying the main process parameters (T , E , J) in different ways. The two most common experiments are reported in Figure 5.

Figure 5(a) is referred to a constant heating rate experiment. The electric field (E) is applied at low furnace temperature (T_i). At such temperatures the ceramic is an insulator and very few electric current (J) flows. For this reason the power source, in this temperature region, is working in voltage control. Nevertheless, ramping the temperature the specimen becomes progressively more conductive and J increases. This stage of flash sintering is often called I stage or incubation[19]. The increase in

current flow also increases the specific power dissipation (w) within the ceramic that can be calculated as:

$$w = EJ \quad (1)$$

Now, since the system during the incubation is working in current control, we can calculate was:

$$w = \frac{E^2}{\rho} \quad (2)$$

where ρ is the electrical resistivity of the material. Since, in many ceramics ρ is decreasing with temperature (following an Arrhenius-like behavior), during the incubation of FS the power slowly increases. Exceptions are represented by metallic like ceramics, among them WC, HfB₂, MAX phases et cetera.

At a certain onset temperature an abrupt drop of electrical resistivity is observed and the current rises. The system switches from voltage to current control, reaching the maximum power dissipation. This is referred as the flash event or II stage of flash sintering[19]. During this stage the highest power dissipation are reached and the sample undergo to a thermal runaway of Joule heating. In this stage the densification starts and extremely higher sintering rates are obtained. It is to underline that the onset temperature for FS is in almost all the cases much lower than the conventional sintering temperature; thus, resulting in an anticipate sintering phenomenon.

After that the system reaches the current limit, the field decreases reaching an equilibrium condition. When the field is stabilized the III stage or steady stage of FS begins[19]. Now the system is working in current control; therefore, the specific power dissipation (w) can be written as:

$$w = J^2 \rho. \quad (3)$$

During the third stage, a residual densification can be still observed but the sintering rate progressively decreases.

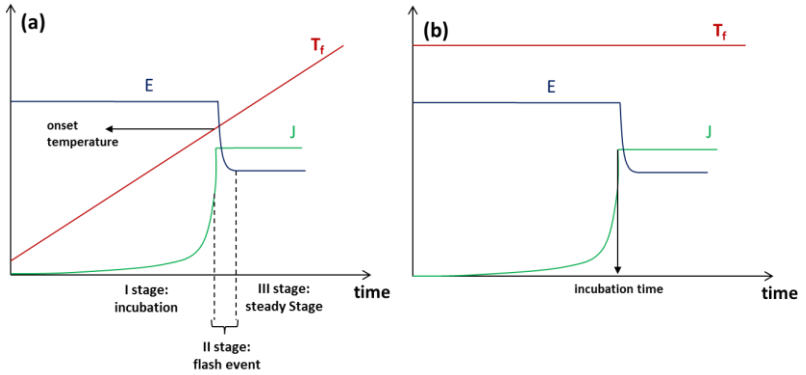


Figure 5: Electric field (E) and current (J) evolution during constant heating rate (a) and constant furnace temperature, T_f , (b) flash sintering experiments.

Figure 5(b) shows the second most used experimental set up for FS. In this case the furnace is at a constant temperature. Once that the power supply is switched on the current start to flow and, even if the furnace temperature is constant, J progressively increases with time. This behavior can be observed only if appropriate field strength is used: if the field is too low J remains constant. Also in this case an abrupt drop in electrical resistivity is observed and the flash event takes place. Therefore, it is possible to define again three stages: first the system works in voltage control and the current slowly increases, then the flash event is observed, finally the system reaches a new equilibrium in current control. When the isothermal flash experiments are conducted the most significant parameter to define the material behavior is the incubation time, which is the time needed for the system to switch from voltage to current control. The incubation time is of course related to furnace temperature and applied field [28], this will be discussed in the next sections.

1.3 Proposed mechanisms for flash sintering

Starting from 2010, when flash sintering was discovered, the attention of the scientific community about this technology has constantly grown and the number of papers published on this argument have risen year by year. The reasons for such

interest are mainly technology-driven; an industrial application of FS would allow a drastic reduction of sintering costs, energy consumption and CO₂ emissions. Nevertheless, being the process very “rich” and multidisciplinary (involving sintering, light emission, electrical properties, new phase formation, textures, non-conventional microstructures...) also a lot of scientific interest has been risen with the aim to interpret and explain the phenomenon. With this purpose different mechanisms for flash sintering have been proposed.

All mechanisms start from the assumption that for explaining flash sintering one should explain both charge and mass transport. Charge transport can be either ionic or electronic, depending from the structure of the material, its purity or from temperature. However, it seems reasonable that the extremely high heating rates obtained during the flash event are unlikely to be due to ionic conduction alone. Probably, a dominant electronic contribution to Joule heating can be pointed out, as a result of a massive electronic scattering. Conversely, mass transport involves diffusion and atoms movement from the surface with positive to negative curvature. Probably, the simplest explanation for flash sintering is based just on Joule heating: the sample is heated by the current flow and for this reason both electric conduction and diffusion are enhanced. At this point the question is: “Is the real sample temperature upon FS high enough for justifying a such rapid densification? Is the sample temperature enough high for justifying the drop of electrical resistivity?” These are still opened questions and will be more in detail discussed point by point in the next sessions.

A second mechanism that has been proposed is based on the selective Joule heating at grain boundary[29–31]. Grain Boundaries (GB), in fact, presents features different from the bulk: different diffusion kinetics, space charge formation... For these reasons one can imagine that the grain boundary temperature is higher when compared to the grain bulk . The local heating at the interparticle neck or at the grain boundary could increase the diffusion processes and densification. Additionally, the formation of a liquid phase at the GB could enhance electrical conductivity and increase the sintering rates, providing a fast diffusion path. The presence of an interparticle liquid phase would also generate capillarity stresses as reported by Chaim[30]. He calculated that, assuming 100 nm alumina particles, the capillarity

stress would be ~ 27 MPa [30], this stress is indeed higher than the sintering stresses and comparable to the load usually applied during SPS processes. This would provide an additional driving force for densification.

The formation of a local liquid film or temperature gradient between GB and bulk are a very attractive hypothesis. In fact, they could also explain some microstructures obtained via flash sintering: the ceramic can be sintered up to nearly full density with submicrometric grain size[6,32–34]. In addition, previous works have shown that in monolithic YSZ specimen the application of a weak DC electric field results in a retarded grain coalescence[35]. Ghosh et al. have proposed that if the grain boundary is hotter than the surrounding region this would lead to a minimum of the interfacial energy (γ_{gb}). This could be explained considering the Gibbs energy associated to the grain boundary:

$$\gamma_{gb} = \Delta H_{gb} - T \Delta S_{gb} \quad (4)$$

where ΔH_{gb} and ΔS_{gb} the excess of enthalpy and entropy associated to the GB. Thus, if the temperature is higher at the GB a minimum in the interfacial energy is achieved. If the grain boundary moves, towards colder region γ_{gb} would increase in this reduces the driving force for grain growth.

The effect of a liquid film formation on grain coalescence was studied by Narayan [36]. He demonstrated that in case of selective melting of the grain boundary the driving force for grain growth is reduced almost to zero. This should inhibit all grain coalescence phenomena.

However, it seems quite hard to state that significant temperature differences can be present in case of micrometric or submicrometric grains. This was confirmed by Holland et al. [37] who showed, via numerical simulation, that the temperature gradients are very limited in micrometric scale. Additionally, they demonstrated that, although some gradients are formed in the early stages of flash sintering (just after interparticle neck formation), these should be removed in fraction of second (depending from the particle size). So, it seem that significant temperature

differences between grain boundary and bulk are not the crucial mechanism behind flash sintering.

The third mechanism involves the formation of Frenkel pairs within the grains during the flash event [6,38–40]. Also, a thereof model based on nucleation theory has been developed in order to explain the incubation time in isothermal FS experiments. In this model embryos of material with high dielectric constant are thought to be formed under E field application, as a result of dipoles vacancy/interstitial associated with Frenkel defects [41]. In this way the electric field provides the driving force for nucleation and a critical radius for the embryos, above which nucleus can grow, can be calculated in nanometric – submicrometric scale [41].

The theory of Frenkel pairs formation was proposed mainly for explaining the rapid densification and so mass transport. Indeed, the diffusion kinetics are proportional to the defect population; hence, if one assumes that vacancy/interstitial pairs are formed this would increase the defect population and the mass transport phenomena rise. Additionally, if the Frenkel defects get ionized also electronic defects are formed for balancing the charge and electronic conduction is activated, leading to a drop of electrical resistance and producing luminescent effect that can explain the photoemission. Although, this mechanism involves all the main phenomenological effects observed during FS, until now, it has found poor experimental evidences.

A fourth mechanism involves the formation of partially-reduced structures during flash sintering. This mechanism was proposed for the first time by Downs in 2013 [9] and it is mainly focused on oxide ceramics, finding only a poor application to covalent materials. The formation of partially reduced oxide is well known and it has been extensively studied on YSZ using direct current [42–46]. This is associated with the formation of the so called “electrochemical blackening” that can be also observed during DC-FS under severe condition of current/treating time [9,47]. If the material is partially reduced its electrical properties would change [43,45] leading to an increase electronic contribution to conduction or it could change the activation energy for cations [48] diffusion leading to non-conventional grain growth [48,49] and densification phenomena. The change in grain growth behavior was also reported in reducing atmosphere for different oxides [50,51].

In the next sections we are going to describe more in detail the different phenomenological effects observed during flash sintering are described in detail and links with the proposed mechanisms are provided and discussed.

1.4 Flash sintering: Phenomenology

1.4.1 Thermal runaway and Joule heating

The thermal runaway is always occurring during the flash event and allowing an abrupt heating of the ceramic due to internal heat generation. It was calculated that during the flash event the heating rate could approach 10^4 °C/min [13]; nevertheless, this value depends on the maximum specific power dissipation set during the experiments, the material specific heat and other process parameters (sample shape, mass...).

The fact that thermal runaway is the trigger of the flash event is accepted by the majority of the scientific community. Although the thermal runaway explains why and when the flash event takes place, it is still not clear if it is the only reason leading to densification[14], photoemission and resistivity drop observed during flash sintering. The thermal runaway model for describing the onset condition for FS was independently developed by Todd [14] and by Zhang [15] and coworkers in 2015. The model is based on the power balance between electrical power and the heat dissipated by the specimen. The concept is quite basilar: the flash event takes place when the sample is no more able to dissipate the internal-generated heat by Joule effect. Therefore, this model is somehow more simple than that developed by Naik et al. for describing the incubation of flash sintering as a nucleation phenomenon, assuming the formation of high-k embryos due to Frenkel pairs [41]. Additionally, the thermal runaway model finds solid theoretical bases on elements that can be easily determined and measured (like power dissipation, heat exchange, electrical conductivity...) and it is valid without the assumption that the material undergo to particular transformation. These reasons are at the base of the success of this model, which has also been validated by many experimental results[15,23,52–56]

A qualitative representation of the basic idea for the thermal runaway is shown in Figure 6. Figure 6(a) is referred to a constant heating rate FS experiment. The red

line represents the power dissipated by Joule effect as a function of the sample temperature (T_S). This curve is rising with temperature; in fact, being the system in voltage control during the incubation of FS the electrical power dissipation (W_{in}), assuming Arrhenius conduction and an homogeneous sample temperature, is:

$$W_{in} = \frac{VE^2}{\rho_0} \exp\left(\frac{-Q}{RT_S}\right) \quad (5)$$

where W is the power dissipation, V the sample volume, ρ_0 the pre-exponential constant for resistivity, Q the activation energy for conduction, R the universal gas constant.

The blue lines represent the heat dissipated from the sample by radiation (W_{out}) at different furnace temperatures (T_F). Indeed, also this curve rises with T_S ; in fact, higher the temperature difference between the sample and the atmosphere higher will be the heat exchange. If the temperature is enough high one can assume that all the heat is exchanged by radiation and so it is possible to write:

$$W_{out} = S \sigma \epsilon (T_S^4 - T_F^4) \quad (6)$$

where S is the sample surface, σ the Stefan-Boltzmann constant and ϵ the emissivity. According to Eq. 6 ramping the furnace temperature the W_{out} curve moves to the right in the plot in Figure 6(a). If the furnace temperature is low (dashed line in figure) W_{out} and W_{in} curves presents an intersection which represent an equilibrium condition and FS cannot be reproduced. However, increasing T_F the two curves becomes tangent; in this case the power that is consumed by Joule effect cannot be dissipated by the sample (being W_{in} plot always above W_{out}) and this represent the onset for FS. Therefore, the sample undergo to an uncontrolled heating process, which is at the base of the flash event.

The relation between the onset field/temperature in constant heating rate experiments results monotonical; being the sample treated with larger field flash sintered at lower temperatures[8,57]. This is due to the fact by increasing E the in W_{in} plot in Figure 6(a) moves upward, so the onset condition is reached at lower

temperature. The experimental relation between onset temperature for FS and electric field is reported in Figure 7(a) for 8YSZ. One can observe that, by increasing E , a drastic reduction of sintering temperature can be obtained.

Similar consideration can be done for isothermal flash experiments. In this case W_{out} plot do not change its position (being the furnace temperature constant); but increasing E the W_{in} curve moves upward and so, once again, an onset condition can be determined. Indeed, the incubation time depends from the applied field and furnace temperature, as shown in Figure 7(b). Increasing E the area between W_{out} and W_{in} becomes larger and this means that the net power absorbed by the sample rises. Therefore, increasing E the sample would undergo to a more rapid heating, reducing the incubation time. An analogous behavior can be obtained increasing the furnace temperature at which the experiments are carried out: increasing T_F it becomes more “difficult” to dissipate the internal heat generated by Joule effect.

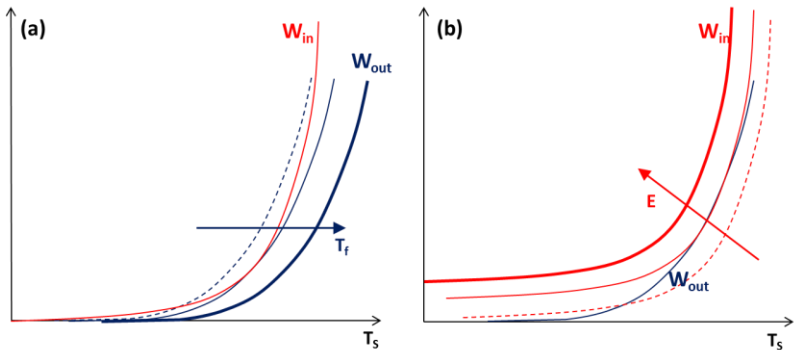


Figure 6: Flash sintering onset determination for constant heating rate (a) and isothermal flash sintering experiments (b). The dashes lines represent condition where FS cannot be reproduced, the thin continuous lines are the onset for FS, the thick continuous lines are conditions leading to the flash.

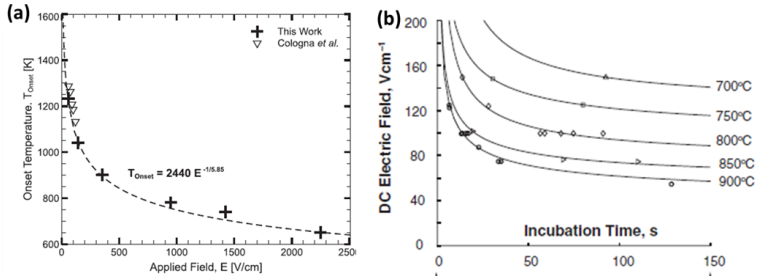


Figure 7: Relation between onset flash sintering temperature and electric field (a) [8] and between incubation time and the applied field for different furnace temperature (b) for YSZ[28].

The onset condition for thermal runaway is not only depending on the applied field but it is also a function of the electrical properties of the tested material, the more conductive specimens being flash sintered at lower temperatures. This behavior is quite well known from the early flash sintering experiments and it can be demonstrated just comparing the flash temperature for different materials [6,33,39,58–60]. Such relation is due to the fact that the more conductive specimens during the incubation of FS are characterized by higher power dissipation (the system is working in voltage control); in this way, the red curve in Figure 6 would shift upward and the onset condition can be easily reached.

More recently, Pereira da Silva et al.[52] and Dong et al. [53,54] developed more sophisticated models for the thermal runaway. In particular Dong et al. calculated the relation between the onset field and temperature as [54]:

$$\ln\left(\frac{E^2}{T_{on}^A}\right) = \frac{Q}{R T_{on}} + A \quad (7)$$

where Q is the activation energy for conduction, T_{on} the onset temperature for flash sintering at a given field (E) and A is a constant depending from the sample geometry/heat exchange and can be empirically calculated. Eq. 7 has been proved to provide a quite good approximation of the many experimental results obtained in constant heating rate flash sintering experiments[54].

Bichaud et al. studied the heating rate of the specimen during FS of cylindrical pellets[56]. In this case the heat is not only dissipated by radiation toward the

environment, but significant heat loss could take place by conduction through the metallic electrodes. They calculated the heating rate of the specimen as:

$$\frac{dT_S}{dt} = \frac{1}{C} \left(\frac{E^2}{\rho} - k_1 \frac{2}{h} (T_S - T_F) - k_2 \frac{2}{r} (T_S - T_F) \right) \quad (8)$$

where C is the sample heat capacity for unit of volume, r the sample radius, h the specimen height, k_1 and k_2 are the heat transfer coefficients at the flat surface (in contact with the electrode) and side surface, respectively.

The key point that deserve to be underlined from Eq.8 is that the heating rate obtained during the incubation of the flash event is dependent from sample geometry; i.e. larger samples (high value of r or h) being characterized by higher heating rate using the same field strength. This result is in perfect agreement with many experimental findings. In fact, it has been shown that the flash event can be reproduced using lower incubation times in large specimens (Figure 8(a)) [56]. Additionally, it was demonstrate that, when working with very thin samples (in the order of few mm), the onset temperature for FS could increase of hundreds of degrees with respect to the traditional dog bone geometries[61].

The strong relation provided by the thermal runaway model between sample conductivity and onset condition (field/temperature) for flash sintering can explain also other experimental results:

- i. Francis et al. showed that the flash sintering temperature decreases by lowering the powder particle size (Figure 8(b)) [62]. This is linked to the different electrical properties obtained in the green compacts by changing the particle size. In fact, due to Van de Walls force the contact area between particles increases with decreasing particle size[62]. In this way the over potential at the particle/particle interface would decrease. Additionally, conventional sintering processes are anticipated in the case of small particles; in this way a continuous path for current flow is easier formed enhancing electrical conductivity and anticipating the thermal runaway.

- ii. Although flash sintering is mainly a pressure-less technique flash-sinterforging experiments have also been carried out. Francis et al. showed that an external pressure application (1.5 - 12.0 MPa) can reduce the onset temperature for the flash event(Figure 8 (c)) [63]. They explained this effect as a result of local field enhancement due to electro-chemo-mechanical effect. However, an external pressure application could enhance the quality of the particle/particle contact and reduce the temperature needed for particle welding; thus, allowing an increase in electrical conductivity and reducing the onset temperature for FS.
- iii. The sintering atmosphere (oxygen partial pressure, reducing potential...) can change the defect population in oxide ceramics. This has an influence on electrical conductivity and so also on the onset condition for flash sintering. The atmosphere effect on flash sintering on ZnO was studied by Zhang et al. [64]. They showed that the onset condition for FS can be reduced of hundreds of °C using Ar or Ar/H₂ atmosphere when compared with air (Figure 8(d)).They attributed this behavior to a higher conductivity showed by ZnO in reducing atmosphere[64]. Nevertheless, the ionization potential of Ar is much lower than air (N₂/O₂). Therefore, it is also possible to suggest a partial contribution of an interparticle plasma formation, which rises electrical conductivity. Further experiments in inert and high dielectric strength atmosphere (i.e. N₂) would be needed for an accurate and definitive understanding of atmosphere effect on flash sintering.
- iv. The use of different electrode materials can influence the conductivity of the ceramic, changing the onset for the thermal runaway. Caliman et al. have shown for β-alumina (cationic conductor) that Pt acts as a blocking electrode for charge transfer between the metal and the ceramic; thus, flash sintering was not reproduced using Pt electrodes. Conversely, in case of silver electrodes, which allow a more efficient electrochemical transfer at the interface, the flash event has been observed.

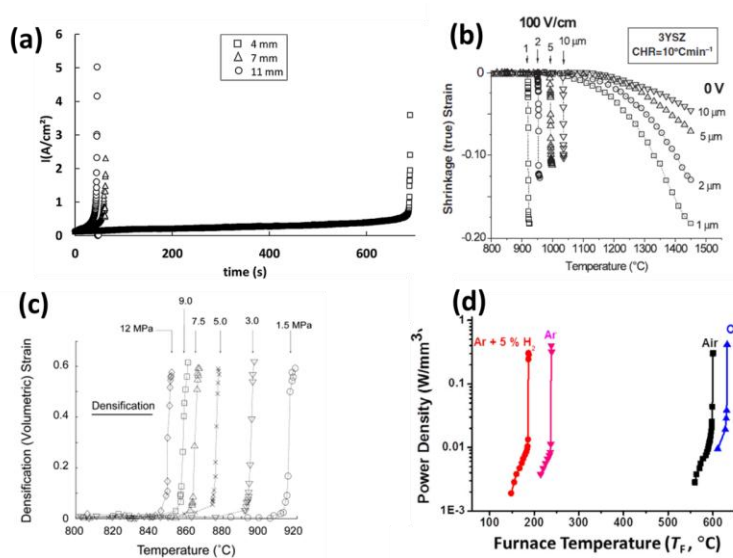


Figure 8: Sample length effect on incubation time for FS in $\text{Al}_2\text{O}_3/\text{YSZ}$ composites (a)[56]. Effect of particle size (b)[62] and applied pressure on onset FS temperature for YSZ[63]. Onset temperature dependence from sintering atmosphere in ZnO (d) [64].

The effect of the field polarization (AC, DC, pulsed...) on the thermal runaway has not been deeply analyzed yet. Dancer collected several data from different authors regarding the FS condition using AC and DC field[57] in 8YYS. Her data, reported in Figure 9, do not show a clear trend. Nevertheless, this point deserves further analysis. In particular, by using different frequencies in AC it would be possible to increase the power dissipation as a result of the effect of imaginary part of the dielectric constant. Anyway, even if the effect of field polarization on the onset is not so evident, it can change the structure of the sintered body as pointed out by Muccillo et al.[47]. In fact in case of DC field a partial reduction of the oxide can be obtained, while it do not happen when using AC[47].

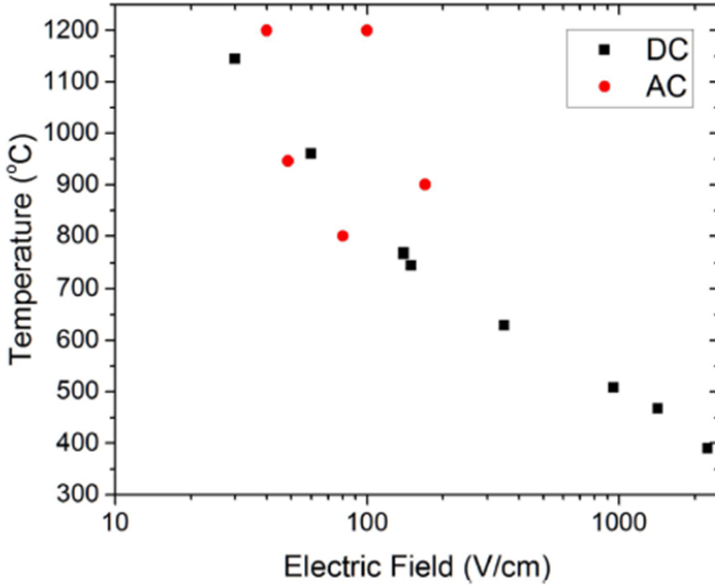


Figure 9: Relation between onset temperature for FS and applied field for 8YSZ in AC and DC treatments.[57]

So far we analyzed Joule heating as a trigger for the flash event and we focused our analysis on what is happening when the system is working in voltage control. Now, we describes what is going on when the current limit is reached. At this point, the power dissipation peak is observed and it is equal to the voltage limit times the current limit. The product of these two values gives the maximum power dissipation that can be obtained and so it is strictly related to the maximum heating rate achievable by the system. Then, being the system in current control, the power dissipated by Joule effect can be written as:

$$W_{in} = V J^2 \rho_0 \exp\left(\frac{Q}{RT_s}\right). \quad (9)$$

Hence, according to Eq. 9 W_{in} decreases with the sample temperature, as qualitatively shown in Figure 10. Therefore it is possible to define a new equilibrium

condition when the electrical power is equal to the heat dissipated by radiation toward the environment (Figure 10).

This new equilibrium is reached at a sample temperature higher than that at which the power peak is observed. Therefore, also after the current limit reaching the sample is still heated. This is due to the fact that after the power peak the W_{in} still is higher than W_{out} . Nevertheless, the difference between the two power decreases with sample temperature (T_s), so the heating rate progressively decreases and the temperature approaches the equilibrium one. As a result of this heating process after the current limit reaching the resistivity of the material decreases and it is responsible for the decrease of E as reported in Figure 5. When E is stabilized and the equilibrium temperature is reached the third stage of FS, also known as steady stage begins.

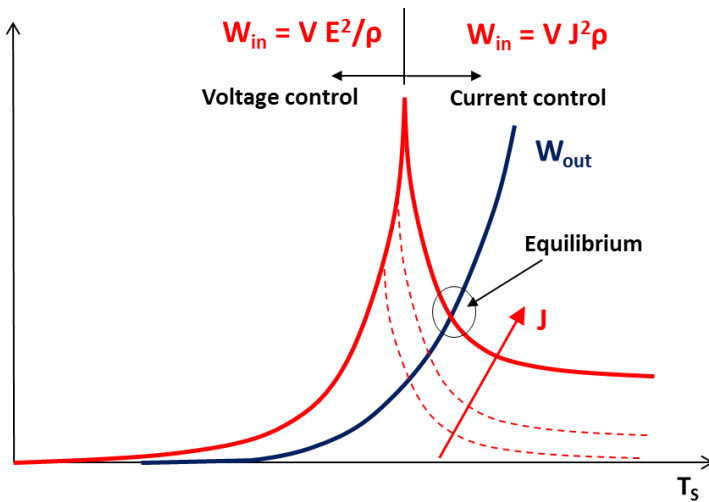


Figure 10: Qualitative power dissipation plot during the different stages of flash sintering.

Now, the key parameter for describing the system behavior is the current density (J). In fact, changing J the curves in Figure 10 shift allowing to obtain different equilibrium temperature during the flash.

A correct estimation of the real sample temperature during the steady stage of flash sintering is crucial: it would allow to clarify if the temperature increase due to Joule effect is or not the only reason at the base of a so rapid densification and electrical resistivity drop.

A first analytical attempt to determine the sample temperature during FS was carried out by Raj [65] . He provided an analytical expression for calculate the sample temperature assuming an homogeneous power dissipation in sample gage section and that the heat is only exchanged by radiation. This allows to write that:

$$T_S = \left(T_F^4 + \frac{Win}{S\sigma\epsilon} \right)^{0.25} \quad (10)$$

where S is the sample surface area and *Win* can be easily measured by multimeter. Being this relation referred the heat exchanged from the surface by radiation it allows to calculate the surface sample temperature and do not give direct information of the temperature in the core. Although Eq. 10 is based on some approximations and the value of the emissivity (ϵ) should be a priori estimated, this has provided in many cases a good approximation of the real sample temperature during FS of dog bone specimens. In fact, the results obtained using Eq. 10 were successfully compared with sample temperature measurement by experimental technique[17,19,63].

Different experimental attempts were for measuring the specimen temperature during the steady stage of flash sintering:

- i. Park et al. measured the sample temperature by in situ impedance spectroscopy[66]. However, this method is based on the assumption that during the flash event no unconventional conduction mechanisms are activated; hence, it would be possible to compare the impedance measured during the flash with the conductivity extrapolated in conventional conditions.
- ii. Different authors measured the sample temperature using a pyrometer [63,67–69]. This kind of measure gives the local surface temperature of the specimen; which, in line of principle could be different from the core. When using a pyrometer the emissivity of the ceramic is an important parameter that should be estimated. This is probably the weak point of

this kind of measure, especially assuming that often the emissivity could change with temperature[70].

- iii. Probably the more accurate measure of sample temperature during FS has been done by XRD[17,71]. In fact, the XRD peak position depends from the cell parameter which, with an appropriate calibration can be related to the ceramic temperature.
- iv. When reproducing the flash event on dense specimen the sample temperature can be estimated from the thermal expansion[72]. This method is not working for flash sintering, where the sintering shrinkage would hide the thermal expansion.

The last point that deserves to be discussed about Joule heating regards the temperature distribution homogeneity within the specimen. If we assume that heat is exchanged by radiation from the surface it would be reasonable that the hearth of the specimen was hotter than the surface. Nevertheless, no microstructural evidences of such e phenomenon (i.e. densification or grain size gradients) have been reported for dog-bone specimen. Lebrun et al. investigated the temperature distribution in dog bone geometry (cross section: $1.3 \times 0.65 \text{ mm}^2$) via XRD[71]. They observed in YSZ that a broadening of diffraction peak width related to temperature gradients can be observed only if the power peak exceeds 1000 mW/mm^3 ; this value is higher than what usually needed for FS of zirconia $\sim 500 - 1000 \text{ mW/mm}^3$. If the power exceeds 1000 mW/mm^3 a temperature gradient between surface and core around 100°C can be estimated. Nevertheless, this broadening is only a transient observed during the flash event and it disappears during the III stage. Conversely, Steil et al. reported in cylindrical pellets ($\phi 8\text{mm}$) different microstructures in sample center and periphery[73]; being the grains larger in the core of the specimen. Additionally, they observed melted areas mainly located in the center. Their results are therefore coherent with the presence of a temperature gradient in cylindrical pellets. However, they used power dissipation up to $\sim 2500 \text{ mW/mm}^3$, this value is much higher than what estimated by Lebrun et al. for producing temperature gradients within dog bone specimen [71]. An analytical model of temperature distribution during FS was developed by Hewitt et al. for cylindrical pellets;

considering both temperature gradients in radial and axial direction due to the heat loss through sample surface and metal electrodes, respectively. Their analytical solutions have suggested that some temperature gradients can be present during the steady stage of flash sintering of cylindrical pellets[74].

1.4.2 Sintering and microstructures

The sintering process is conventionally divided into three main stages. According to Rahaman[3], in the first stage the particles get welded together via interparticle neck formation. This stage is activated at relatively low temperature and it is usually based on surface diffusion or evaporation/condensation mechanisms. At such temperatures a very moderate densification can be achieved and the distance between particles center remains substantially constant. It is assumed that the stage finishes when a relative density of ~65% is reached, or when the radius of the interparticle necks reaches 40-50% of the particle radius.

At higher temperature bulk and grain boundary diffusion get activated and the second stage of sintering starts, leading to densification up to ~90%. The densification is accompanied by a strong shrinkage of the material based on the fact that the particle centers get closer. In this stage the pores are still quite continuous and they reaches their equilibrium shape forming the dihedral angles. When the pores get isolated at the grain corners the third stage of sintering begins, allowing an additional densification and shrinkage.

Therefore, when we discuss of the electric field effect on sintering we can divide the argument in two main parts:

- i. First, we can analyses the field effect on neck formation (I stage of sintering)
- ii. Second, we can analyses the field effect on densification (II-III stage of sintering)

Cologna et al. studied the interaction between E-field and neck formation in 3YSZ[75], without reproducing the flash event and Joule heating. They conclude that the neck growth rate is substantially unaffected by E-Field application. This is in other word meaning that the electric field alone (without current and Joule heating) do not influence the mechanisms at the base of particle welding, in particular surface

diffusion. For these reasons it seems that FS can be more correctly classified as Electric Current-Assisted Sintering (ECAS) rather than a Field-Assisted Sintering.

Conversely, a very huge effect of electric field/current application can be observed when the flash event is reproduced, allowing a very rapid densification (few seconds) at very low furnace temperature[6–8,24,68,76]. Therefore, the electric field/current effect on the I stage of sintering is in general very moderate, while it becomes more relevant when describing the II and III stage. In fact, until a relevant current density is reached the field effect are limited.

At this point a good question is: “Is the Joule heating observed during the flash event enough for justifying a so rapid densification?”. A definitive answer regarding this point has not been achieved and unanimously accepted yet by the scientific community, also considering how difficult is to obtain a precise measure of sample temperature during the flash event.

What is pretty sure is that at least a partial contribution of Joule effect on densification can be pointed out. However, Raj showed that the temperature reached during flash sintering are much lower when compared with what would be expected from the measured sintering rate during flash sintering[65]. In particular he showed that 3YSZ during FS is densified in ~ 3.6 s, while conventional sintering processes requires soaking time of ~ 1 h (3600 s) at 1450°C . This means that during the flash event the sintering rate is ~ 1000 times higher than in conventional processes. Hence, using the sintering equations and assuming different activation energy for densification it is possible to extrapolate the temperature that would be needed for a such rapid densification. Raj estimated this temperature close to 1900°C (Figure 11); much higher than the sample temperature estimated using Eq. 10 which was approximately 1250°C [65]. Such temperature estimation is consistent with the temperature measured from lattice expansion via XRD, which results just above 1200°C when power dissipation of about 1000 W/mm^3 is achieved in the III stage of FS.

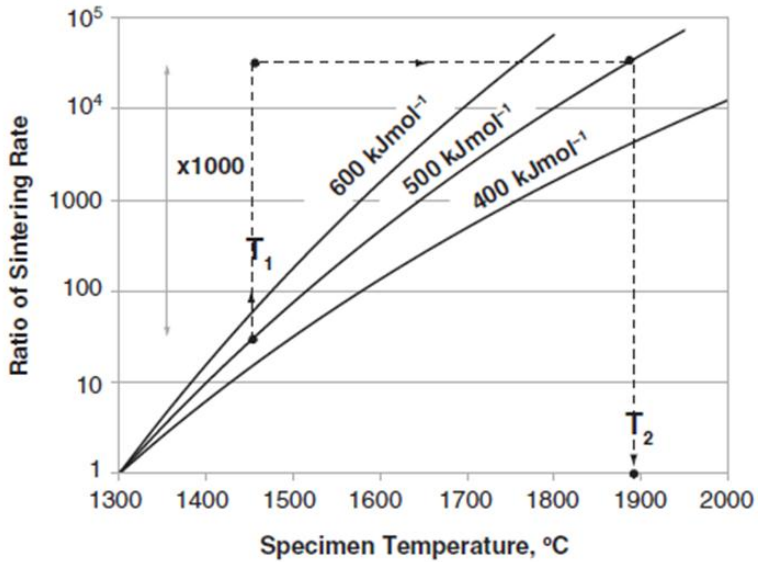


Figure 11: Sintering rate as a function of sample temperature using different activation energy for densification. T_1 is the specimen temperature estimated using Eq.10; T_2 is the temperature needed for justifying the observed sintering rates[65].

On these bases, being the sintering rate proportional to the defect population, a mechanism based on field-induced Frenkel pairs formation was developed[6,38–41,62]. However, up to now quite poor experimental evidences have been recorded supporting this theory. Additionally, what it seems is that the enhanced sintering rates are more current-induced than field-induced. In fact, until the current is low there are no significant field effect on sintering, like it has been pointed out by Cologna et al. in the early stages of FS[75]. Whereas, during the flash event when the current starts to flow, and the field decreases, differences between the conventional sintering and flash sintering can be pointed out, even considering Joule heating [65].

A second “unconventional” mechanism that could explain the densification is based on the assumption that the material can be partially reduced during the flash sintering process. This mechanism is mainly focused on oxide ceramics treated

using DC field. The possibility of the formation of a partially reduced oxide during DC flash sintering experiments has been for the first time pointed out by Muccillo et al. in 2011[47] and it has been in detail discussed by Down in 2013 [9]. Narayan states that the partial reduction of the oxide would lead to the formation of discharged oxygen vacancies; that are characterized by a lower activation energy for diffusion[29]. Additionally the reduction of the oxidation state of cations can influence their mobility during flash sintering[48,49]; the result is coherent also with grain growth enhancement measured in reducing atmosphere [50,51].

One last point deserves to be analyzed when discussing about densification during flash sintering. This point is focused on the concept that the sintering rate during flash sintering cannot be easily compared with conventional processes. This is due to the fact that the heating rates are completely different: according to Grasso et al. the heating rate during the flash event could reach 10^4 °C/min[13], ~ 3 order of magnitude higher than in conventional process.

The heating rate effect on sintering becomes very important if the activation energy for the densification is higher than the activation energy for grain coarsening; this resulting in the fact that densification needs higher temperature for being activated with respect to grain growth (Figure 12). In this case a fast heating process, like during FS, allows to reach high temperature, where the densification is activated, without significant prior grain coalescence. This leads to the extremely high densification kinetics as a result of the fact that the sintering rates are proportional to $1/G^n$, where G is the grain size and n an exponent depending from the densification mechanisms and usually ranging between 3 and 4 [3]. Therefore, by some point of view FS resembles the so called *fast firing*[3,77]: a firing process, yet applied to different ceramics[78–80], in which the ceramic specimen is introduced in a pre-heated furnace and subjected to a very fast heating.

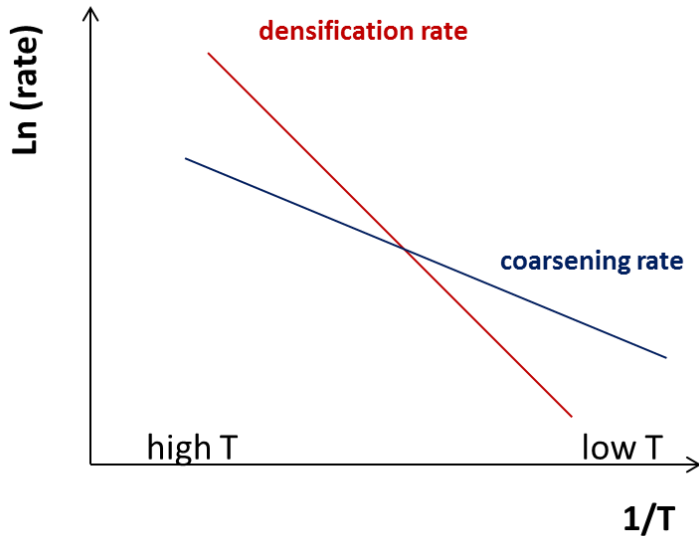


Figure 12: Qualitative behavior for sintering rate and grain coarsening under the assumption that the activation energy for the latter is lower. One can observe that at high temperature densification is enhanced, while at low temperature grain coarsening is more fast. In this case we assume that the sample temperature is homogeneous (grain boundary and grain core are at the same temperature).

The densification obtained during flash sintering is accompanied by a microstructural evolution, similarly to what happens during conventional sintering. In this case much different results were proposed. Ghosh et al. [35] reported that the application of an E-field, without reproducing the flash event, allows a retardation in grain coalescence. Other authors showed that via flash sintering it is possible to obtain dense materials with grains in the sub-micrometric or nanometric scale [6,32–34,81] or it would be possible to arrest abnormal grain growth[58]. However, this could be very likely attributed to the short treating time. As an example in Figure 13 is reported a micrographs of a well sintered GDC tape casted specimen densified by flash sintering with a very limited grain size.

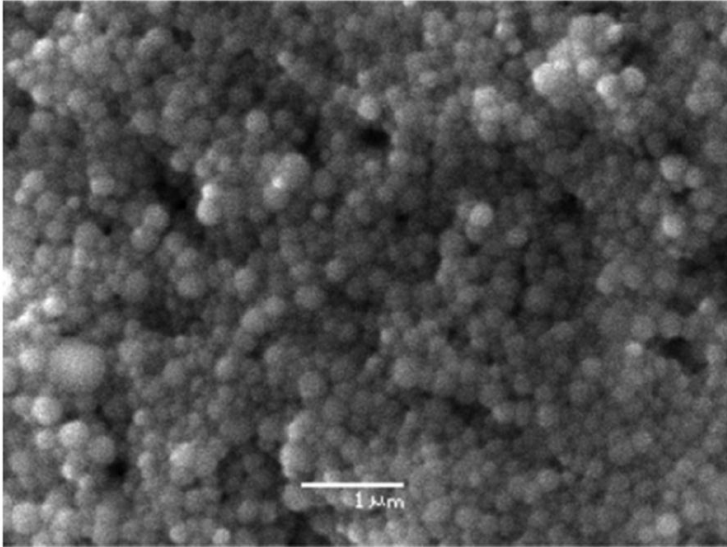


Figure 13: SEM micrograph of a dense flash sintered GDC specimen with sub-micrometric grain size. Taken from [34].

Conversely, Naik et al. studied the effect of a prolonged dwelling time in the III stage of FS on the microstructure evolution of alumina, zirconia and composites [82]. They suggested that during the flash event the activation energy for grain growth do not change significantly; nevertheless, the grain growth is enhanced compared with conventional sintering. Thus, they suggested that this could be related to an increase of defect population. Also other authors observed abnormal grain growth in field-assisted processes [83].

The results in direct current are quite complex. In fact, microstructural asymmetry was reported when comparing anode and cathode of flash sintering specimens. Qin[48] and Kim et al.[49], working with 3YSZ, observed that the grain size at the cathode is much larger than in other parts of the material (Figure 14). This has been attributed to the fact that close to the cathode the material could be partially reduced as a result of an electrolytic reaction pushing electrons in the ceramic, reducing the

oxidation state of the cations. This would decrease the energy barrier for diffusion and enhance, locally, grain boundary mobility[48,49].

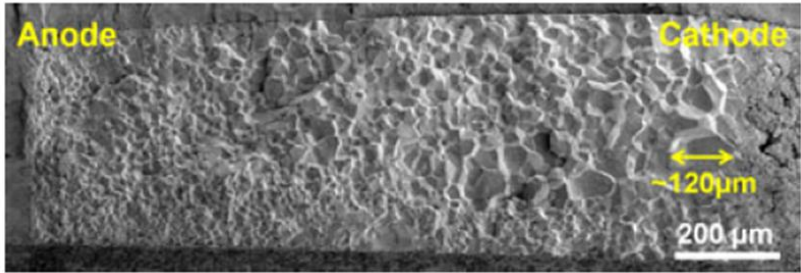


Figure 14: SEM micrograph on a 8YSZ flash sintered specimen showing a strong microstructure asymmetry (24 h at 1250°C, 50 A/cm²). Taken from [49].

Surprisingly, completely different results were reported by Zhang et al. [15] who observed abnormal grain growth at the anode when working with ZnO [15]. They explained such a behavior assuming that cation vacancies could be formed at the anode according to:



These reactions increase the cation vacancy population at the anode and, being cation diffusion controlling grain growth rate, this results in a faster grain coarsening. However, in a recent work carried out on flash sintered zinc oxide it has been shown, via catholuminescence, that the main defect introduced by flash sintering in the crystal structure are anionic vacancies [84]. Zhang and co-workers also reported that this asymmetry is much reduced when a liquid phase is added for promoting sintering[15].

An indirect observation of the microstructure, especially the grain boundary structure, has been carried out in flash sintered YSZ specimens using impedance

spectroscopy. However, the reported data are contradictory. Du et al. reported that both bulk and grain boundary impedance response are similar in conventional and flash sintered specimens[85]. M'Peko et al. suggested that in flash sintered sample the grain boundary thickness is lower and characterized by higher defect concentration than in conventional materials [86]. Finally, they have shown that the specific grain boundary conductivity is higher in flash sintered specimen. Results consistent with those provided by M'Peko were observed also by Liu and coworkers[87]. These results could be explained based on the theory of Frenkel pairs nucleation. However, the partial reduction of the oxide, increasing oxygen vacancy population, is also coherent and probably it provides a better explanation. In fact, Du et al. have carried out FS using AC field which do not lead to any reduction, so they have found strong affinities between flash sintered and conventionally sintered YSZ. Conversely, M'Peko, Liu and coworkers carried out a DC flash sintering experiment; which lead, even in short treating time to a modification of the material structure.

1.4.3 Electrical behavior

The electrical resistivity drop is one of the main characteristic of the flash event. This results in a non-Arrhenius behavior when plotting conductivity or electrical power dissipation vs. the inverse of furnace temperature. This behavior was been observed on different materials as shown in Figure 15.

The Arrhenius behavior in Figure 15 is represented by the region where the power dissipation follows a straight line (low temperature, right side of the plots); however, when the onset condition for flash sintering is reached, an abrupt increase in power dissipation is observed and electrical conductivity rises.

Raj pointed out that this deviation always happens in a quite narrow specific power dissipation range (10 - 50 mW/mm³), even changing the tested material and the onset furnace temperature of hundreds of Celsius degrees[88]. This confirms that power dissipation and Joule heating are very likely the trigger for the flash. However, Raj has also concluded that Joule heating is a necessary condition for the flash event, but not sufficient[88]. The interpretation of the electrical data during flash sintering are quite difficult since it would be necessary an accurate estimation of the

sample temperature, which is not yet possible. In addition, a general conclusion cannot be drawn because in each material different conduction mechanisms are activated. Nevertheless, some attempts were done; but the published results are not in agreement each other's.

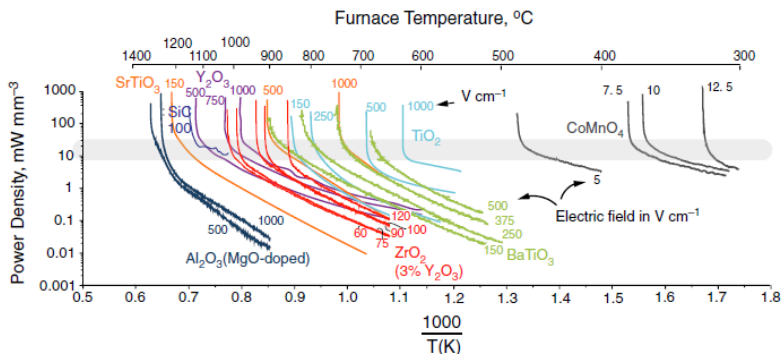


Figure 15: Power dissipation as a function of the inverse of furnace temperature for different materials. The furnace heating rate was 10°C/min and the sample geometry was dog bone-like, the span between electrode was 20 mm and the cross section approximately 3x 1.6 mm². Taken from [88].

Yoshida et al. studied the conductivity of Y₂O₃ during the DC flash experiment using a pyrometer for measuring the sample temperature[69]. They pointed out that the activation energy for conduction remains unchanged during the flash, suggesting that no different conduction mechanisms get activated. However, they have also observed that during FS the conductivity rises more than what would be expected from the temperature measurements (the difference is in the order of a factor ~ 3). Therefore, they concluded that it is possible that Joule heating alone could not explain the conductivity evolution and other athermal effects (i.e. defect generation) can be pointed out. Raj[65] estimated the activation energy for conduction (Q) in 3YSZ during the flash using the data form AC experiments reported in [13]. He calculated Q for conduction to be only 0.46 eV; much lower than the activation energy for ionic conduction. Thus, he suggested that during the flash the conductivity is mainly electronic. Nevertheless, also the band gap for electron promotion in YSZ is

much higher than the measured value for activation energy [89–91]. Jha et al. reported a decrease of the activation energy for conduction in titania from 1.6 eV to 0.6 eV, before and after a DC flash, respectively. They have also concluded that this decrease is due to the activation of electronic conduction in the flash state. Du et al. measured the electrical behavior of 8YZS during the steady stage of FS in AC, taking in account also of the porosity evolution during the process. They have found that the material, even in the flash state, does not deviate significantly from the expected Arrhenius behavior. So, they have concluded that FS is process mainly driven by Joule heating.

Literature results on this point are often controversial. What it is possible to suggest, at least in DC is that a partial reduction of the material can take place rising electronic conductivity and lowering the activation energy for conduction. A reduction of Q, increasing the conductivity with respect to the stoichiometric oxide, has already been observed in partially reduced YSZ[43]. The fact that Du et al. observed a more conventional behavior can be due to the application of a AC field, which do not lead to oxide reduction.

1.4.4 Light emission

Light emission is a key point, always observed during the flash event. We can find a first report about this argument in a paper by Muccillo et al. [92]. They showed a strong correlation between the photoemission in YSZ and SnO₂ and the electric current flow. They suggested that such a phenomenon could be related to antiparticle gaseous discharge. More recently, photoemission spectra have been recorded on different materials in the UV/VIS region: YSZ[18], SrTiO₃, KNO₃ and SrTiO₃/ KNO₃ composites [20]. The authors suggest that such a phenomenon is related to electroluminescence[18,20], being a result of electron-hole generation and recombination during flash sintering[18]. Nevertheless, no further information are provided indicating which electronic transitions are at the base of the phenomenon. In addition, if we compare the spectra obtained on different materials (Figure 16), we can observe that they are pretty similar. If the light emission was due to electroluminescence it would indeed depend from the electronic structure of the

material; thus, we would expect that different materials generate different spectra. This has not yet been observed during flash sintering.

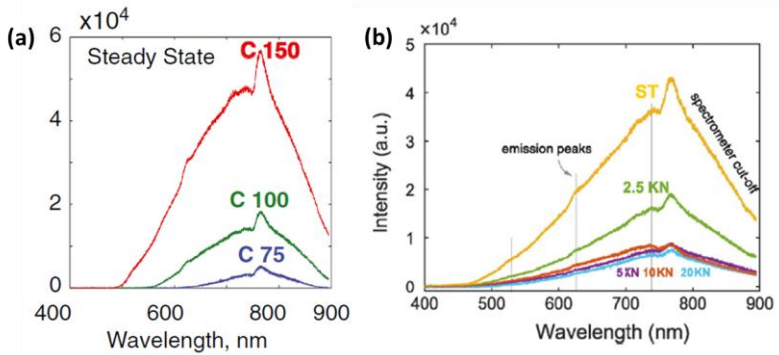


Figure 16: UV/VIS photoemission spectra obtained on YSZ using different current limit (a)[18] and on strontium titanate, potassium niobate and teir composites (b) [20].

Also NIR light emission was measured during flash sintering of YSZ[17]. The authors highlighted the presence of two luminesce peak at ~ 1175 and ~ 2250 nm, as shown in Figure 17(a). They stated that this spectrum is not compatible with the Black Body Radiation (BBR); hence, they provided an interpretation based on electroluminescence. The authors also argued that this can be linked to the Frenkel pairs formation: the defect would be ionized in neutral vacancies and interstitials forming electron-holes; those recombination allows the photoemission. Generally speaking, it seems strange that electronic transition could emit light in the IR; being their transition usually much more energetic[93][89]. We should also consider that each body, if heated, starts to emit light as a result of the well-known thermal radiation, based on black body[94]. Often the photoemission is scaled from the theoretical BBR of a factor called spectral emissivity, which is a function of the wavelength. Therefore, the light emitted can present features different from that would be expected by the black body theory. Figure 17(b) compares the theoretical emission (BBR) and the measured one for a single crystal of 13.5YSZ [95]. It is possible to notice that for low wavelength the differences between the two spectra are very strong and some peaks can be observed. So, we cannot exclude that what

was measured during flash sintering of YSZ is just a result of the combination of BBR and a spectral-dependent emissivity. The spectra in Figure 17(a) can be also compared with the Nernst glower emission; however, very poor correspondence can be found with the Nernst lamp spectra reported in [96].

Finally we can observe, from Figure 17(a) that the relative intensity of the two peak changes with the estimated sample temperature: the spectra obtained at low temperature present a relatively stronger signal at ~ 2250 nm, whereas those obtained at higher temperature show a stronger peak at ~ 1175 nm. This would be coherent with the BBR theory: increasing sample temperature the radiation at low wavelength would grow faster.

A definitive conclusion on this point can not be drawn; however, it seems that the effect of BBR on photoemission during FS is much stronger than what until now considered.

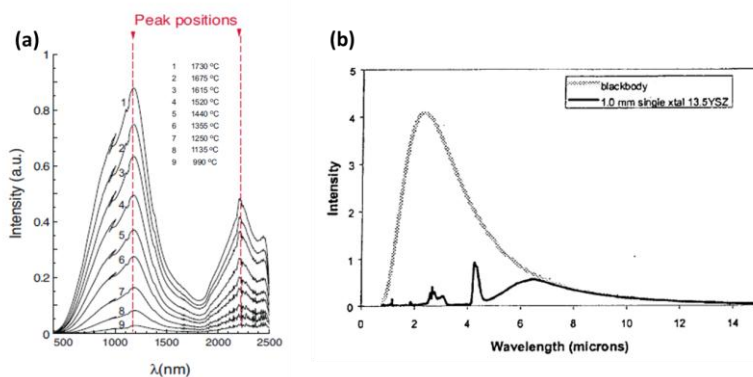


Figure 17: NIR light emission during flash sintering of 3YSZ (a)[17]; spectral emissivity of 13.5YSZ 1 mm thick single crystal (100) at 1000°C (b)[95].

1.4.5 Textures and new phases

Textures and new phase formation was observed only on few materials during DC flash sintering; therefore, we cannot state that are a characteristic of flash sintering. Nevertheless, the results on this argument are very interesting and it deserves to be cited. Texture formation during the flash sintering was described by Jha et al. on

titania[21]. They reported that when the field was switched on the relative intensity of the diffraction peaks immediately changes, and quickly disappears when the field was switched off. The fact that the transformation is not time dependent suggest that it is not based on diffusion, but it is likely related to local atoms displacement from their original position. The results were explained assuming that field-induced crystal defects get formed and they segregate forming clusters on preferential crystallographic orientations.

Lebrun et al. have studied the formation of a new pseudo-cubic second phase during the III stage of flash sintering of YSZ[22]. They concluded that this phase formation can not be due to the Joule heating. In this case the formation of the new phase is time dependent, suggesting that it is based on nucleation and growth phenomena and on atomic diffusion. If the flash experiments are repeated the peak of this new phase gets stronger, this being probably related to some residual effect of the flashes on the structure (like crystallographic defects or nuclei of the pseudo-cubic phase)[22]. The interpretation of such results is still not completely clarified. For instance it would be interesting to understand if these effects are field or current induced. In our opinion this point is yet not clear being the phenomena observed in the III stage of FS when a significant current flows in the system. Additionally, a comparison with AC flash sintering could shade some light on the process.

1.5 Materials densified by flash sintering

Starting from 2010, different ceramic materials have been subjected to flash sintering (Table II). These materials are characterized by a wide range of electrical properties: ionic conductors, protonic, cationic and electronic conductors, insulators, composites, semiconductors. Both oxide and covalent ceramics, have been successfully densified by FS.

Table II: Flash sintered ceramics.

Oxides	Non-Oxide Ceramics
--------	--------------------

<p>3YZS [6,13,14,17,18,22,28,48,62,63,71,86,87,97], 8YZS [7,8,47,66,72,73,85,92], Al₂O₃/TZP composite [41,56,82], Al₂O₃-Y₃ Al₅O₁₂-ZrO₂ eutectic ceramic [98], BaCe_{0.8}Gd_{0.2}O_{3-δ} [99], β-Al₂O₃ [100], BaTiO₃ [81,101], BaZr_{0.1}Ce_{0.7}Y_{0.1}Yb_{0.1}O₃ [102] , CaCu₃Ti₄O₁₂ [103], Co₂MnO₄[24,60,68], GDC [32–34,59], HA [104], K_{0.5}Na_{0.5}NbO₃ [31], K₅NbO₃ [12,20], K₅NbO₃ / SrTiO₃[20], (La,Sr)(Co,Fe)O₃[24,76], MgO-doped Al₂O₃ [39], Mn(Co,Fe)₂O₄ [61], Ni²⁺-doped Y₂O₃[67] NiO/YSZ - YSZ multilayer for SOFC [38], N and V-doped TiO₂ [105], SDC [59], SiC whiskers reinforced ZrO₂ [106], SnO₂ [83], SrTiO₃ [20,58], TiO₂ [21,107], TiO₂ / Al₂O₃ [108] Y₂O₃[69], ZnO [15,64,84,109], ZnO / Bi₂O₃ [15].</p>	<p>α-SiC [110–112], B₄C[113,114], β-SiC [110,111], β-SiC / B₄C [110,114], β-SiC/YAG[115], MoSi₂ [11], SiC [23,116], SiC / Al₂O₃ - Y₂O₃ [23], SiC / Al - B₄C - C[23], ZrB₂ [11,117,118], ZrB₂ / MoSi₂[11].</p>
---------------------------------------------------------------------------------------------------------------------------------------------------------------------------------------------------------------------------------------------------------------------------------------------------------------------------------------------------------------------------------------------------------------------------------------------------------------------------------------------------------------------------------------------------------------------------------------------------------------------------------------------------------------------------------------------------------------------------------------------------------------------------------------------------------------------------------------------------------------------------------------------------------------------------------------------------------------------------------------------------------------------------------------------------------------------------------------------------------------------------------------------------------------------------------------------------------------------------------------------------------------------------------------------------------------------------------------------------------------------------------------------------------------------------------------------------------------------------------------------------------------------------------------------------------------------------------------------------------------------------------	------------------------------------------------------------------------------------------------------------------------------------------------------------------------------------------------------------------------------------------------------------------------------------------------------------------------------------------------------------------------------------------------------------------------------------------------------

We can say that the only constraints that the material should satisfy for being subjected to flash sintering are:

- i. The material should have a negative resistivity temperature coefficient. This allows an increase of current flow when the specimen is heated, triggering the thermal runaway.
- ii. The material should be enough conductive in order to generate the power dissipation needed for triggering flash sintering.

Recently, this technology was extended to glasses. McLaren et al.[119] have shown that the flash event can be generated in alkali-silicate glasses, with strong photoemission, resistivity drop and Joule heating. In this case an abrupt drop in glass viscosity is also observed (Figure 18); therefore, they named the process “electric field-induced softening”.

Such result is very interesting and it has opened new application fields for field-assisted processes. In fact, it deserves to be pointed out that a large variety of advanced ceramics and almost all traditional ones are sintered with the addition of a glassy phase, which provides a liquid at high temperature, responsible for liquid phase sintering mechanisms. The combined effect of electric field-induced softening and flash sintering can be a new research field for ceramists.

On these bases, in 2015 Gonzalez-Julian et al. studied the effect of a moderate field on the sintering behavior of a calcium-aluminum-silicate glass-containing alumina[120]. They concluded that the field application accelerate the densification of the ceramic; nevertheless, the moderate field application do not reproduced the flash event in almost all the cases.

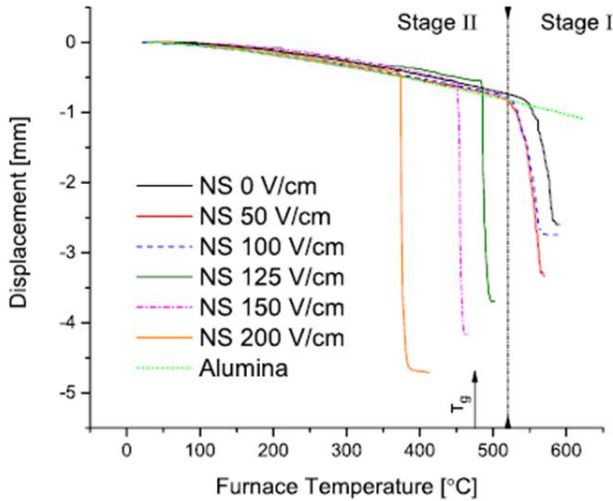


Figure 18: Electric field-induced softening in a sodium-silicate glass using different field strength. Taken from [119].

1.6 Flash sintering and related technologies

In this section the application of flash sintering to geometries different from those usually studied are analyzed (Figure 3) together with other technologies based on similar processes.

1.6.1 Flash sintering of tape casted layers

Flash sintering was applied to tape casted ceramic layers, with possible application in the field of solid oxide fuel cells (SOFC). In particular, nanograined GDC tape was densified by flash sintering[34]. The material resulted well densified with grain size well below 1 μm .

Francis et al. sintered a anode-electrolyte multilayer for SOFC. The multilayer was constituted by NiO/YSZ anode and cubic zirconia electrolytes. The multilayer was densified at furnace temperatures lower than 1000°C. The electrolyte microstructure

was dense with limited closed porosity, whereas the anode was still porous. Such microstructure is the ideal one for this kind of application.

Additionally, they showed that flash sintering obviate the problems related to constrained sintering, consistently with other experimental findings [108]. The result were attributed to the Frenkel pairs generation within the grains that would allow a faster relaxation of the shear stresses. For details see [108]. Nevertheless, one can also suggest a partial contribution of creep stress relaxation due to the very limited grain size obtained during the densification by flash sintering.

1.6.2 Travelling electrodes

Probably, current concentration along preferential paths is one of the main problems observed in flash sintering experiments. In fact, current concentration is responsible for inhomogeneous microstructure [27]. This is indeed limiting an industrial application of this technology.

Today, continuous flash sintering systems are being developed. These involve rolling or sliding electrodes moving with respect to the green specimen. In this case the contact between the ceramic and the electrode is virtually reduced to a line. The motion of this line on the specimen, where FS takes place, allows the densification of quite large pieces. A possible problem related to this technology consists in the fact that an interface between a sintered (shrunk) and a not sintered (not shrunk) part is formed; thus, the differential deformation could produce damages in the green body. However, in May 2015 a first industrial application of FS has been demonstrated by the UK company Lucideon: they were able to sinter a whiteware floor tile 15 x 15 cm² at a temperature ~500°C lower than the conventional one[57].

1.6.3 Hyper-flash and double flash

Steil and co-workers named hyper-flash a flash sintering process with very limited soaking time in current control (1-2 s)[73]. In this way the system does not have time for reaching the equilibrium condition typical of the III stage of flash sintering. In hyper-flash experiments usually very high power peak are used, in the order of 1000 mW/mm³ or more, this for ensuring a very fast heating process within a short time. Hyper-flash experiments can be repeated to enhance densification. In this case the

process is defined as double-flash and it has been proven to easily lead to full densification in 8YZS[73].

1.6.4 Contactless Flash Sintering (CFS)

In 2015, Saunders and co-workers developed the so called Contactless Flash Sintering (CFS)[114]. This technology allows to reproduce flash sintering using electrodes that are not in touch with the ceramic specimen. For this purpose plasma electrodes were used as shown in the sketch in Figure 19. The arc plasma carries the current, through electrons and ion motion, from the electrodes to the specimen. Being the sample in series with the arcs in Figure 19, the current is also forced to flow within the ceramic, reproducing the flash event. Therefore, the ceramic is heated both for the contact with the hot plasma and for an internal heat generation by Joule effect. The obtained heating rates in CFS are extremely high, approaching $20,000^{\circ}\text{C}/\text{min}$ [114].

This technology was applied to SiC, B₄C and SiC/ B₄C composites. The results have shown an optimal densification for B₄C and SiC/B₄C composites in few seconds (~ 3 sec). Conversely, pure SiC has reached lower density. This has been attributed to sublimation/condensation of SiC close to the pores ($T > 2000^{\circ}\text{C}$)[114]. The formation of SiC vapours, constitute by Si, Si₂C, SiC₂, leads also to the growth of particular oriented structures. In fact, platelets SiC crystals have been observed in contactless flash sintered specimens; their growth has been attributed to physical vapor transport mechanisms[112].

The main advantages of contactless flash sintering consist in the fact that the material is not contaminated by the physical contact with the electrodes and no conductive pastes are needed to reduce the contact resistance. In addition, this system can be employed for developing a continuous sintering process by sliding the specimen with respect to the plasma arc [114]. One can also observe that the extremely high heating rate achieved in CFS are suitable for densified metastable or out of equilibrium materials.

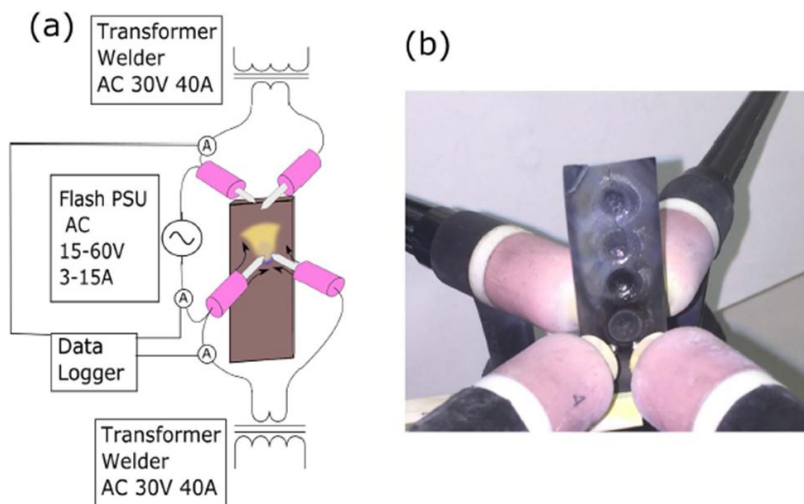


Figure 19: Experimental set-up for contactless flash sintering (a) and a picture of the used system (b). Taken from [114].

1.6.5 Flash Spark Plasma Sintering (FSPS)

Several attempts have been done for bridging the gap between flash sintering and other field-assisted technology like SPS. In particular, some papers have been focused on the possibility to use SPS machines for reproducing the flash event. In this way it would be possible to couple flash sintering with pulsed current and pressure application.

In 2014 Grasso and co-workers published the first work on the so called Flash Spark Plasma Sintering (FSPS)[117]. The same machine used for SPS is used also for FSPS treatments. The basic difference between the two technologies is that the latter does not employ a graphite mold. The sample is just placed between the two graphite punches and the current is forced to flow through the ceramic, allowing the flash event. In FSPS experiments extreme heating rates are reached ($10^4 - 10^6$ °C/min), so the obtained material might have characteristics far different from the equilibrium ones[121]. If the material is too resistive at low temperature for ensuring the current flow, a graphite felt can be placed between the punches in order to pre heat the sample at temperatures at which it becomes conductive. Unlike the

conventional FS experiments, FSPS is a pressure-assisted technology. For this reason, the specimens are usually pre sintered in order to ensure a sufficient mechanical strength.

FSPS is a very attractive technology basically for two reasons:

- i. It allows to produce quite large (tens of grams) crack and defect free samples[117]. The sample dimension is actually one of the main limitation of FS, that is at least partially overcome by FSPS.
- ii. It allows a drastic reduction of processing time (98%) and energy consumption (95%) with respect to conventional SPS[117].

In the last two years many papers have shown the applicability of FSPS at different materials: ZrB₂ [117], SiC[111][116], magnetic materials [122], B₄C [123], YSZ[97], TiB₂ [121], Mg₂Si [121]. Particular interest has been risen about flash SPS of SiC-based materials. In fact, it has been shown that during the process strongly oriented microstructures are formed Figure 20, as a result of the high temperature gradients formed between the core of the specimen and the graphite punches[110]. These gradients allow crystals growth via Physical Vapor Transport: SiC sublimate where the temperature is higher and condensate where the material is colder.

The flash event has been reproduced in an SPS machine also by Zapata-Solvas and co-workers. They do not remove the die like in a typical FSPS experiments, but they forced the current to flow in the specimen using insulating alumina felt placed between the graphite die and the punches[11].

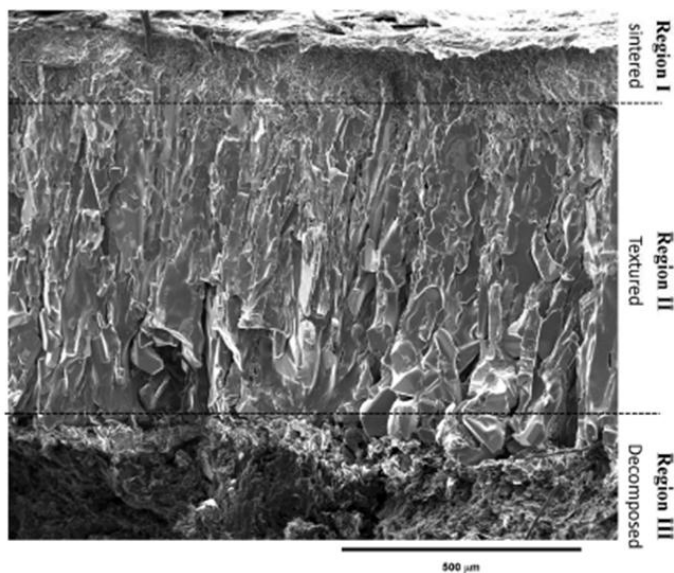


Figure 20: Textured SiC obtained by flash spark plasma sintering. Taken from [110].

1.6.6 Field-Assisted Sintering Technique (FAST)

FAST is a sintering technology where the sintering process takes place under an electric field application. Also, SPS is a kind of FAST. Nevertheless, when dealing with flash sintering experiments it is usually referred to a sintering regime that do not show the flash event. Therefore, in FAST regime the field is too low for reproducing the power needed for the thermal runaway.

Although, FS is not observed and Joule heating is substantially negligible the field application enhances the densification. In Figure 21 the two sintering regime are highlighted. If the field exceed 60 V/cm FS is observed with an almost instantaneous densification. In the case of lower field strength FAST takes place[6]. In FAST regime the densification can be anticipated of $\sim 200^{\circ}\text{C}$ with respect to conventional process. This behavior, observed both using AC and DC field, has been attributed to the delayed grain growth observed in zirconia under weak electric field[124][125]. In fact, smaller grains accelerate densification according to the well-known sintering mechanisms[3].

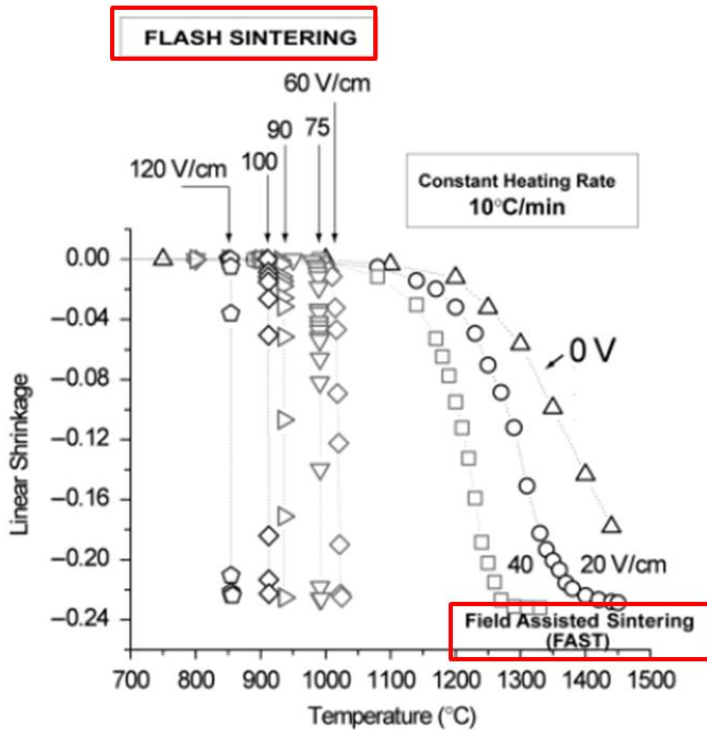


Figure 21: FS and FAST regime in YSZ upon constant heating rate experiments (10°C/min). Modified from [6].

1.6.7 Flash reactions

Flash sintering has been applied to composite powder compacts that upon sintering react forming new phases by solid state reactions. In particular the alumina-titania system has been studied, showing that an aluminum-titanate (Al_2TiO_5) is formed during the III stage of flash sintering[126]. The authors estimated the specimen temperature measuring the cell parameter by diffraction, demonstrating that a complete conversion to Al_2TiO_5 can be obtained in 5 min at 1250°C. A conventional treatment at such a temperature would need 300 min or more for completing the reaction[126]. Therefore, the results suggest that the electric field application enhances the reaction kinetics of ~ 60 times.

2 Aim of the work

Up to date, the research on flash sintering has been mainly focused on ionic and electronic conductors and on semiconductors. Only one work has investigated the flash sintering behavior of insulating materials like high purity and MgO-doped alumina [39]. Nevertheless, many technical ceramics (i.e. refractories, high temperature materials...) are resistive. This represents an evident lack in the scientific knowledge of this process.

Another point that has not been deeply investigated yet is the flash sintering behavior of materials constituted by the simultaneous presence of a crystalline and glassy phase. Such materials represents the larger part of ceramics market: many advanced ceramics are sintered with the addition of a glass for promoting liquid phase sintering, while all the traditional ceramics are characterized by a vitrification process upon sintering. Additionally, the recent findings on Electric Field-Induced Softening has increased the scientific interest on this topic.

In the present work, we tried to fill part of these two gaps. At first, we studied the flash sintering behavior of a resistive technical ceramic like alumina, which is widely used in many applications as pointed out by the huge world production exceeding 50 million tons per year[127]. Flash sintering experiments were carried out on commercially pure alumina CT3000SG (99.8% pure), manufactured by ALCOA. Then, we extended our analysis to a common mixed system containing both crystalline (alumina) and glassy (magnesia silicate glass) phase. The experimental and analytical activity was carried out with the aim to clarify and understand some of the several mechanisms behind flash sintering.

The aim of this work is therefore to extend the application fields of flash sintering to two widely diffuse ceramic systems and to deepen the mechanisms involved in the process.

3 Experimental procedures

3.1 Materials and samples preparation

In this work, low soda reactive α -alumina from ALMATIS - CT3000SG, 99.8% pure, was used. The nominal composition of the powder is reported in Table III. The powder is characterized by $d_{50} = 600$ nm and a specific surface area of 7.8 m²/g.

Such alumina powder is commercially available and widely used because of its good sinterability. At the same time it seems suitable for flash sintering experiments because of the presence of several impurities, which may enhance electrical conductivity. Higher purity alumina has already been subjected to FS experiments pointing out that they are too resistive for triggering the flash event[39]. A more detailed discussion of the material composition and its effect on flash sintering, compared with previous experimental results [39], is reported in “4.1.1 Densification behavior and microstructural evolution”.

Table III: Nominal composition of the alumina powder used in in this work.

	[wt%]
Al ₂ O ₃	99.8
Na ₂ O	0.03
Fe ₂ O ₃	0.015
SiO ₂	0.015
MgO	0.040
CaO	0.015

The magnesia-silicate glass-containing specimens were obtained by mixing alumina (ALMATIS CT3000SG) with glass powder obtained via sol-gel method. For this purpose TEOS (Sigma Aldrich) and magnesium nitrate hexahydrate (Sigma Aldrich) were used as precursors of silica and magnesia, respectively. TEOS and magnesium nitrate were dissolved in isopropyl alcohol. Then, an aqueous solution containing 10% NH₄OH was added, allowing TEOS hydrolysis. The suspension was dried overnight in oven at 100°C. The obtained powder were mixed with alumina and ball

milled in isopropyl alcohol using alumina spheres for 3 h. The suspension was then dried and calcined in a muffle furnace (Nabertherm P180) under static air atmosphere using heating rate of 10°C/min up to 750°C and dwell time of 30 min. The nominal composition of the obtained material was: 90 wt% Al₂O₃, 8wt% SiO₂ and 2 wt% MgO. Hence, the glass load in the material was 10 wt% and the composition was 80 wt% silica and 20 wt% magnesia.

For comparison, following the same procedures, also high purity silica glass was obtained and added to alumina. In this case the nominal composition of the material was 90 wt% Al₂O₃, 10 wt% SiO₂.

The three different powder (pure alumina, magnesia-silicate and pure silica-containing alumina) were then mixed with some water as a binder (6 – 7 wt%). The specimens were shaped by uniaxial pressing in dog bone shape at 120 MPa, using the geometry reported in Figure 22. The sample thickness varies from 2.8 to 3.3 mm. The chosen geometry was substantially the same of that used in many flash sintering experiments like those reported in Figure 15; unless the sample thickness used in the present work was slightly higher.

Two platinum wires were forced into the holes on the opposite side of the dog bone (Figure 22) and act as electrodes. In order to improve the contact between the metal wires and the ceramic a conductive paste was added. In almost all the cases a platinum paste (Sigma Aldrich) was used. Also silver paste (Agar Scientific) and carbon cement (Plano GMBH) were used for comparison. Pastes different from Pt were used in some experiments (as reported in Section “4.1.5 Electrode Material Effect”).

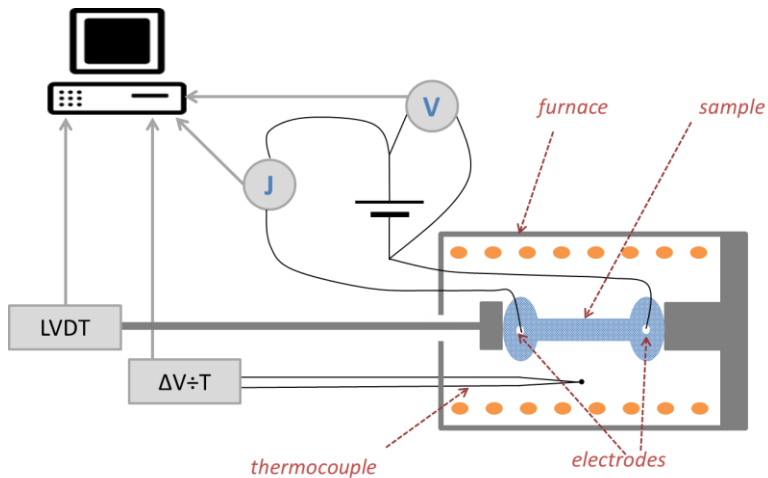


Figure 23: Experimental set-up for constant heating rate experiments.

The system starts to work in voltage control in the range 250 – 1500 V/cm. After the flash event the system switches in current control and the current was let to flow in the specimen for 2 min. After that the power supply and the furnace were shut down. Currents in the range 0.6 – 7 mA/mm² were used for the experiments.

The electrical parameters (current and tension) were recorded using a digital multimeter (Keithley 2100). Current density, field and specific power dissipation were calculated taking in account of the actual sample size (assuming isotropic shrinkage). If these values are calculated with respect the green body dimension they are defined in the text as “nominal”.

3.3 Experimental set-up n. 2

The experimental set-up used for isothermal experiments is reported in Figure 24. In this case the sample were subjected to a pre-sintering cycle prior to the flash sintering experiments. Different pre-sintering temperatures were chosen for alumina sample in order to check the effect of the residual porosity on the flash sintering behavior of the material: 1250, 1350, 1450 and 1550°C. The pre-sintering cycle was operated in a muffle furnace (Nabertherm) using an heating rate of 10°C/min and soaking time of 2 h.

After pre sintering, the specimens were connected by two platinum wires to a DC power supply (Glassman EW series 5 kV–120 mA) and to a digital multimeter (Keithley 2100). The specimen was then introduced in a pre-heated tubular furnace (Nabertherm P330) at 1200°C and subjected to flash sintering using different combination of E and J.

An optical fiber was placed on the bottom of the furnace for recording the optical emission spectra during the flash event. For this purpose two different spectrometer were used: NIR 512 and USB4000 for the NIR and UV/VIS region, respectively. The data in the UV/VIS were recorded using an integration time of 3.8 ms, whereas in the NIR the integration time was fixed in 10 ms. The optical response of the system was properly corrected using a calibration lamp (Avantes, HD2000).

Using this experimental set-up the electrical conductivity of alumina pre-sintered at different temperature was measured at 1200°C using field in the range 500-1500 V/cm.

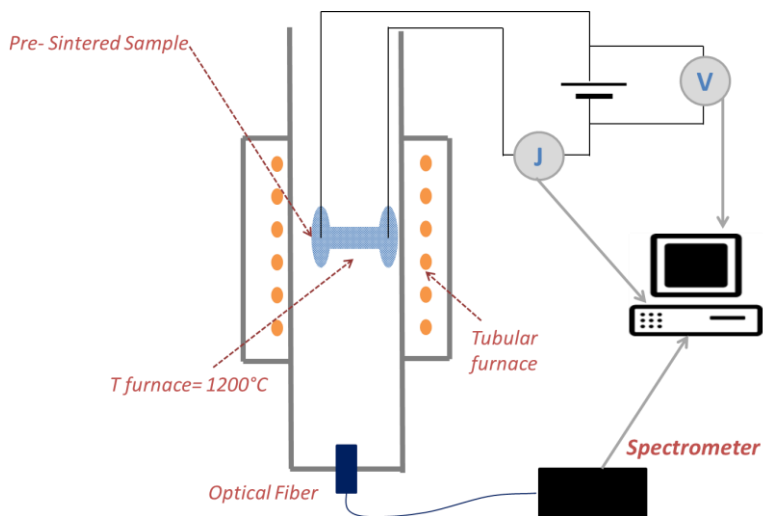


Figure 24: Experimental set-up for isothermal flash sintering experiments.

3.4 Conventional Sintering

Conventional sintering processes were operated in order to study the densification and grain growth phenomena without the field/current effect. These experiments were operated using cylindrical pellets (diameter 13 mm, thickness ~3 mm), shaped by uniaxial pressing at 120 MPa. The samples were sintered in a muffle furnace (static air atmosphere). The heating rate for all the experiments was 10°C/min. Different soaking time and maximum temperatures were employed in the different experiments (reported in the text).

3.5 Characterization

3.5.1 Microstructure

The microstructure of the sintered specimens was characterized by SEM micrographs, using JEOL 5500 and Jeol IT300. The microstructure was studied on fracture surface and free surfaces. The grain size measured using the linear intercept method and repeating the measurement 12 times. In the case of glass-containing specimens, micrographs were taken also on polished and polished/HF-etched surfaces. The etching was carried out using 10% HF water solution for 25 s.

3.5.2 Phase analysis

The mineralogical analysis was carried out by XRD on monolithic sintered specimen using Italstructures IPD3000 diffractometer and Cu K α as X-ray source (excited with 30 mA- 40 kV). A multilayer monochromator was used to suppress k β radiation. The spectra were collected by means of an Inel CPS120 detector. The measurement time was 20 min. The spectra were studied in the 2 θ range from 10 to 70°.

The peak position were identified using the following PDF files: corundum 00-046-1212, spinel 00-021-1152, mullite 00-015-0776, silicon 00-027-1402.

3.5.3 Density measurement

The density of sintered specimens was measured by the Archimedes' method, according to ASTM C 830 – 00 (2006) standard. An analytical balance Gibertini with sensitivity 0.0001 g was used. The standard allows to calculate both the bulk density (mass/geometric volume) and the open porosity percentage (volume of open

pores/geometric volume $\times 100$). The volume of the open pores is estimated by the weight difference between the dry sample and the sample impregnated with water.

3.5.4 XPS

XPS analysis were performed on alumina specimens in order to analyze possible reduction reactions taking place in the oxide during the flash sintering process. For this test Kratos AXIS Ultra XPS machine was used with Al K α (1486.6 eV) X-ray source.

3.5.5 Photoluminescence spectroscopy

The sintered alumina samples were studied by photoluminescence spectroscopy using an excitation radiation of 300 nm and recording the light emitted from the sample in the range 320-500 nm. The spectra were obtained using the instrument Jasco FP6300 equipped with a 150 W Xe lamp. All the spectra were collected with a bandwidth of 5 nm.

4 Results and Discussion

Part of this chapter has been published in:

M. Biesuz, V.M. Sglavo, Flash sintering of alumina: Effect of different operating conditions on densification, *J. Eur. Ceram. Soc.*, vol. 36, n. 10 (2016), p. 2535-2542.
- doi: 10.1016/j.jeurceramsoc.2016.03.021

M. Biesuz, V.M. Sglavo, Field Assisted Sintering of Silicate Glass-Containing Alumina, *Ceram. Engin. Sci. Porc.*, v. 2015, vol. 36, n. 6 (2015), p. 75-81. - doi: 10.1002/9781119211662.ch9

M. Biesuz, P. Luchi, A. Quaranta, V.M. Sglavo, Theoretical and phenomenological analogies between flash sintering and dielectric breakdown in α -alumina, *J. Appl. Phys.* 120 (2016) 145107. doi:10.1063/1.4964811.

M. Biesuz, V.M. Sglavo, Liquid phase flash sintering in magnesia silicate glass-containing alumina, *J. Eur. Ceram. Soc.*, vol. 37, (2017), p. 705–713. doi:10.1016/j.jeurceramsoc.2016.08.036.

4.1 Flash sintering of alumina

4.1.1 Densification behavior and microstructural evolution

The results described in this section are referred to the experimental set-up n. 1, using platinum electrodes.

Figure 25 shows the dilatometric curves obtained by applying different combinations of field strength and current density during the heating process. First of all, one can

observe that the FS event can be reproduced using $E \geq 500\text{V/cm}$; while the sample treated with 250 V/cm is characterized by a sintering behavior very similar to the conventionally sintered specimen (0 V/cm). Hence, we can state that flash sintering can be efficaciously applied to commercially-pure corundum if the field exceeds 500 V/cm . The onset temperature for flash sintering is mainly controlled by the applied field and it progressively decreases by increasing the field strength (Figure 25). It is quite interesting to observe that, using 1500 V/cm , the material densifies at temperature slightly higher than 900°C .

In general, FS temperature measured in this work is $120 - 230^\circ\text{C}$ lower than that recorded by Cologna on 0.25 wt\% MgO -doped alumina (using the same field strength and similar sample geometry)[39]. This result is quite surprising considering that in the present work we used coarser powder ($d_{50} = 600\text{ nm}$, $d_{90} = 3000\text{ nm}$ compared to $100 - 300\text{ nm}$ in[39]) coarser powder being typically responsible for delayed FS phenomenon[62]. Thus, the reasons of the observed behavior shall be identified in the powder composition. Although the total amount of impurities present in the powder used by Cologna et al. is slightly higher (0.25 wt\% respect to 0.20 wt\%) and seem to correspond to MgO only; conversely, in the present work, the powder is characterized by the presence of different cations (Mg^{2+} , Ca^{2+} , Si^{4+} , Fe^{3+} , Na^{+}). This is suggesting that the simultaneous presence of different chemicals allows to increase alumina conductivity leading to the anticipated FS phenomenon. The reason of this behavior can be clarified if one considers that the cationic solubility in corundum is very low[128–130], the solubility of magnesia at $1720\text{--}1880^\circ\text{C}$ being only $75\text{--}175\text{ ppm}$ [130]. This means that almost all magnesia present in the powder used here and by Cologna is not in solid solution and forms a second resistive phase (periclaase or spinel) that does not enhance the conductivity of the system. The simultaneous addition of different chemicals should form a saturated solid solution for each cation; thus it is reasonable to suggest that in this way the total amount of Al^{3+} substituted by aliovalent ions is higher when compared with a system containing only magnesia. The substitution of Al^{3+} with other ions is at the base of conduction in corundum, increasing both ionic and electronic conduction. Elements with valence lower than 3 (like Mg^{2+} , Ca^{2+}) act as electron acceptors [1,131] and promote the formation of oxygen vacancies[131–133], while elements with higher valence (like

Si⁴⁺) act as electron donors [1,131]and promote the formation of aluminum vacancies[133].

Figure 25 points out also that the current limit is the key parameter controlling the sintering rate (i.e. the slope of the dilatometric curve) and the densification. In fact, by increasing the nominal current density much higher linear shrinkage is obtained upon sintering. This can be accounted by the relation between sample temperature and power dissipation (Eq. 10); in fact, during the third stage of FS the system is working in J control and the specific power dissipation is increasing with J.

The samples treated with 500 and 750 V/cm show two main shrinkage events. First, while the system is in voltage control, the dilatometric curves present a downward concavity (as observed also during the conventional sintering processes); but, once the current limit is reached, the concavity of the curves turns upward and FS take place. One can observe in Figure 25 that these samples are already partially shrunk (~2 - 5 %) when the concavity changes; so the densification phenomena are already activated when FS happens. This has an effect on the final density of the sintered body as it will be shown later on. The first part of the shrinkage (downward concavity) is partially due to thermal and field-assisted sintering mechanisms. In fact, well before the flash event and the current limit reaching, the specimens treated with 500 – 750 V/cm are shrinking more than that conventionally treated (0 V/cm). Their dilatometric plots cannot be explained only as a result of the heating process, but a partial contribution of the field on the densification should be highlighted. This behavior resemble the FAST regime described extensively in YSZ under moderate E-Field, where the enhanced densification is explained as a result of the field induced lowering of the grain growth rate[6,124,125].

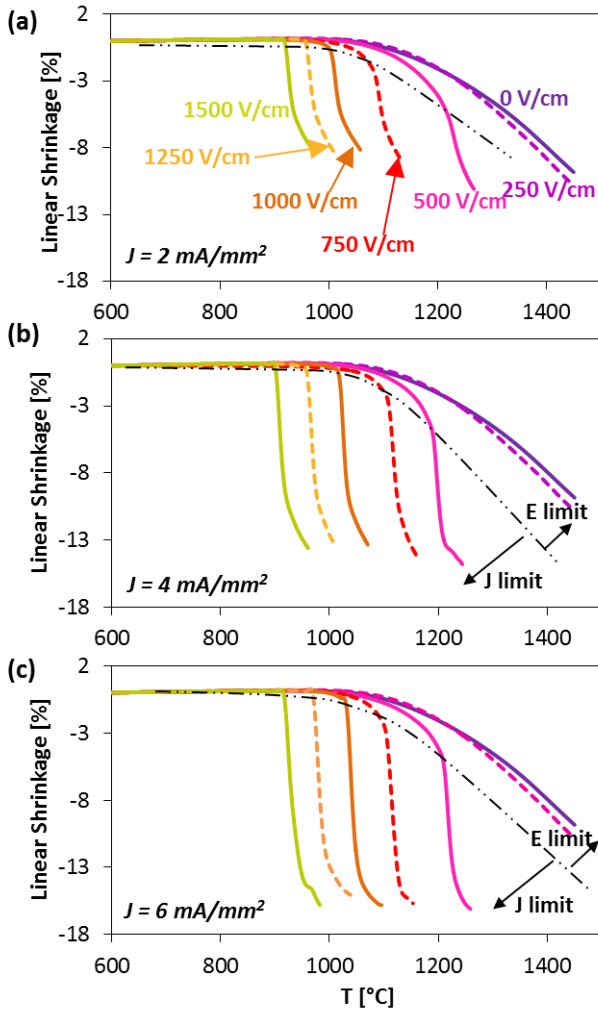


Figure 25: Dilatometric curves obtained using different fields (250 - 1500 V/cm) and nominal current limits of 2 (a), 4 (b) and 6 mA/mm² (c). Modified from [55].

A different behavior can be observed at higher fields (1000 – 1500 V/cm), the current limit being reached when the furnace is at a temperature lower than 1050°C and FS accounting for almost overall densification.

The density measurements on the sintered samples are reported in Figure 26. It can be easily observed that the material become denser by increasing the current limit, coherently with the dilatometric curves reported in Figure 25. If the current limit is high, the physical properties are not influenced by the field strength and the material is substantially full dense. However, in the case of lower current application the density is also partially related to E, the specimens treated with lower field (500 -750 V/cm) resulting more densified. This behavior is based on two reasons:

- i. The samples treated with low field (500 – 750 V/cm) are already partially densified via thermal/field-assisted mechanisms when the flash event happens;
- ii. The samples treated with lower fields are flash sintered at higher furnace temperature and this results also in higher equilibrium sample temperature during the third stage of FS according to Eq 10.
- iii.

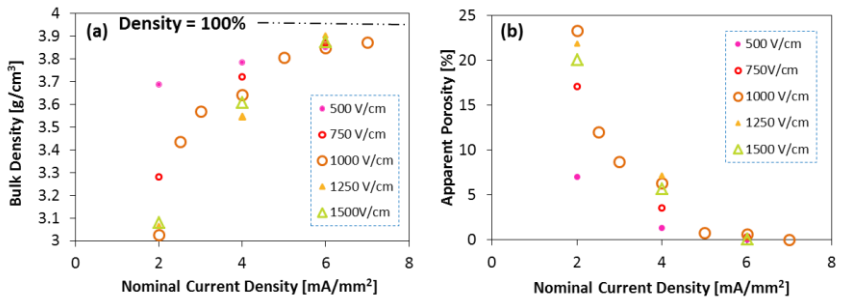


Figure 26: Density (a) and open porosity (b) evolution as a function of the nominal current density. Modified from [55].

The microstructural evolution was analyzed by SEM, as reported in Figure 27. The micrographs refer to fracture surfaces observed in the central part of the gage

section, where the current density can be easily calculated. One can notice that the current limit is the main parameter affecting the final microstructure of the sintered bodies, while the effect of the field strength is less marked. As expected from the previous results, the material becomes progressively denser by increasing the current limit. The grains are all equiaxial and grain growth phenomena are activated in the case of high current application. Therefore, the current application significantly influences the grain boundary mobility, especially considering that everything happens in just 2 min.

The pores location is also changing: in the case of the specimens treated with 2 mA/mm² all pores are located at the Grain Boundaries (GB) while increasing the current breakaway phenomena are observed with grain boundary-pores separation. This is an obvious result of the high grain boundary mobility in the case of high current application. Finally, the fracture mechanism is influenced by the current density and it turns from intergranular (low current) to partially transgranular (high current). This can be due to the grain boundary – pores separation: when the pores are located at the GB the fracture is intergranular and the crack propagates between the grains; but, once the pores get isolated inside the grains, the crack starts to produce cleavages and transgranular fractures. Such transition from inter to transgranular fracture has also been observed in conventionally sintered ceramics[134].

The grain size evolution is reported in Figure 28. One can observe that, according to SEM micrographs, the grain size is controlled by the current limit and the effect of the field is much less important. The plot in Figure 28 is characterized an exponential-like behavior and it was modeled considering the well-known equation for grain growth[3]:

$$G^n = G_0^n + K_0 \exp\left(\frac{-Q}{RT}\right)t \quad (13)$$

where G and G₀ are the grain size at the end and at the beginning of the process, respectively, K₀ is a pre-exponential constant related, Q the activation energy for diffusion across the grain boundary, R the universal constant, T and t the treating

temperature and time, respectively. Using a very rough approximation we can assume that the energy for atoms diffusion across the GB is proportional to the measured power dissipation during FS. However, as it will be shown in section “4.1.2 Electrical behavior” the power dissipation is nearly proportional to J; thus Eq. 13 can be reduce to:

$$G^n = G_0^n + K_0 \exp\left(-\frac{Q}{R C J}\right) t \quad (14)$$

where C is a constant. Moreover, the samples tested in the present work were all treated with the same dwelling time (2 min). Therefore, we can write:

$$G^n = G_0^n + A \exp\left(-\frac{B}{J}\right) \quad (15)$$

where A is a constant incorporating t and K₀. Finally G can be expressed as:

$$G = \sqrt[n]{G_0^n + A \exp\left(-\frac{B}{J}\right)} \quad (16)$$

Using the minimum-square method the experimental data were fitted according to:

$$G = \sqrt[1.9]{0.41^{1.9} + 569 \exp\left(-\frac{30}{J}\right)} \quad (17)$$

Although this relation was built assuming some rough approximations, it can provide a quite good prediction, at least from an empirical point of view, of the grain size evolution during flash sintering. In fact, the blue dashed line in in Figure 28, which is derived from Eq. 17, well fits the experimental data.

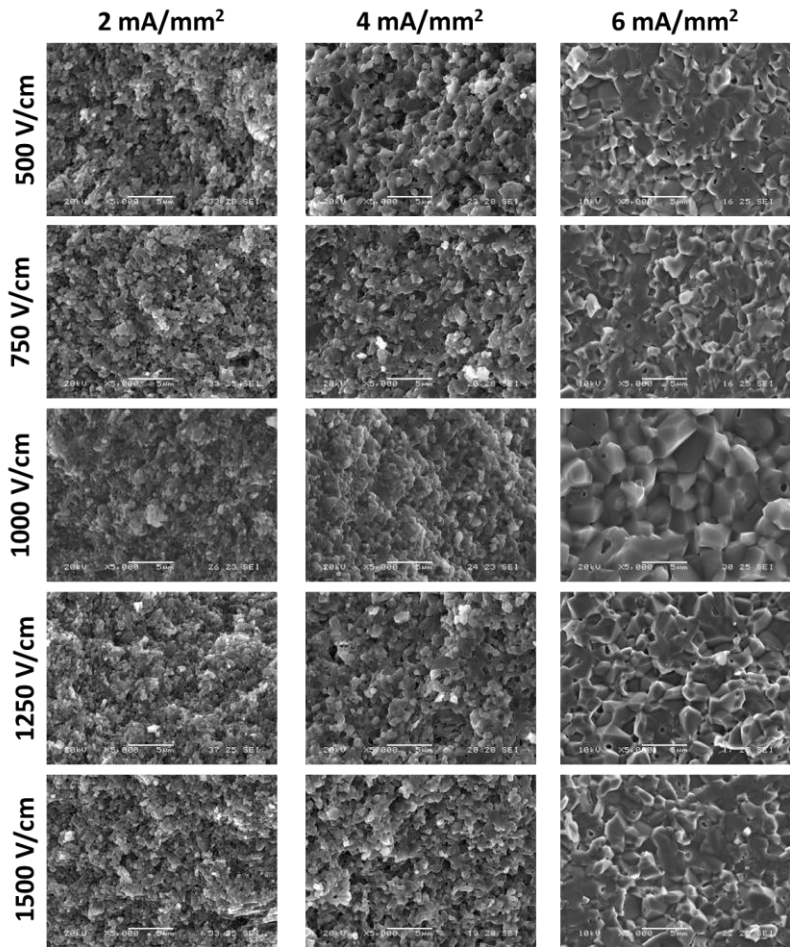


Figure 27: SEM micrographs of flash sintered sample using different combination of E and J.

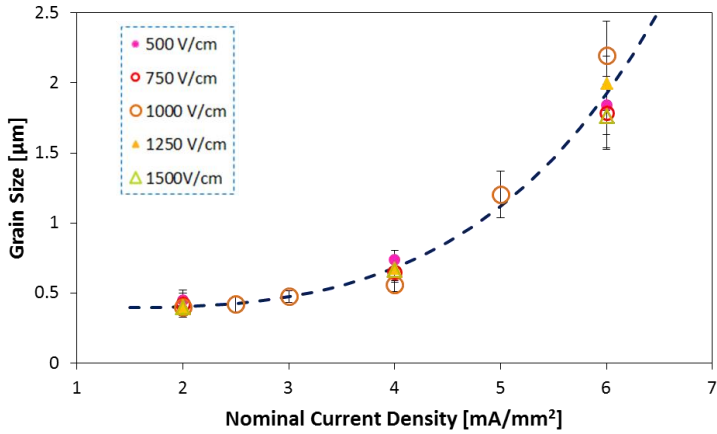


Figure 28: Grain size evolution as a function of the nominal current density, the dark-blue dashes line represent the fitting given by Eq.17.

At this point the densification and microstructural evolution of flash sintered alumina bodies have been well characterized. We can undoubtedly state that via FS it is possible to obtain dense corundum with microstructural features similar to conventionally sintered material but using treatment temperatures significantly lower (nearly 600 °C) and reduced processing times.

Now the open question is: “How much the sample temperature during flash sintering can account for the observed microstructures?”. In order to answer this question we should estimate Joule heating using Eq. 10 and compare the results with what expected in conventional processes. Since the emissivity (ϵ) is unknown we calculate the sample temperature for three values of ϵ in a wide range: 0.5, 0.7 and 0.9. Such value are compatible with the tabulated emissivity of alumina, generally around 0.6 [135,136]. The temperature calculation takes in account the shrinkage that occurs during the process; updating second by second the S and W_m values in Eq. 10.

The results are calculated under the following assumptions:

- i. The sample thickness is considered to be the same in all the gage section;
- ii. Core and surface are at the same temperature during the steady stage of FS[71];

- iii. Grains and grain boundaries are at the same temperature of the bulk of the grain[37];
- iv. Only the data collected in the second minute after the flash event were used in the calculation; with the purpose to be sure that the sample already reached the equilibrium temperature.

According to the assumption (ii) the sample temperature in the III stage of FS can be approximated with its surface temperature. This seems to be a reasonable approximation for two reasons. First, temperature gradients have not been observed by Lebrun et al. in the steady stage of FS on YSZ sample via XRD. They measured only a transient temperature difference between core and surface of $\sim 100^{\circ}\text{C}$ when the power dissipation overcomes 1000 mW/mm^3 . Such condition can be considered an extreme one: in our experiments the maximum power peck was 900 mW/mm^3 and the thermal conductivity of alumina is nearly one order of magnitude higher than that of YSZ. Second, we did not observe any microstructural differences, in terms of grain size and densification, between core and sample surface.

It should also be underlined that the temperature reached at the end of the process is reasonably the higher one. First, in this stage the sample is already shrunk increasing the current density to values higher than the nominal ones. Additionally, according to the power diagram in Figure 10 the sample achieved the higher temperature during the III stage: in fact, after the power peck the electrical power is still higher than the heat dissipated by radiation until the equilibrium is reached. This behavior is confirmed by the fact that the sample decreases its resistivity after the power peck and the light emission gets stronger (4.1.3 Photoemission during Flash Sintering), consistently with a temperature increase. Hence, the temperature values discussed in the followings can be considered the higher reached during FS.

Such values for the different combination of E , J and ϵ are reported in Table IV. The temperatures are strongly influenced by the current limit, while the effect of the field is less important. However, as a matter of fact the temperature is generally decreasing of some tens of Celsius degrees by increasing the field from 500 to 1500 V/cm. This is due to the fact that by increasing the field the sample is flash sintered at a lower furnace temperature; hence, the specimen reaches the equilibrium at a lower temperature (Eq. 10). Much more important is the effect of the current; in fact,

increasing the current from 2 to 6 mA/mm² the sample temperature increases of 200°C or more.

Table IV: Estimated sample temperature [°C] during the third stage of flash sintering for different emissivity values.

$\epsilon = 0.9$		$J \text{ [mA/mm}^2\text{]}$					
		2.0	2.5	3.0	4.0	5.0	6.0
$E \text{ [V/cm]}$	500	1360			1459		1513
	750	1270			1408		1494
	1000	1223	1288	1310	1367	1410	1505
	1250	1222			1350		1433
	1500	1206			1351		1450
$\epsilon = 0.7$		$J \text{ [mA/mm}^2\text{]}$					
		2.0	2.5	3.0	4.0	5.0	6.0
$E \text{ [V/cm]}$	500	1389			1502		1573
	750	1308			1458		1567
	1000	1268	1339	1395	1431	1480	1518
	1250	1273			1409		1503
	1500	1260			1400		1510
$\epsilon = 0.5$		$J \text{ [mA/mm}^2\text{]}$					
		2.0	2.5	3.0	4.0	5.0	6.0
$E \text{ [V/cm]}$	500	1437			1581		1668
	750	1338			1548		1679
	1000	1362	1288	1310	1530	1580	1631
	1250	1343			1511		1620
	1500	1344			1507		1635

These values should now be compared with conventional sintering process. In order to do this, the grain growth of alumina was studied doing thermal treatments in the temperature range 1550-1630°C with soaking time of 2 - 8 h (Figure 29).

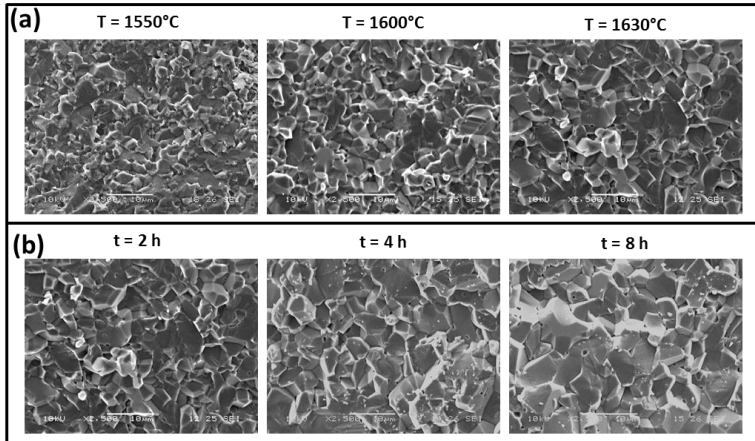


Figure 29: SEM micrographs on conventionally sintered specimens treated for 2 h at different temperatures (a) or at the same temperature (1630°C) for different times (b).

Interpolating the experimental data, the relation describing grain growth during conventional processes was determined as:

$$G = \sqrt[4.1]{0.39^{4.1} + 1.4 \cdot 10^{21} \exp(-92700/T) t} \quad (18)$$

Therefore, it is possible to estimate the temperature needed at the grain boundary for obtaining the same grain size of flash sintered samples by conventional sintering process. This can be done combining Eq.18 ($t = 2$ min) with the grain size measured in flash sintered bodies (Figure 28). The results are summarized in Table V for sample treated with 4, 5, and 6 mA/mm²; the other specimens were not taken into account since the grain coalescence was very limited.

Table V: Estimated sample temperature (T_s) using Eq. 10 (with different emissivity) and the grain boundary temperature measured from grain growth process (T_G).

Current limit [mA/mm ²]	T_G [°C]	T_s [°C]		
		$\epsilon = 0.9$	$\epsilon = 0.7$	$\epsilon = 0.5$
4	1508-1555	1350-1459	1431-1502	1511-1581
5	1630	1410	1480	1580
6	1695-1733	1450-1513	1503-1573	1620-1679

Table V points out that, generally speaking, the temperature needed at the grain boundary for explaining the grain growth observed during FS is in almost all the cases higher than the sample temperature during the process, even assuming a very low value for ϵ (i.e. 0.5). In addition, the spread between the two temperatures becomes larger by increasing the nominal current density. Different reasons can be claimed for explaining the behavior and deserved to be mentioned:

- i. The model used for calculating the sample temperature from furnace temperature and power dissipation is simplified since it assumes that bulk and GB are at the same temperature. Theoretically, the GB temperature could be different from the bulk because of the presence of space charges or because it offers a preferential path for ionic diffusion. However, it is hard to state that significant temperature gradients can occur in micrometric or sub-micrometric scale. The hypothesis of temperature gradients within the grain was rebutted by Holland et al.; they showed via numeric simulation that during FS the differences in temperature between the different microstructural areas are negligible[37].
- ii. At the particle contact points the material melts and during the FS process and *“local melting progress is hierarchical, which assures the preservation of the local melt, as long as other percolative paths for the current flow exist”*[30]. This theory was proposed by Chaim for explaining the rapid densification during FS. The melt would provide a fast diffusion path and

meanwhile the liquid film capillarity should generate a mechanical strength between the particles ensuring a fast densification. This theory is very attractive and provides a good explanation for the densification process; in addition the presence of a melt at the GB could provide the fast diffusion path needed for grain coarsening. However, as pointed out by Narayan the presence of liquid should drastically decrease the driving force for grain growth, resulting in a suppression of GB motion[36].

- iii. The current flow accelerates the diffusion process. This can be related to electrolytic reactions at the cathode and anode producing oxygen vacancies and promoting a partial reduction of the oxide as described by Downs[9]. The high lattice defect concentration enhances the diffusion rates and the grain growth phenomena. Finally, a partial reduction of the oxidation state of the cations could reduce the activation energy for cationic diffusion [48] and electron trapping in oxygen vacancies lowers their migration energy barrier [29].

In order to point out the current effect on densification, some samples (prepared following the same procedures of the FS specimens) were treated by Fast Firing (FF) at temperatures of 1600 and 1650°C (soaking time = 2 -3 min). These temperatures were chosen since they are close to the temperature range estimated for the specimen treated with 6 mA/mm² assuming a low value of ϵ (Table IV).

The fast fired samples were directly introduced in a pre-heated muffle (1600-1650°C) using a platinum wire, with the aim to reproduce the abrupt heating process of flash sintering. Prior to FF, the specimens were pre-sintered using an heating rate of 20°C/min up to 1050°C, simulating the thermal treatment during the incubation of FS. After pre-sintering the sample were polished reducing their thickness ($t < 0.8$ mm); in this way thermal gradients and the heat capacity of the sample were reduced ensuring a fast heating.

The fast fired specimens were characterized by densities in the range 3.47 – 3.68 g/cm³, lower when compared with the densities of flash sintered samples (6 mA/mm², Figure 26). Therefore, even assuming a low value for ϵ , the density

obtained by FS are higher than what would be expected from conventional processes.

In this chapter we extended the applicability of flash sintering to a resistive ceramic; showing the applicability of this innovative sintering technology to nearly pure corundum. Additionally we pointed out that both grain growth and densification during flash sintering appears to be not completely explainable by conventional/thermal sintering theories. Therefore, the results suggest that the current flow can interact with the mass transport phenomena.

4.1.2 Electrical behavior

Understanding the electrical behavior of a material is crucial for the analysis of FS. In fact, the onset temperature for flash sintering depends from the electrical properties; being the more conductive powder compacts flash sintered at lower temperature using the same field. In addition, if a material is too resistive, like high purity alumina, it can not be flash sintered in any case[39].

The specific power dissipation during the incubation of FS, when the system works in voltage control, is shown in Figure 30. At low temperature a linear-like behavior is expected. In fact, the power dissipation can be written as:

$$w = EJ = E^2 / \rho(T) = \frac{E^2 \exp(-\frac{Q}{RT})}{\rho_0} \quad (19)$$

and it can be linearized as:

$$\ln(w) = \ln\left(\frac{E^2}{\rho_0}\right) - \frac{Q}{RT} \quad (20)$$

The plots in Figure 30, even at low T (right portion of the curves), show a certain deviation from the expected linear behavior, i.e. the slope of the curve progressively increases by increasing the temperature.

At higher furnace temperature a strong non-linearity can be observed, the system switches to current control and FS occurs. This non-linear behavior takes place when the system reaches a specific power density of $\sim 25 \text{ mW/mm}^3$. This vale is in the

same order of magnitude when compared with data previously reported on other materials[88].

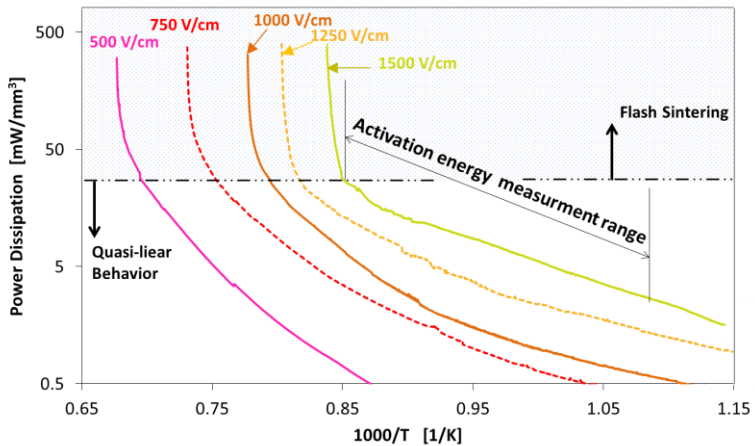


Figure 30: Natural logarithm of the specific power dissipation during the incubation of FS as a function of the inverse of the absolute furnace temperature (Pt electrodes, $J = 6\text{mA/mm}^2$). Modified from [55].

The behavior before the onset for FS is not perfectly linear (as it would be expected from Eq. 20) but the slope of curves (i.e. the activation energy for conduction) progressively rises by increasing the temperature. Different reasons can account for this:

- i. It is well-known that by changing the temperature different conduction mechanisms can be activated. In particular, at high temperature mechanisms with higher activation energy became dominant, while at low temperature are more important those with low values of Q [137–140]. For this reason, while the temperature is increasing the slope of the curves, and so the apparent activation energy, becomes larger.
- ii. The power dissipation curves are referred to the green body. So, it should not be surprising that by increasing the temperature the material will undergo to some modifications. In particular necks between particles start to be formed providing a continuous path for current flow. This should

progressively increase the conductivity of the system and so the slope of the curves in Figure 30.

The experimental data were fitted in a temperature range of 250 °C before the deviation from the linearity, as shown in Figure 30 for the sample treated with 1500 V/cm. In this way it was possible to estimate the activation energy for conduction. This has been done not only for the samples treated using platinum electrodes; but also for those treated with carbon and silver pastes for comparison. The estimated activation energies are: 1.2 ± 0.2 , 1.2 ± 0.1 , 1.0 ± 0.2 eV for Pt, C, and Ag electrodes, respectively. Two considerations deserve to be mentioned:

- i. The samples treated using Pt and C exhibit the same Q value, while the specimens treated using Ag paste are characterized by slightly lower activation energy. However, this difference is not enough for stating that different conduction mechanisms are activated, especially considering the standard deviations. In addition, as it will be shown in the following the samples connected to Ag electrodes are flash sintered at temperatures significantly lower when compared with Pt and C, so also the temperature range in which the activation energy measurement was done changes for the different electrode materials.
- ii. Despite these activation energies are referred to conduction in a green body and were measured using quite high field, the results are not far from literature data referred to bulk corundum. In particular the activation energy for conduction in dense alumina has already been estimated by Cologna et al. (1.5–2.3 eV)[39], Pan et al. (1.5–2.4 eV) [137], Mohapatra and Kroger (2.0–2.1 eV)[141] and Öjjerholm et al. (1 eV)[142]. It deserves to be underlined that this good agreement between literature and measured results is maintained even if the field used in the present work are enough high for activating non-linear effects on conductivity as it will be discussed in “4.1.4 Flash Sintering and Dielectric Breakdown”.

It is possible to observe that the activation energy for conduction is much lower than the band gap of corundum (8.7–10.8 eV)[2,143–145]. Nevertheless, the electronic

bands are bended close to the grain boundaries or surfaces because the long-range disordered structure; this could decrease the energy needed for electron promotion in the conduction band. For amorphous alumina band gap in the range 3.2 – 8.7 eV are reported in the scientific literature[143,144,146]; but they are, once again, larger than the activation energy measured in this work. A second factor that affects the band gap width is the presence of dopants. In fact, in the case of solid solution in corundum element with valence lower than 3 acts as electrons acceptor, while elements with valence higher as donors. Nevertheless, also considering different dopants band gap around 4 – 5 eV are reported in literature[144,145], still larger than the estimated activation energy. This is suggesting that, during the incubation of FS, electronic conduction is not the dominant charge transport mechanism. This is also in supported by several authors that have pointed out that the electronic conduction in corundum is activated at high temperature and becomes predominant around 1400°C[137,147–150]. Other authors suggested that conduction is mainly ionic and based on Al³⁺ diffusion even at high temperature (up to 1650 °C)[151].

Therefore, an important ionic contribution to conduction during the incubation of FS can be suggested. The problem of diffusion in corundum is quite controversial. First, a large data scattering for the activation energy of aluminum and oxygen self-diffusion can be find in literature and, second, the activation energy measured with different techniques is significantly different. Probably, the most complete overview on this argument has been done by Heuer[152]. He reported activation energy for diffusion in most the cases in the range 3- 8 eV; measuring Q using radio-tracers. However, it is to underline that these measures were carried out at high temperature (T > 1300°C) when diffusion paths at high activation energy can be activated (as a result of the high sample temperature). Moreover, it has been shown that the grain boundary presence does not reduce the value of Q [152–154]enough for making it comparable with what is calculated in this work.

Conversely, other authors attempted to measure the energy barrier for Al and O self-diffusion using electrical techniques (i.e. impedance spectroscopy, interfacial polarization) at temperatures generally lower than 1200°C. The results in this case are well-comparable with the activation energy measured in this work, fixing Q in the range 0.8 –2.4 eV[137,142,149,155]. It deserves to be mentioned that these values

are very close to the first-principle calculations for Q which lays between 0.7 and 2.5 eV [131,132,156,157]. So, we can conclude that during the incubation of FS in corundum the activation energy for conduction is comparable with the activation energy for self-diffusion of ionic species measured in a similar temperature range ($T < 1200^{\circ}\text{C}$). This suggests that during the incubation conduction is mainly ionic.

However, it is actually not clarified why so large differences of Q can be find in literature; especially comparing radio-tracer high temperature measures (3 – 8 eV) and theoretical calculations (0.7 – 2.5 eV) / electrical low temperature measures (0.8 – 2.4 eV). Different reasons can be claimed for accounting these differences:

- i. At high temperature diffusion paths with higher energy barrier are activated[137–140]; in particular a transition from extrinsic to intrinsic diffusion is observed around $1600 - 1650^{\circ}\text{C}$ [138][139]. At lower temperature diffusion is “*impurity-controlled*” or “*structure-sensitive*”[138]. In this case a central role is played by fast diffusion paths like grain boundaries or dislocations. Oishi et al. have calculated the activation energy for oxygen self-diffusion in crushed alumina and they have fixed Q in 1.87 eV, as a result of the high concentration of dislocations[158].
- ii. The large amount of surfaces in the green bodies studied in this work could lead to dominant surface diffusion mechanisms. Öjjerholm and Pan have estimated the activation energy for oxygen surface diffusion in 1 eV[142]. However, also in this case a large data scattering can be observed and many authors measured much higher value for Q[159,160]. In addition, this is not explaining why are reported so large differences in activation energy also in dense samples.
- iii. A final consideration is related to the defect chemistry of corundum. In fact, it is well-known that the points defects like interstitials or vacancies can interact each other’s[131–133,157]. The interaction is due to the electrostatic forces acting between species with opposite charges. This leads to the formation of a wide series of clusters, and each cluster is characterized by its own binding energy; Table VI summarizes the main clusters that are formed in pure corundum (intrinsic) and MgO-doped

alumina (extrinsic). Indeed, the materials are much more complex and other species can interact, since just few ppm are enough for producing defects concentration order of magnitude higher than those observed in pure corundum.

- iv. As suggested by Tewary, when one considers the activation energy for diffusion the binding energy between clusters should be taken in count[132]. For instance, an oxygen vacancies close to Mg'_{Al} would need energy for breaking the cluster and then an additional energy for overlap the energy barrier for diffusion. The measured activation energy is a result of the sum of this two terms. Thus, the measured Q should be higher than the theoretical one. The binding energy between Mg'_{Al} and V_O in Table VI are 1.36 – 2.15 eV; however, in literature also different values are reported, up to 3.5 eV.
- v. According to Tewary calculations, this should increase the activation energy for diffusion of 2 – 3 eV[132]; making comparable the theoretically calculated value of Q and those measured by radio-tracer at high temperature.
- vi. The fact that in the electrical, low temperature ($T < 1200^{\circ}\text{C}$) measurements the calculated activation energies are in good agreement with those theoretically calculated could be explained considering that, once clusters are broken, they are slowly reformed considering the low sample temperature and the fact that the vacancy motion is mainly driven by the E-field application.

The next step is now represented by the attempt to describe the electrical behavior and the power dissipation observed during the third stage of FS; therefore, after the current limit has been reached. All the following results in this section are referred to samples treated with Pt electrodes.

The power dissipation after the flash event is studied as a function of E and J in Figure 31. The first conclusion is, as expected, that current limit is the key parameter controlling the specific power dissipation during the third stage; while the effect of the electric field is less important, being the system in voltage control. The second

conclusion is that the relation between the power and J is almost linear; while a second order relation would be expected, according to Eq. 3.

Table VI: Main defect clusters formed in pure alumina and MgO-containing alumina calculated using atomistic simulation techniques. Data taken from [133].

	Cluster	Binding Energy [eV]
Intrinsic (Pure corundum)	$\{Al_i^{\cdot\cdot} : O_i''\}$	2.59
	$\{Al_i^{\cdot\cdot} : 2O_i''\}'$	4.01
	$\{V_{\bar{O}} : V_{Al}''' \}'$	3.48
	$\{2V_{\bar{O}} : V_{Al}''' \}$	7.07
	$\{2V_{\bar{O}} : 2V_{Al}''' \}'$	11.77
	$\{3V_{\bar{O}} : 2V_{Al}''' \}^x$	14.15
Extrinsic (MgO-doped corundum)	$\{2Mg'_{Al} : Mg_i^{\cdot\cdot} \}^x$	2.72
	$\{Mg'_{Al} : Mg_i^{\cdot\cdot} \}$	1.58
	$\{2Mg'_{Al} : V_{\bar{O}} \}^x$	2.15
	$\{Mg'_{Al} : V_{\bar{O}} \}$	1.36
	$\{3Mg'_{Al} : Al_i^{\cdot\cdot} \}^x$	3.59
	$\{2Mg'_{Al} : Al_i^{\cdot\cdot} \}$	3.39
	$\{Mg'_{Al} : Al_i^{\cdot\cdot} \}$	1.92
	$\{Mg_i^{\cdot\cdot} : O_i'' \}^x$	1.65

The deviation from the parabolic relation is obviously due to the fact that the sample temperature (T_s) is not always the same. The specimens treated with high current are hotter (Table IV, Figure 32) and less resistive; this leads to a decrease of $\rho_{(T_s)}$, thus the power increases slower than what suggested by the second order relation reported in Eq. 3.

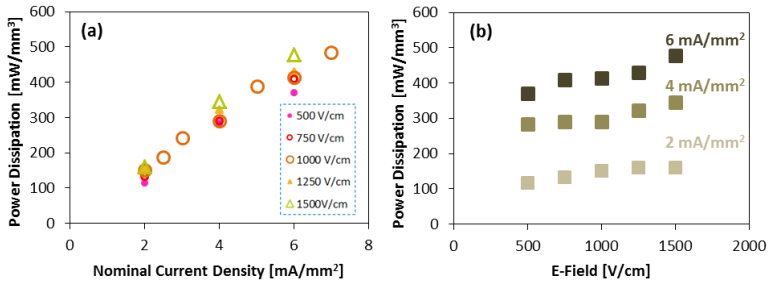


Figure 31: Specific power dissipation measured during the steady state of flash sintering as a function of the nominal current density (a) and of the E-field (b). Modified from [55].

In addition, Figure 31 shows that the specific power slightly increases with E. This is related to the fact that increasing E the onset temperature for FS is reduced, and this finally leads to a moderate reduction of the equilibrium sample temperature during the steady state of FS. The effect of J and of the furnace temperature (related to E) on the equilibrium sample temperature is qualitatively shown in Figure 32.

The relation between sample resistivity and applied current during the third stage of FS is reported in Figure 33 (a). All the data are referred to the second minute after the current limit reaching for being sure that the specimens reached the equilibrium condition. As expected, the resistivity progressively decreases by increasing the current density, this is a result of the increase in sample temperature with J. The experimental results were fitted using the minimum square method; the best fit was obtained using an emissivity equal to 0.65 and $Q = 0.94$ eV. Even changing the emissivity in a wide range, the activation energy always remains below 1 eV. In addition, the estimated value for ρ_0 is $0.0316 \Omega\text{m}$, higher than that measured during the incubation of FS ($0.0092 \Omega\text{m}$). One can notice that these values of Q are still not compatible with electronic conductivity in corundum.

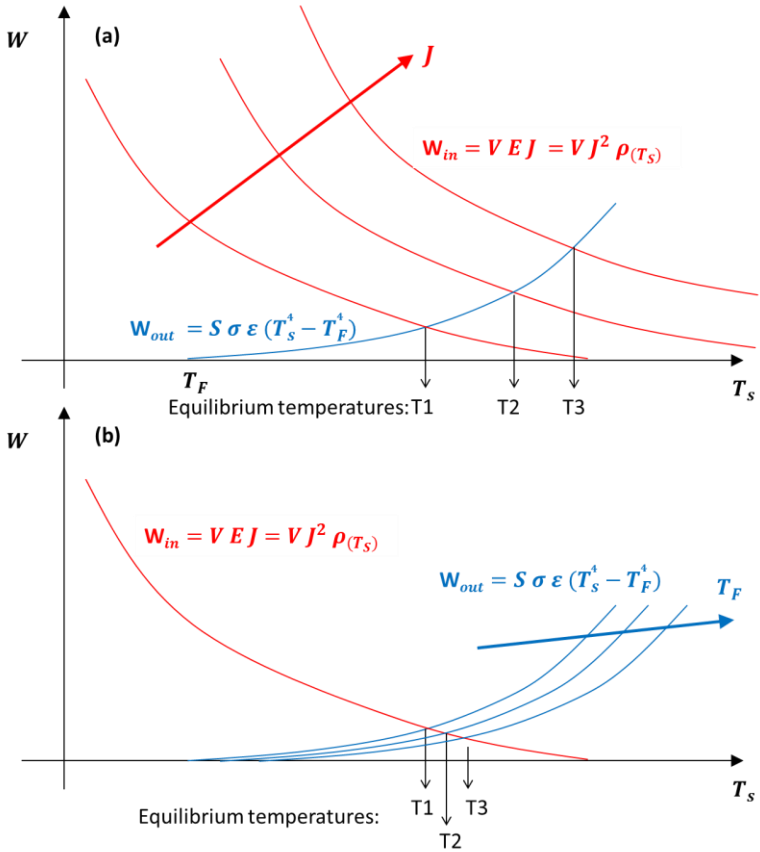


Figure 32: Current (a) and furnace temperature (b) effect on the equilibrium sample temperature during the steady state of FS. The equilibrium temperature is reached when the electrical power is equal to the heat exchanged by radiation. One should also remember that the onset for FS is depending from the field strength, resulting the specimens treated with higher E sintered at a lower furnace temperature.

However, one should also consider that a large amount of porosity is still present on the specimens treated with low current (i.e. 2 mA/mm²) while the effect of pores is practically negligible on the samples treated using higher current limits (i.e. 6 mA/mm²). In other words, while the resistivity of the samples treated with 6 mA/mm²

corresponds to a “real” values; the resistivity of the sample treated with 2 mA/mm² is overestimated, being the real cross section available for current flow reduced by the pores.

Figure 33(b) tries to answer to this problem. In this figure the resistivity are updated taking in account for the pores presence under the following assumptions:

- i. The specimen density can be approximated with the final density determined by Archimedes measurements and reported in Figure 26. This is meaning that we assume that the main part of the densification was completed in the first minute after FS;
- ii. The porosity is isotropic and homogeneously distributed.

In this case the best fit was obtained using $Q = 0.76$ eV, $\epsilon = 0.60$. It deserves also to be pointed out that we can compare this value of Q with the activation energy measured during the incubation of FS. In fact, being the porosity amount constant, as a first approximation, during the incubation of FS this is not changing the activation energy.

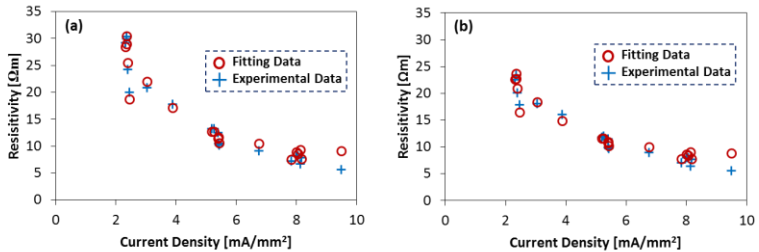


Figure 33: Resistivity calculated during the third stage of FS from electrical and geometrical parameters without (a) and with taking in account of the effect of porosity (b). The best interpolation was given using: $Q = 0.94$ eV, $\epsilon = 0.65$ (a) and $Q = 0.76$ eV, $\epsilon = 0.60$ (b). Modified from [55].

The conclusion is that the activation energy during flash sintering is reduced; thus, changes in the conduction mechanisms can be suggested. Nevertheless, it is quite surprising that Q decreases: since sample temperature increases during FS one should expect that conduction mechanisms with higher energy barrier would be activated.

Some reasons can be advanced for explaining the behavior:

- i. A liquid film formation at the grain boundaries could provide a fast diffusion path for ionic diffusion and changes the band gap for electron promotion. However, if we look at literature data the activation energy for conduction in molten alumina was estimated to be: 1.4 eV[161]. This value is still larger than what have been measured in this work.
- ii. One can also suggest that the samples treated with low currents are less resistive than what it would be expected because of the formation of an air plasma at neck between particles. However, this statement do not find any evidence form the photoemission measures reported in the next section and in literature[18,20].
- iii. The presence of electrolytic reaction close to the electrodes leads to a partial reduction of the material. This could change the electrical properties and the activation energy value, leading to a mixed conduction behavior.

Previous works on partially-reduced zirconia have pointed out that this material is much more conductive and characterized by lower activation energy for conduction when compared with the stoichiometric oxide[43]. Also the dielectric properties, like dielectric constant and loss factor, have been shown to be are sensitive to the oxide stoichiometry[45].

Additionally, it is significant to point out that a decrease of Q during FS has already been reported also on YSZ (AC)[65] and titania (DC)[107]. Conversely, Du et al. always working in AC, have observed much more conventional conduction behavior in the flash state.

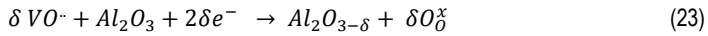
An important effect of electrolytic reactions on FS was proposed for the first time by Downs for explaining the flash sintering in cubic zirconia[9]. Similarly to what suggested by Downs for zirconia we can identify an electrolytic reaction at the anode:



and at the cathode:



Thus, the anode acts as an oxygen vacancies source, the vacancies moves under the E-field effect toward the cathode and here are consumed by the opposite reaction. However, when the current reaches a certain value at the cathodic site the reaction, which involves molecular oxygen decomposition, could be not enough fast for balancing the charge carriers motion. In addition, sintering progressively reduce the surface at which the reaction can take place decreasing its rate. Hence, the crystal itself becomes a source of oxygen and a partial reduction of corundum take place:



By combining Eq. 21 and 23 the reduction equation for alumina can be obtained:



The partial reduction of the oxide enhances electrical conductivity and is responsible for the change in the activation energy for conduction. Being the material partially reduced the conduction turns from mainly ionic to electronic. Indeed, reaction 23 needs electrons for being completed; thus, it has been reported to start at the cathode in YSZ[42]. Then, the reaction front progressively moves toward the anode as the partially reduced areas allows electrons motion within the sample. The behavior, as we will show in alumina, is a bit different.

The high vacancies concentration produced via electrolyte reaction and partial reduction of the cations could provide an explanation for the observed densification and electrical behavior. All these conjectures are mainly speculative; nevertheless, some evidences are compatible with these assumptions. These evidences are described in the following and involves:

- i. Photoluminescence spectroscopy;
- ii. Temperature asymmetry during the process;

- iii. Blackened area formation;
- iv. XPS analysis.

The photoluminescence spectra obtained using an excitation wavelength of 300 nm on samples treated using experimental set up 2 and different current limits are reported in Figure 34. The four specimens show extremely different behaviors. In particular, one can observe the formation of a wide band on flash sintered samples with a maximum around 410 nm. This band was not detected in the specimen treated with 2 mA/mm² and in the conventionally sintered body. One can also notice that the band becomes progressively stronger by increasing the applied current during the sintering process.

Photoluminescence in corundum has been extensively studied by many authors and finds solid basis in the scientific literature. As it has been reported by Kouroukla[162] and other authors[163,164] the structural defects in corundum F and F⁺-centers should emit light with a maximum intensity in the range 410- 420 and 330-340 nm, respectively. The F-centers are oxygen vacancies filled with two electrons, while the F⁺ ones are filled with just one electron and so have a positive charge. Also F_{cations} – centers can be observed in alumina with an emission range around 300 nm. These are the result of the electrostatic interaction between oxygen vacancies and divalent ions (e.g. Ca²⁺, Mg²⁺) which leads to the formation of well-known defect clusters[133]. Therefore, the literature data are suggesting the conclusion that the wide band observed in the flash sintered sample is related to lattice defects which can be identified as F-centers. No significant signal was recorded in the F⁺ emission range: 330-340 nm. However, this may be due to the fact that this kind of centers should be activated using higher radiation energy. In any case, the experimental results suggest, at least by a qualitative point of view, that the oxygen vacancies concentration is increasing in the sintered sample by increasing the current used during the treatment. This is providing evidence that the material is changing its structural features during flash sintering.

The formation of charged oxygen vacancies is guarantee by Eq. 21. and their reduction to the uncharged form by reaction Eq.23; allowing the formation of F-

centers. Therefore, these results are compatible with a partial reduction of corundum during flash sintering.

It should be remarked that the strong correspondence between current limit and photoluminescence spectra suggest that the material reduction is a phenomenon mainly related to the third stage of flash sintering. This is not particularly strange considering that during flash sintering incubation the current is quite low and the high porosity of the material allows oxygen restoration in the crystal through the cathodic reaction (Eq. 22).

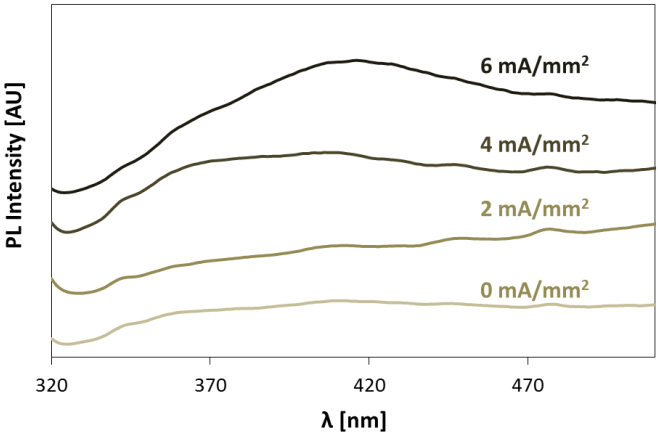


Figure 34: Photoluminescence spectroscopy of alumina samples treated with different current density.

A second consideration supporting the thesis of partial reduction of alumina during the process is represented by the observation of the sample during the FS treatment, allowed by the experimental set up n.2. In Figure 35 are reported pictures of a specimen at different times during the three stages of flash sintering. The sample was pre-sintered at 1250°C and treated using 6 mA/mm² at a furnace temperature of 1200°C.

Figure 35 shows that the light emission is slightly asymmetric. In fact, the anode (+) is brighter with respect to the cathode (-). The photoemission is mainly an effect of Joule heating, as it will be shown in section "4.1.3 Photoemission during Flash Sintering", hence the result is suggesting that the anodic area is hotter.

Temperature differences between anode and cathode are, in addition, confirmed by shrinkage measurements carried out in a direction perpendicular to current flow, on a section passing through the center of the hole in which the electrodes were inserted, as it is shown in Figure 36. The results indicate that the shrinkage obtained during FS in the anodic area is always higher when compared with the cathodic one; so, the anode should be hotter. This is in agreement with the asymmetry observed in the light emission.

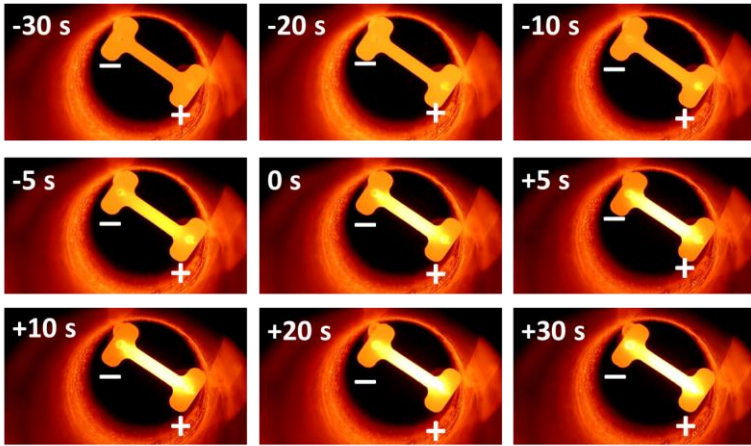


Figure 35: Pictures of a sample subjected to flash sintering at different times ($t = 0$ s was assumed to correspond to the system reaching the current limit).

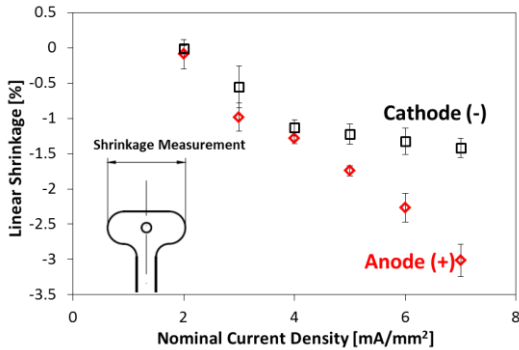


Figure 36: Linear shrinkage achieved in the electrode area (experimental set up 2, pre-sintering temperature = 1250 °C, $E = 750$ V/cm).

This temperature asymmetry can be explained as a result of different power dissipation within the specimen. In other words, the resistivity close to the cathode and to the anode are different, being the latter higher. This results in an higher anodic specific power dissipation since the current should be the same on each crosssection.

The reasons behind this phenomenon could be the different electrodes reactions Eq.21-23 during the incubation of FS. While the anodic reaction creates new defects within the ceramic the cathodic one represent a symple rearrangement of the defect structure and it is reasonably more spontaneous. Therefore, the driving force (the E-field) should be higher at the anode thus resulting in a higher power dissipation. In addition the field-induced $VO^{\cdot-}$ migration toward the cathode (-) increases the charge carrier population on this side reducing the local resistivity.

The third reason for supporting the thesis of partial reduction of the material during flash sintering is represented by the formation of the well-kown blackened zones. The formation of the blackened area can be observed only in DC and characterizes the samples treated for long times with high currents.

The first publicated description of these areas in a paper focused onFS was given by Muccillo[47] stating that:

“Numerous experimental results, obtained for instance with fuel cells, show that an efficient compensation (of vacancies motion) cannot be expected for current densities exceeding a few A/cm². When the compensation is not ensured, the sample is chemically reduced. This results in an additional, fairly high, electronic conductivity. This is the so-called blackening process. Experimentally, when this process starts locally, it initiates preferential current routes because of the important local electric resistance fall.”

This phenomenon takes place also in alumina and was observed in this work. The extension of the blackened areas depends from the current density, becomming visible with current higher than 5 mA/mm². The blakening-process affected only limited volumes and it is pretty concentrated on some current concentration paths.

Table VII shows the O/Al molar ratio calculated via XPS on a conventionally sintered and flash sintered specimen (exp. set-up n.2, 6 mA/mm², 4 min).The flash sintered sample was analysed both in the black and white zone. The results are only semi-

quantitative; they are reported with the only objective to compare their relative values. We can notice that the O/Al ratio is different from that theoretically expected (1.5); nevertheless, this is not particularly surprising since the oxygen atoms close to the surface are chemically bonded to other chemical species (like hydrogen, forming surface OH groups). Additionally, we want to reaffirm that the measure is not strictly quantitative.

The key point that should be underlined is that the O/Al ratio is higher in the case of the conventionally sintered specimen; whereas the flash sintered sample presents oxygen deficient structures. Additionally, within the flash sintered specimen it is possible to notice that the black areas presents lower oxygen content when compared with the white ones. This experimental finding is supporting the thesis that a partial reduction of the oxide takes place during FS and the blackened zones are composed by a more reduced material.

In alumina, blackening generally starts from the anode and progressively moves towards the cathode. This is somehow surprising considering that the $VO^{\cdot\cdot}$ migration should produce more reduced structures on the cathodic side. It becomes still more surprising when compared with what has been reported by Downs for YSZ[9]; being in his case the cathode more blackened.

Table VII: Molar ratio between O and Al measured by XPS on conventional sintered and flash sintered specimen.

Sample	O/Al
Conventional Sintered	2.00
Flash sintered: White	1.88
Flash Isntered: Black	1.75

The answer to these apparent contradictions can be find considering the different nature of conduction in cubic zirconia and alumina. Zirconia is a good ionic conductor; therefore, the mobility of oxygen vacancies is pretty high. This means that once a $VO^{\cdot\cdot}$ is formed close the anode (reaction in Eq. 21) it moves quite faster and it has good chances to reach the cathodic area before meeting electrons and being

reduced. This results in a quite homogenous blackening process, slightly more marked close the cathode.

Conversely, the oxygen vacancies mobility in alumina is much lower. Thus, during the third stage of FS we assumed that the conduction mechanism is mainly electronic, allowed by the described partial reduction of the material. Nevertheless, even if it should be quite slow the anodic reaction (Eq. 21) producing oxygen vacancies continues during the third stage of flash sintering. These $VO^{\cdot\cdot}$ moves much slower than in YSZ; thus, they are reduced where they are produced: at the anode. Therefore, the accumulation of vacancies at the anode during the third stage of FS leads to the formation of these heavily-reduced zones, which results black. If the treating time is prolonged electrons starts to be removed also at the interface between the blackened and white alumina, in this way the anodic reaction site moves progressively allowing an expansion of the blackening process.

A second consideration regarding the differences between YSZ and alumina deserves to be done. The defect population before the flash in the two material is completely different; being zirconia doped with 3-8 wt% of yttria the oxygen vacancy concentration is several order of magnitude higher than that in alumina. Hence, the number of vacancy formed at the anode during FS of YSZ is relatively less "important" than in alumina. This could contribute to the fact that the blackening in corundum starts from the anodic site, while in YSZ the blackening is mainly a result of a partial motion toward the cathode of the defects already present in the material before the treatment.

In order to highlight the characteristic of these dark areas a sample was treated with experimental set up n.2 under very severe conditions of J and time (7 mA/mm² for ~ 4 min); the experiment was interrupted because of sparking. A picture of this sample is reported in Figure 37. The blackened areas are quite extended, although they could be observed only on the side of the sample represented in Figure 37. Therefore, also in this case, only a minor part of the specimen was affected by the blackening process. As previously mentioned, the blackening starts from the anode and moves toward the cathode.

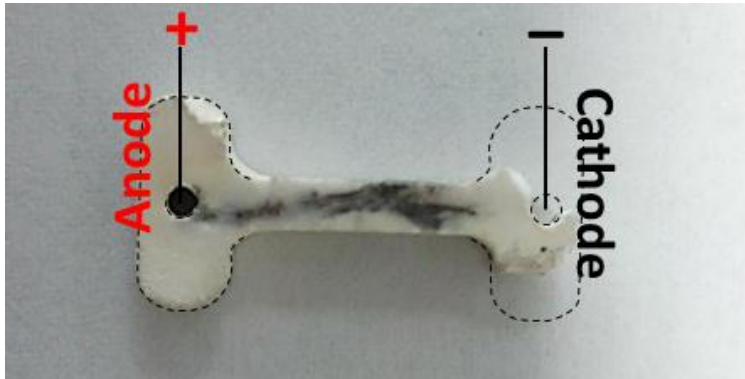


Figure 37: Blackened areas on a sample treated with 7 mA/mm^2 for ~ 4 minutes (experimental set up 2).

Some SEM micrographs were obtained on this sample and are reported in Figure 38, Figure 39 and Figure 40. It is nice to observe that the micrographs are showing the presence of typical solidification structures, indicating that the material was locally melted during the process.

Different microstructure can be observed in the blackened alumina. The first structure is represented by the grain coalescence zone (Figure 38 and Figure 39(b)). This area was blackened and not melted during FS, but it reached temperatures very closed to the melting point. This results in an abnormal grain growth and grains of several hundreds of micron can be observed. On the material surface it is possible to notice the presence of some lines (Figure 39(b)). These could be a result of the combined effect of high temperature and thermally-induced stresses. The combined effect of high temperature and stress produces shear bands along preferential crystallographic orientation, leading to viscous flows within the grains.

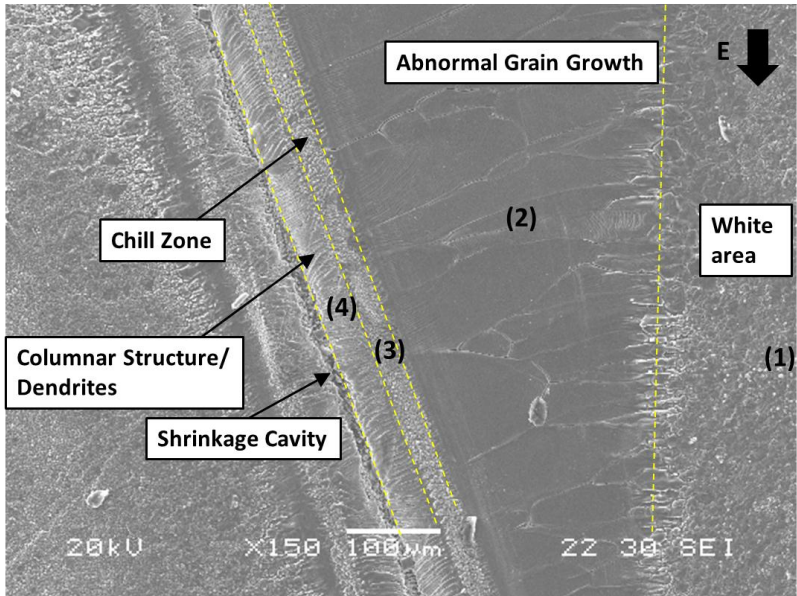


Figure 38: SEM micrograph of the blackened areas obtained on a sample treated with 7 mA/mm² for ~ 4 minutes (experimental set up 2). The micrograph was taken in the central part of the gage section. The field direction is indicated by the black arrow; the different microstructural areas are indicated and numbered.

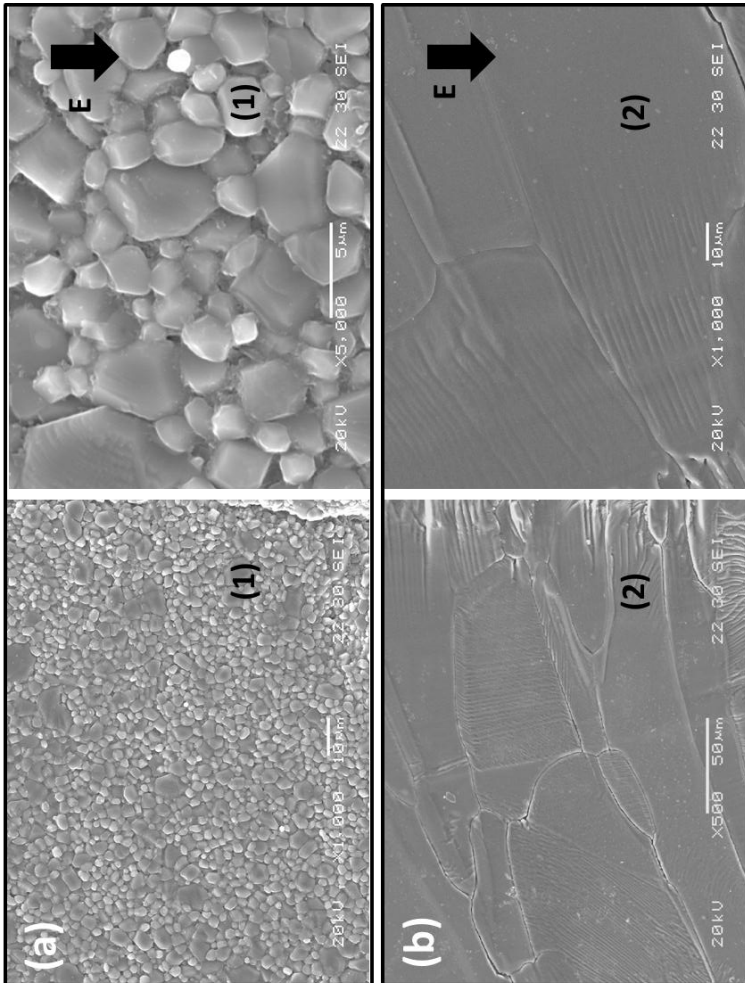


Figure 39: SEM micrographs of the non-melted zone obtained on the sample treated using 7 mA/mm for ~ 4 minutes. One can point out normal grain growth in the white areas (a) and abnormal grain growth on the blackened ones (b). The field direction is indicated by the black arrow; the numbers between brackets allows to identify the position of the different microstructures in Figure 38.

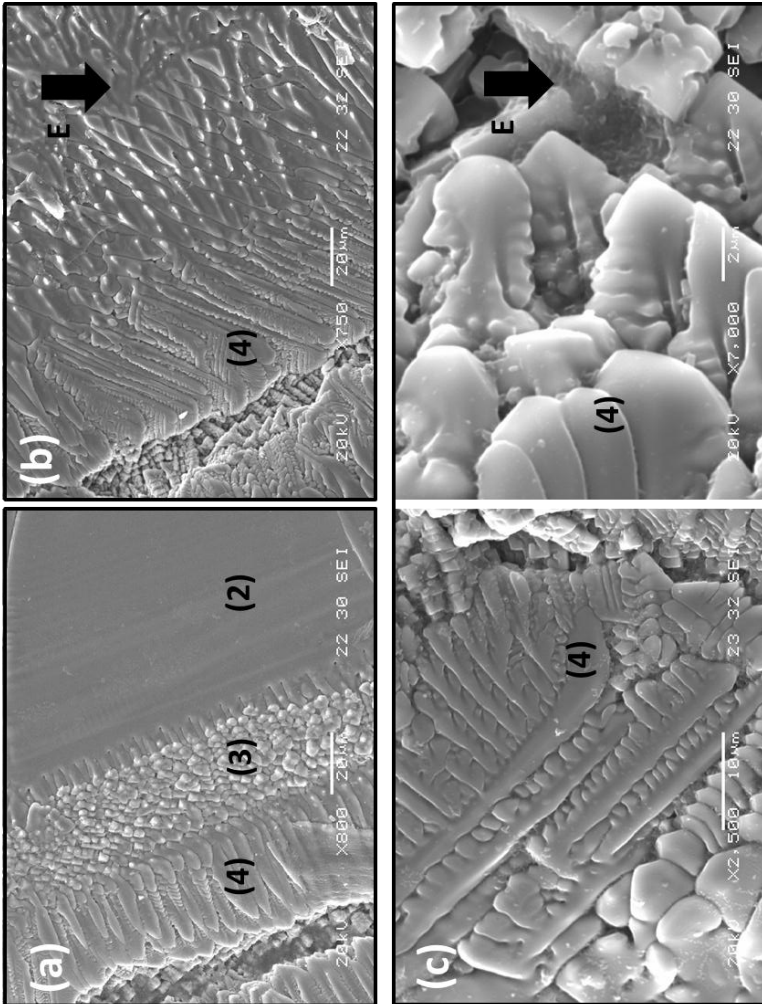


Figure 40: SEM micrographs of the solidification structures obtained on the sample treated using 7 mA/mm for ~ 4 minutes. The chill zone/dendrites (a) and columnar/dendrites (b) transition can be observed; some typical dendrite structures are also reported (c). The field direction is indicated by the black arrow; the numbers between brackets allows to identify the position of the different microstructures in Figure 38.

The differences in terms of grain size between the blackened and the white areas are pointed out in Figure 39. We can state that the grain size in the blackened zone is at least 2 orders of magnitude larger than in the white ones. It is also nice to observe that the transition between the two zones is very sharp (Figure 38) and a complete transition from abnormal to normal grain growth takes place in few tens of microns. An extremely high and quite unreasonable thermal gradient would be required for explaining this behavior. In addition, using Eq. 18 we can notice that grains of 100 μm can be obtained, conventionally, in 4 minutes at a temperature $\sim 2700^\circ\text{C}$; this result is absolutely unreasonable and much higher than the melting point of alumina. A second consideration is that the grains are equiaxial in the white areas, while they preferentially grow in a direction orthogonal to the melted zone (at the center of the blackening) in the blackened ones, thus resulting in a quite elongated grain shape (Figure 38 and Figure 39(b)).

It deserves to be pointed out that the results resemble those reported by Kim et al. [49] and Qin et al. for YSZ [48]. Qin and co-workers observed abnormal grain growth close to the cathode and they estimated that such a grain size would be obtained conventionally at $\sim 4100\text{ K}$ (temperature much higher than the melting point of YSZ). They argued that the partial reduction of the material close to the cathode, as a result of the VO^\bullet motion and electron injection, lowers the activation energy for grain boundary migration. It is important to observe that in YSZ the blackened areas were concentrated mainly at the cathode, exactly where abnormal grain growth has been observed. Hence, probably, in alumina something similar is happening; but it starts from the opposite side, being the blackened zone first formed in proximity of the anode.

The reasons behind the anisotropic grain growth, with grains preferentially oriented in a direction orthogonal to the melted area and to the current flow are not completely clarified. Nevertheless, we can propose three possible mechanisms. The first mechanism should take place at the interface between the blackened (heavily reduced) and the white slightly reduced areas (Figure 41 (a)). One can imagine that first the melted path connecting the two electrodes is formed; then, the blackened zone growth starts from the melted path. Since electrons are thought to move very quickly in the blackened zone, when a charged oxygen vacancy gets close to the

boundary between the blackened ($Al_2O_{3-\delta}$) and the white zone (Al_2O_3) it is suddenly reduced according to reaction in Eq.23. This leads to the oriented growth of the reduced phase and to abnormal grain growth. The second proposed mechanism happens within the blackened zone (Figure 41 (b)). It is based on the assumption that the degree of reduction of the material increases moving toward the center of the blackened zone (represented by the melted area) and the oxygen vacancies in the blackened zone are discharged by the reaction with electrons. This leads to a different oxygen vacancies concentration on the opposite side of a GB, being the vacancies concentration higher on the side closer to the melted zone. This difference in vacancies concentration becomes the driving force for grain boundary motion rather than curvatures. In this way VO should cross the GB moving away from the melt, while O atoms moves toward the melt.

The third mechanism that could explain the oriented grain growth is based on the assumption that a strong temperature gradient is formed between the melted zone and the other parts of the specimen (Figure 42). In this condition the grain boundary energy would depend from the distance from the melt (x). Differentiating the expression for grain boundary energy (Eq. 4) we can obtain:

$$\delta\gamma_{gb} = \frac{d\gamma_{gb}}{dx} \delta x = -\frac{dT}{dx} \Delta S_{gb} \delta x \quad (25)$$

where $\delta\gamma_{gb}$ is the grain boundary interfacial energy variation resulting from grain boundary motion across a distance δx (x axe defined in Figure 42). Referring to the data in Figure 42, being $\Delta S_{gb} > 0$ and the derivative of $T < 0$ a decrease of the grain boundary energy ($\delta\gamma_{gb} < 0$) can be obtained assuming a grain boundary migration toward the melt ($\delta x < 0$). This additional driving force could enhance the grain growth only in the direction orthogonal to the melt path (where significant temperature gradient occurs) and could explain grain orientation; nevertheless, it can not explain why the grains are so large also in the other directions. Therefore, a contribution due to material reduction can be in any case pointed out.

At the center of the blackened zone other structures can be observed in the areas that were melted during FS:

- i. **Chill Zone:** this area is characterized by equiaxial grains and is placed at the limit of the melted area (Figure 40 (a)). This is the first zone that is solidified during the cooling process.
- ii. **Columnar/Dendritic structures:** these are characterized by elongated grains and by the presence of many arms (Figure 40 (b), (c)).
- iii. **Shrinkage cavity:** is at the center of the melted area and is a result of the constrained solidification process, which leads to the formation of a cavity.

All these microstructures clearly prove that local melting occurs. Nevertheless, it is very difficult to state that the local temperature reaches values higher than 2072°C, which is the melting point for corundum. In fact, this value is much higher than what previously calculated and reported in Table IV and the electrodes never melted in all the experiments, although they were forced inside the holes in the sample. The melting temperature of Pt is 1768 °C, ~ 300°C lower than the melting point of alumina. Even more difficult is to explain the abnormal grain growth in the blackened zone that would require temperatures higher than 2700°C. Hence, we believe that the structural changes in the oxide induced by severe current flow and the formation of out-of-equilibrium structures are at the base of such phenomena. They can interact with the diffusion process kinetics.

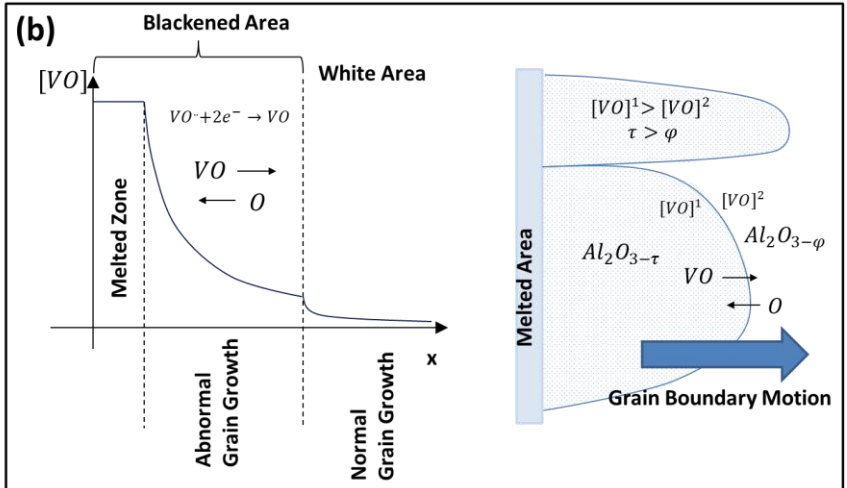
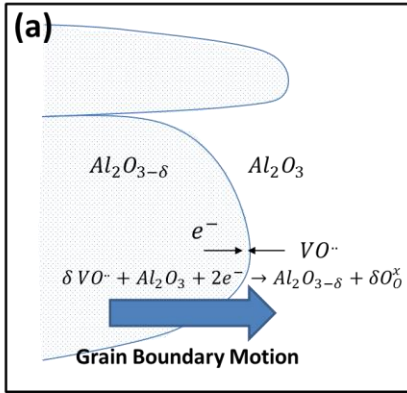


Figure 41: Possible mechanisms at the base of abnormal/anisotropic grain growth at the interface between blackened and white areas (a) and within the blackened one (b). The mechanism (a) is based on the assumption that the abnormal grain growth is associated to the growth of the substoichiometric phase. The mechanism (b) assumes the presence of a discharged vacancy gradient in the blackened areas which accelerate the mass flux.

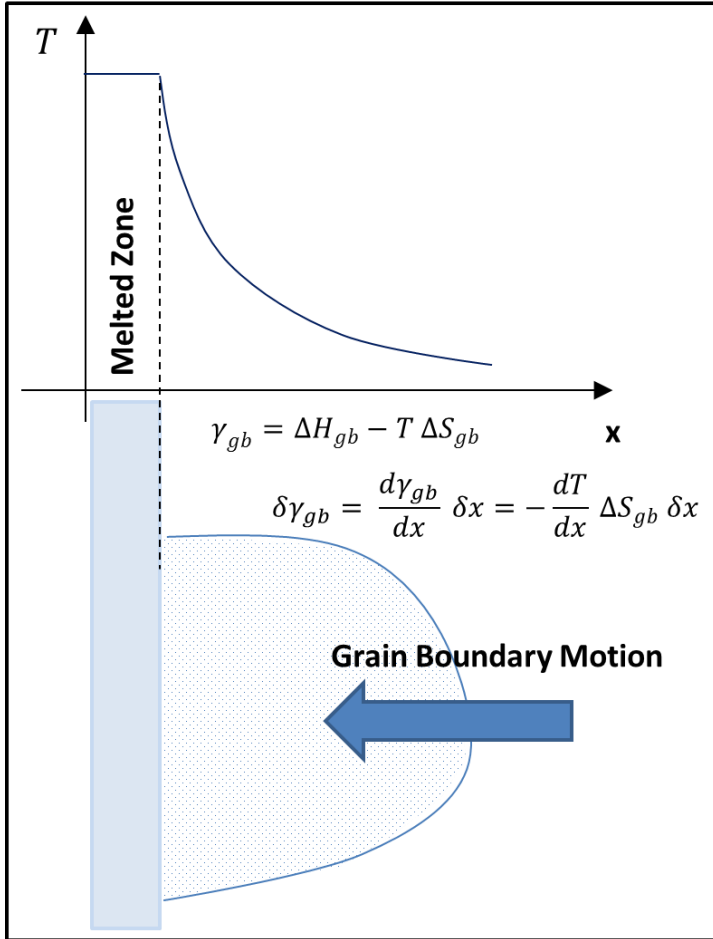


Figure 42: Mechanism for oriented grain growth in the blackened areas based on a thermal gradient. The grain boundary would migrate toward the hotter region (melted zone) as a result of a net decrease in the grain boundary energy ($\delta\gamma_{gb}$).

The results summarized in this chapter point out that the current flow allows a partial reduction even of a high stoichiometric oxide like alumina. This partial reduction changes the mass and charge transport phenomena in the oxide.

All the considerations and experimental results reported here suggest that FS can not be interpreted only using “conventional” sintering theories; some field/current induced mechanisms must be considered; among them, a partial reduction of the oxide seems the most attractive. Strong experimental evidences are reported supporting the thesis that a current-induced partial reduction takes place even in a high stoichiometric oxide like alumina.

4.1.3 Photoemission during Flash Sintering

The light emission during flash sintering was studied using the experimental set up n. 2. The samples were pre-sintered at 1250 and 1450°C; the furnace temperature during FS experiments was fixed at 1200°C.

The photoemission during the third stage of FS is reported in Figure 43 (a) for a sample pre-sintered at 1250°C and treated with different current densities. The first conclusion is that the shape of the spectra does not change with the applied current, suggesting that no additional phenomena are activated increasing the current limit.

The second result is that the spectra are pretty similar to those recorded by Lebrun [18] and Naik [20] on different materials (YSZ, SrTiO₃, K₂NbO₃): all spectra present a shoulder around 620 nm and two maxima around 720 and 760 nm. Therefore, it seems that the light emission in the UV/VIS region is independent from the tested material. This is in contrast with the theories that explain the photoemission during FS as a result of electroluminescence; in fact, electroluminescence should depend on the electronic structure of each tested material.

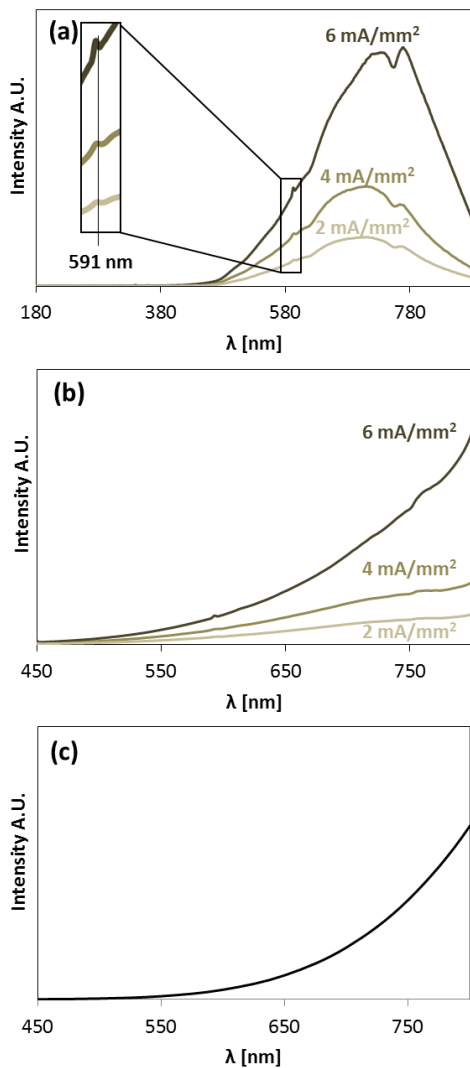


Figure 43: Photoemission spectra collected during the steady stage of flash sintering using different current density (samples pre-sintered at 1250°C). In particular are reported both the spectra as collected (a) and after the calibration with halogen lamp (b). For comparison the black body spectrum, calculated at 1600 K, is also reported (c).

In order to take in account of the effects due to the experimental set-up, the quantum yield of the spectrometer and the transmittance of the optical fiber a calibration was operated using an halogen lamp. Knowing the ratio between the real light intensity (emitted from the lamp) and the measured one it was possible to calculate a correction factor for each value of wavelength. The corrected spectra are reported in Figure 43 (b). The shape in this case is much more familiar and similar to the Black Body Radiation (BBR), being the maximum of the thermal radiation in the IR region. For comparison, the photoemission calculated for a black body at 1600 K from Planck's law is reported in Figure 43 (c) [94]:

$$I_{(T,v)}^{BBR} = \frac{2\pi h v^5}{c^3} \frac{1}{\exp(hv/kT)-1} \quad (26)$$

where v is the radiation frequency, c the light speed, T the absolute temperature, h and k Planck's and Boltzmann constant, respectively. The figure points out that the light emission spectra of the samples during the third stage of FS are very similar to what expected from Planck's law. The main difference is represented by a small shoulder around 760 nm (Figure 43 (b)). Nevertheless, this can probably be accounted for by some residual experimental effects, presenting the calibration curve (not reported) a peak in that position.

The light emission during the different stages for FS is reported in Figure 44 for a sample treated using 750 V/cm and pre-sintered at 1450°C ($J = 4 \text{ mA/mm}^2$). The results point out that:

- i. The light emission progressively increases during the incubation of flash sintering and still increases after the power dissipation peak which corresponds to the current limit reaching. This is compatible with an emission due to Joule heating. In fact, during the process the sample temperature progressively increases as a result of the thermal runaway. Nevertheless, the specimens temperature still increases in the third stage of FS being the electric power higher than heat exchanged by radiation until the equilibrium temperature is reached (as qualitatively shown in Figure 10). Hence, the time-dependent light emission evolution is compatible with a thermal radiation.

- ii. The light emission shape is not changing during the different stages of FS, suggesting that no luminescent effect are activated before, during and after the current limit reaching.
- iii. The light emission shape do not depend from the relative density of the body subjected to flash sintering.

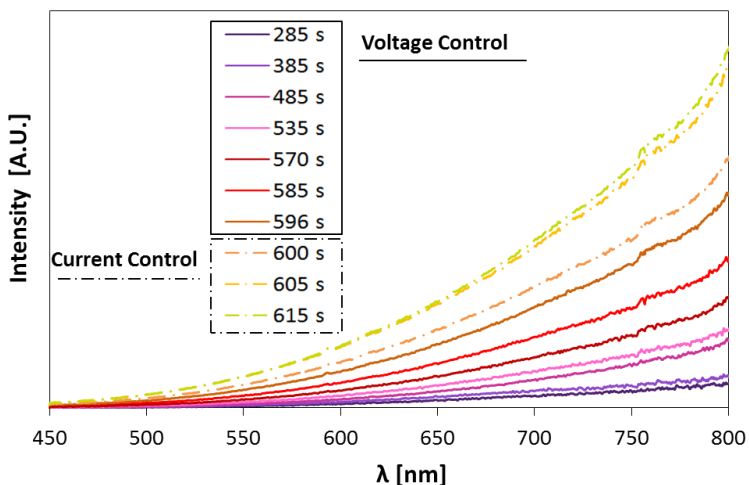


Figure 44: UV/VIS photoemission spectra obtained during the different stages of FS.

Therefore, the results indicate that the light emission in the UV/VIS range is just a result of the thermal radiation due to Joule heating. There are, no indications suggesting the presence of electroluminescence or, if electroluminescence is present, its intensity is negligible with respect to thermal radiation.

Nevertheless, the results presented so far provides just qualitative common points between photoemission during FS and BBR. In order to highlight more quantitative affinities, the light emission intensity evolution for three different wavelength during the incubation of FS is reported in Figure 45 (a) and it is compared with the measured conductivity. The photoemission was normalized with respect to the intensity measured during the steady stage of FS. One can notice that the three

intensities are extremely “coupled” and they behave in a very similar way. If the light emission was a result of electroluminescence some intensities would growth more than others during the process, but this was not observed.

Figure 45 (b) shows the decay of the normalized photoemission intensity after that the power supply was switched off. Also in this case the decay of the intensity at different wavelength is coupled and the light emission requires several seconds for being reduced. Once again this result is compatible with the BBR; in fact, the specimens would require several second for being cooled as a result of its own thermal capacity. Conversely, electroluminescence would decay much faster.

It is also possible to observe that the light intensity emitted at low λ (i.e. 530 nm) is slightly lower than those at higher λ (i.e. 850 nm) during the runaway for FS and the decay of the photoemission. In other word, the light emitted at 530 nm is relatively stronger, when compared with 700-850 nm, during the third stage of flash sintering (when the sample is hotter) and weaker during the other stages (when the sample is colder). This is a result of the fact that increasing the sample temperature the maximum of the photoemission moves toward lower wavelength, according to Wien's displacement law [94]. Thus, increasing the temperature the light emission intensities at lower wavelength growth more, in proportion, respect to those at higher λ .

Figure 45 (a) points out also that photoemission and electrical conductivity behaves in a similar way. This is not surprising; in fact, if the light emission is due to a thermal radiation, both conductivity and light emission intensity are related to the sample temperature. In order to explore this relation we can write the intensity of light emitted by an incandescent body as:

$$I_{(T,v)}^{REAL} = \varepsilon_{(v)} I_{(T,v)}^{BBR} = \varepsilon_{(v)} \frac{2\pi h v^5}{c^3} \frac{1}{\exp(hv/kT)-1} \quad (27)$$

where $\varepsilon_{(v)}$ is the spectral emissivity depending from the wavelength. The relation for the electrical conductivity in a ceramic insulator can be written as:

$$\sigma_{(T)} = \sigma_0 \exp(-Q/kT) \quad (28)$$

where σ_0 is a pre exponential constant and Q the activation energy for conduction.

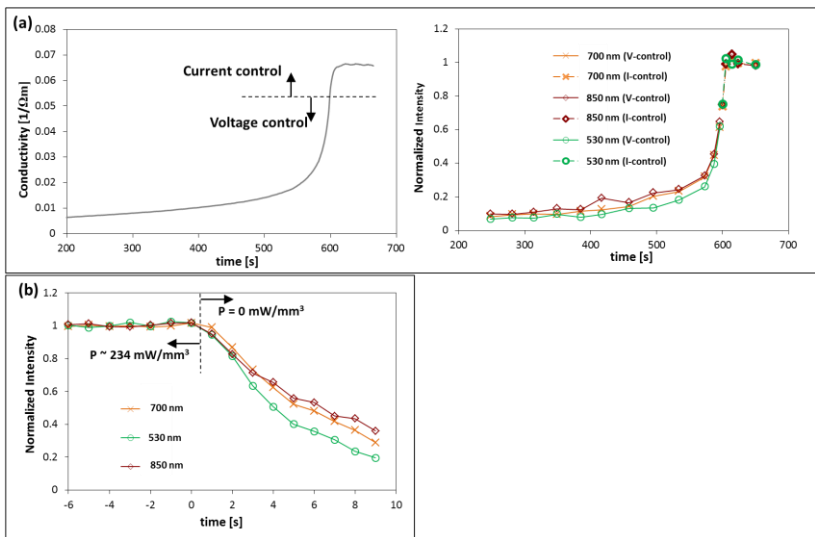


Figure 45: Normalized light emission evolution at different wavelengths during the incubation (a) of FS and after the power supply was switched off (b). It is also reported the conductivity evolution which can be well compared with light emission.

Here, we assume that the sample temperature can be considered homogeneous during the process. This is an approximation: Figure 35 pointed out a certain temperature asymmetry between the two electrodes. However, this asymmetry involves only a small part of the specimen; therefore, the assumption seems to be reasonable. Joining Eq. 27 and Eq. 28 it is possible to write a relation between light emission and conductivity:

$$I_{(\sigma,v)}^{REAL} = \mathcal{E}(v) \frac{2h\pi v^5}{c^3} \frac{\sigma^{hv/Q}}{\sigma_0^{hv/Q} (1 - (\sigma/\sigma_0)^{hv/Q})} \quad (29)$$

Indeed, being σ_0 the conductivity of the material at a virtually infinite temperature, the ratio between σ and σ_0 is negligible. E.g. even assuming an activation energy for conduction of 1.2 eV (the same previously measured) and a temperature of 2000 K (higher than the temperatures in Table IV) it is possible to estimate: $\sigma/\sigma_0 \sim 0.001$. Therefore Eq.29 can be reduced to:

$$I_{(\sigma,\nu)}^{\text{REAL}} = C_{(\nu)} \sigma^{h\nu/Q} \quad (30)$$

where $C_{(\nu)}$ is a function of the radiation frequency. According to Eq. 30 the relation between light emission intensity and conductivity should be a power law with the exponent depending from the wavelength/frequency of the radiation. In particular, if a radiation with high wavelength (low ν) is considered the exponent decreases; conversely if the wavelength is low (high ν) the exponent increases.

Using Eq. 30, the experimental results recorded on the sample pre-sintered at 1450°C and treated with 750 V/cm – 4 mA/mm², were interpolated by the minimum squares method. In Figure 46 are reported both the experimental data and the fitting curves (black dashes lines), showing that Eq.30 provides a pretty good approximation of what is going on during the process. A small deviation from the predicted behavior can be observed during the third stage of FS, being the light emission slightly underestimated. This can be related to the fact that the walls of the tubular furnace are quite close to the specimen (being the inner diameter of the alumina tube 30 mm), thus they are heated during the process. In this way the furnace itself should start to emit more light than what was estimated at the beginning of the treatment.

As theoretically expected the power law exponent in Figure 46 depends from the chosen wavelength and it decreases by increasing λ . From the value of the exponent (n) it is also possible to estimate the activation energy for conduction, being:

$$Q = h\nu/n \quad (31)$$

The results suggest that Q ranges between 1.5 and 1.8 eV. These values are similar to literature data for corundum and not far from what previously measured on the green specimens (1.2 eV). The differences between the activation energy measured here and on the green specimen can be related to the different microstructural feature of the material (partially sintered/green body) and to the temperature range in which it was measured ($T > 1200^\circ\text{C}$ for photoemission and $T < 1200^\circ\text{C}$ for the green bodies).

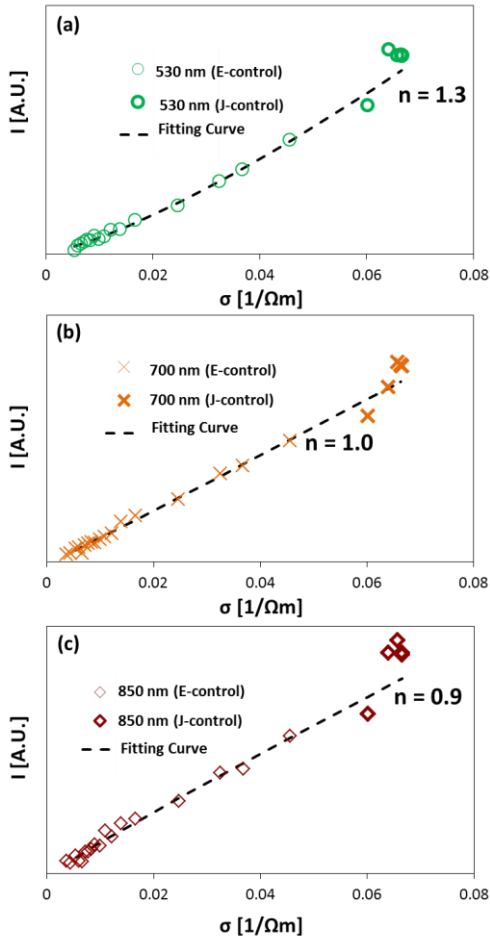


Figure 46: Light emission intensity as a function of the measured conductivity at different wavelength: 530 (a), 700 (b), 850 nm (c). The value of n , the exponent of the fitting power law, is also reported.

Since Terauds and co-workers have observed two photoemission peaks in the NIR during FS of YSZ[17], we analyzed also for alumina the light emission in this region. The spectra are reported in Figure 47(a) and they point out that the NIR photoemission is independent, in its shape, from the applied current. For comparison, the spectrum emitted by the hot alumina tube of the furnace at 1400°C

is reported in Figure 47(b). One can observe that the two spectra present the same features and the same shape. Hence, we can conclude that also in the NIR region there are no reasons for claiming luminescent effect during flash sintering of corundum.

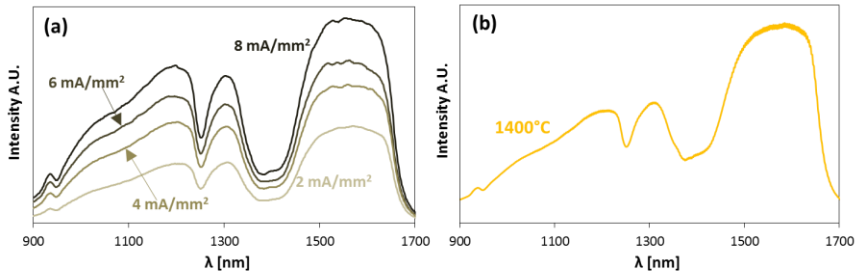


Figure 47: NIR spectra obtained during FS using different current density (furnace temperature= 1200°C) (a) and the thermal radiation of the furnace heated at 1400°C(b).

Some final consideration deserve to be drawn:

- i. It is possible to observe a small peak at 591 nm (Figure 43 (a)). Nevertheless, it completely disappears if the electrodes were shielded. This suggests that the peak could be related to some spark/air ionization at the metal/ceramic interface. In addition, its position could be associated to a line of ionized nitrogen[165]. No evidences of air ionization are observed in places different from the electrodes (i.e. inter-particle regions, pores...).
- ii. It is possible to notice in Figure 43 that no relevant signal was measured at 188 and 255 nm. These wavelength should be associated with the annihilation of the Frenkel pairs for aluminum and oxygen, respectively[133]. The formation and the consequent annihilation of Frenkel pairs has often be claimed for explaining the densification during FS. Even if a definitive conclusion can not be drawn the measurements here reported do not offer any support to this thesis.

The results reported in this chapter points out that the photoemission during flash sintering of alumina is mainly of thermal origin. This conclusion is not in agreement with the literature data which attribute the photoemission during FS to electroluminescence.

4.1.4 Flash Sintering and Dielectric Breakdown

The results reported in this section were obtained with experimental set up n.2, at a constant furnace temperature of 1200°C, using samples pre-sintered at 1250, 1350, 1450 and 1550°C.

When FS experiments are carried out at constant furnace temperature, the most important parameter is the Incubation Time (IT). It is defined as the time needed for reaching the current limit, after that the power supply was switched on. In other words, it represents the time length where the system is working in voltage control, as it is for example shown in Figure 48 (a).

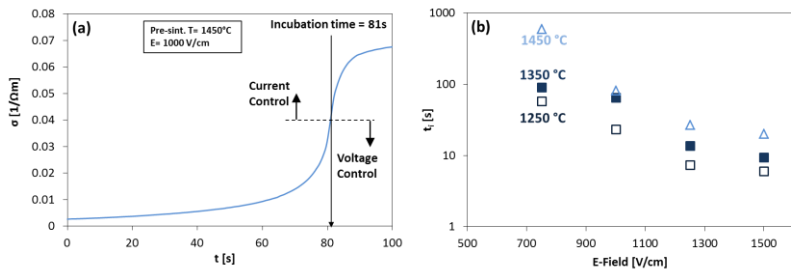


Figure 48: Conductivity evolution during the incubation of FS (a) and incubation time as a function of field strength and pre-sintering temperature (b). Modified from [16].

Figure 48 (b) points out that the incubation time is decreasing with the applied field. This is not surprising since the power dissipation during the first stage of FS is proportional to E^2 (Eq.5); so high values of E accelerates the thermal runaway.

Much more valuable is the consideration that the IT is also strongly related to the pre-sintering temperature being the sample pre-sintered at high temperature characterized by longer incubation time. In addition, the samples pre-treated at 1550°C never reached the current limit in any cases. Indeed, the microstructure of

the treated samples is strongly related to the sintering temperature. In particular in Table VIII are reported the density values for the samples prior to FS treatment. By comparing Table VIII and Figure 48 (b) we can conclude that by lowering the density of the sample it was easier to reach the flash sintering condition. In other words, the presence of pores and surfaces plays an important role during the incubation on FS in corundum.

This result is quite surprising especially if compared with other works on LSCF [24] or SiC [23] that pointed out that a pre-sintering treatment has a beneficial role on the FS behavior, lowering the onset temperature for the process. Therefore, the mechanisms leading to flash sintering are undoubtedly different.

A first possible explanation for the observed behavior is based on the fact that the presence of porosity is reducing the thermal conductivity of the material. Therefore, a thermal gradient can be produced within the less dense specimens since the heat produced by Joule effect cannot be efficiently removed from the sample center. In this way the hearth of the specimen should become progressively hotter and more electrically conductive than the surface. Finally, this should lead to FS. However, this mechanism was not observed in other materials (SiC, LSCF), where FS was easily reproduced using denser samples. In addition, some recent work have shown that these temperature gradient do not change too much the onset for FS[14]. Therefore, other reasons deserve to be sought.

Table VIII: Bulk and relative density of the samples used for FS experiments as a function of the sintering temperature.

Pre-Sintering T	1250°C	1350°C	1450°C	1550°C
Apparent density [g/cm³]	2.73	3.24	3.73	3.89
Relative density [%]	69.1	82.0	94.0	98.6

In order to explore the microstructure effect on the incubation time we can try to define the heating rate of the sample during the incubation of FS under some hypothesis:

- i. the heat is exchanged by only radiation (conduction and convection are negligible),
- ii. the sample temperature and the current flow are homogenous.

So, the power balance equation during the incubation of FS, when the system is working in voltage control, can be written as:

$$C_s m \frac{dT_s}{dt} = \frac{VE^2}{\rho(T_s)} - S\sigma\epsilon(T_s^4 - T_f^4) \quad (32)$$

where C_s is the specific heat of alumina, t the time, T_s and T_f are the sample and furnace temperatures, ρ is the electrical resistivity, E is the E-field, σ is the Stefan-Boltzmann constant, ϵ is the emissivity, m , S and V are the mass, surface and volume of the sample, respectively. Rearranging Eq. 32, and assuming that $m = BV$ (where B is the bulk density of the pre-sintered specimen), the heating rate can be written as:

$$\dot{T}_s = \frac{dT_s}{dt} = \frac{1}{BC_s} \left(\frac{E^2}{\rho(T_s)} - \frac{S\sigma\epsilon(T_s^4 - T_f^4)}{V} \right) \quad (33)$$

the derivative of the current density (J), during the incubation of FS, is proportional to the heating rate (\dot{T}_s). In fact, for ceramic materials it is possible to approximate the resistivity with an Arrhenius-like relation. Under this hypothesis it is possible to calculate the derivative of J as:

$$j = \frac{dJ}{dt} = \frac{EQ}{RT_s^2 \rho(T_s)} \frac{1}{BC_s} \left(\frac{E^2}{\rho(T_s)} - \frac{S\sigma\epsilon(T_s^4 - T_f^4)}{V} \right) \quad (34)$$

where R is the universal gas constant and Q the activation energy for conduction. Being the current limit fixed during all the FS experiments in this section (4 mA/mm²) the key parameter controlling the incubation time is j , obviously higher values of j leads to lower IT. Different parameters influence this quantity (Eq. 34). The first is, as expected, the E- field: increasing the E-Field, the derivative of J increases and the time needed for FS is reduced in agreement with the relation shown in Figure 48 (b).

According to Eq. 34 different reasons can be considered for explaining the relation between pre-sintering temperature and incubation time. First, one can observe that by increasing the pre-sintering temperature the bulk density value (B) increase (Table VIII) leading to a decrease of j . In fact, from Eq. 34 it is possible to observe an inverse-proportional relationship relating the derivative of J and B . However, being the relative bulk density of all pre-sintered bodies in the range 69.1 - 98.6%, j should be enhanced to a maximum of $98.6/69.1 = 1.43$ times. This is probably not enough for accounting the experimental data: much stronger differences were observed in the incubation times. Moreover, it does not give any explanation of why the samples pre-sintered at 1550°C did not reach the current limit in any case.

The resistivity of the system is the second parameter, which can influence the incubation time: if the material is more conductive, the derivative of J should be increased (Eq. 34). It would not be surprising that the pre-sintering temperature changes the electrical properties of the material. In fact, depending on the sintering conditions, different amounts of surface, grain boundary and pores are present in the ceramic bodies. This can lead to the activation of different conduction mechanisms or produce different cross-section available for the current flow (assuming that the current cannot flow through the air in the pores). Therefore, an estimation of the material resistivity is crucial for clarifying the runaway of FS.

Figure 49 (a) points out that if a relatively low field is used ($E < 180$ V/cm) the conduction behavior is linear and the conductivity increases with pre-sintering temperature. This is a result of the fact that porous samples are

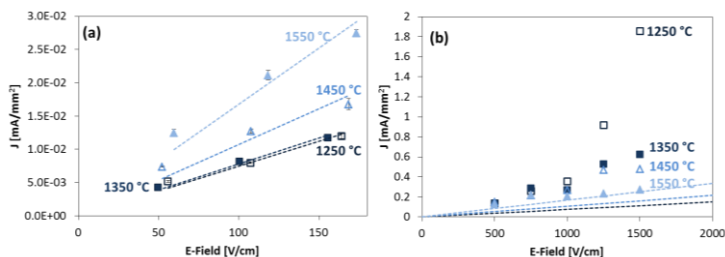


Figure 49: Electrical behavior of pre-sintered alumina samples using low (a) and high field application (b). The data are referred to the very

beginning of the incubation stage of flash sintering, when the power supply was turned on. Modified from [16].

less conductive because pores reduce the cross-section available for current flow.

Figure 49 (b) shows the electrical behavior if higher field strength are applied ($E > 500$ V/cm). The results are referred to the moment at which the voltage limit of the system is reached, at the very beginning of the incubation time. The plots indicate, in this case, a different trend: the material sintered at high temperature being less conductive. In addition, the conduction behavior is strongly non-linear and conductivity increases with E . This non-ohmic behavior is more pronounced on the porous sample (i.e. those sintered at lower temperature), while the dense specimens do not show a marked deviation from linearity (i.e. those sintered at 1550°C). This conduction behavior is probably at the base of the incubation time values reported in Figure 48 (b).

A similar deviation from the linear conduction behavior has been reported also by Cologna et al. for MgO-doped alumina[39]. They have measured the conductivity on dense specimens and observed a transition between linear to non-linear conductivity by applying a field of ~ 250 V/cm. These results are quite similar to those reported in Figure 48 (b); however, we do not observe significant deviation from linearity when using dense samples (those sintered at 1550°C). These differences are very likely associated to the different composition of the two materials, pointing out that the chemical composition and purity plays a fundamental role in conduction.

We can state, according to Figure 49, that conduction in our material is sensitive to the presence of pores and surfaces. It is well known that surfaces are characterized by a more disordered structure when compared with bulk materials. These can therefore represent a favorable path for ionic diffusion. Moreover, the surface electronic structure is also different from that associated to an ordered crystal. Hence, surfaces can be characterized by lower band gap values, rising electronic conduction.

One should finally consider that close to the pores the field is sensibly enhanced because of the interface between media with different dielectric constant, ϵ_r being equal to ~ 1 and 10 for air and alumina, respectively. For instance, assuming a spherical hole inside corundum the field is intensified of a factor 1.86 on the pore

surface[166]. Nevertheless, more complex and sharp geometry would lead to much higher field intensification. This problem has been extensively studied by Holland et al. during the incubation of FS by numerical simulations[167]. They conclude that the field is enhanced by a factor depending from the ratio between the neck/particle curvatures; i.e. assuming this ratio 0.1 it is possible to estimate a field intensification for alumina higher than 10. Indeed, pore shape and the ratio between neck/particle curvatures depend from the pre-sintering temperature; thus, the samples sintered at low temperature are not only characterized by an higher amount of pores but the pore shape would also be more sharp, leading to more significant field intensification.

Actually, field-sensitive conductivity has been already reported in different material and it is a result of the fact that the activation energy for diffusion or electron promotion can be reduced by field application. The first extensive discussion on the argument has been carried out by Frenkel in the paper “*On Pre-Breakdown Phenomena in Insulators and Electronic Semi-Conductors*” in 1938 [168]. He described the “pre-breakdown” behavior as “*an increase of electrical conductivity which finally leads to breakdown*” [168]. This phenomenon resembles what we observe before FS. The relation between E and σ in the pre-breakdown region is described by the Poole-Frenkel model [24,168–170]:

$$\sigma = \sigma_0 \exp\left(-\left(Q - \beta E^{0.5}\right)/kT\right) \quad (35)$$

where β a characteristic constant of the material. Using the natural logarithm of the conductivity Eq.35 can be linearized as:

$$\ln(\sigma) = \ln(\sigma_0) - Q/kT + \beta E^{0.5}/kT \quad (36)$$

that becomes, considering that in our experiments the furnace temperature was always the same:

$$\ln(\sigma) = A + B E^{0.5} \quad (37)$$

where A and B are two numeric constant. Using Eq.37 the experimental data in Figure 49 were interpolated. The results are reported in Figure 50; one can point out that the model provides a quite good approximation of the experimental results.

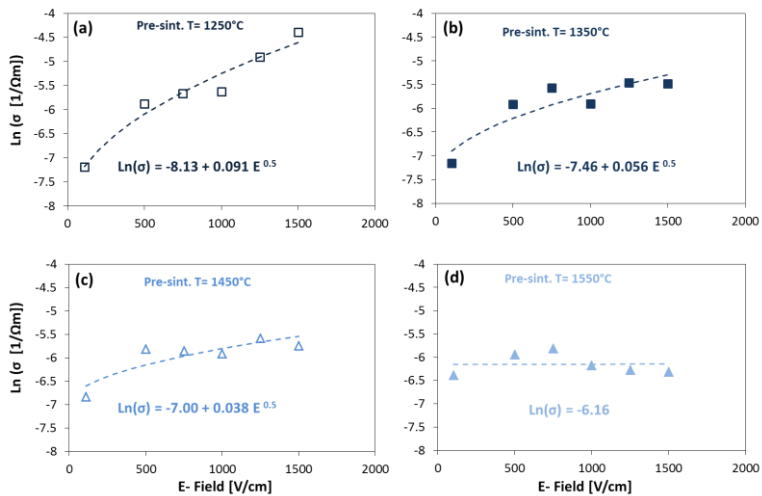


Figure 50: Conductivity for samples pre sintered at different temperature as a function of the field strength; the dashes lines represent the interpolation given by the Poole-Frenkel model. The data are referred to the very beginning of the incubation stage of flash sintering, when the power supply was turned on ($T_s \sim T_f = 1200^\circ\text{C}$). Modified from [16].

Certainly, FS and Dielectric Breakdown (DB) have other common points:

- i. The electrical behavior is similar, showing the material a transition from insulator to conductor-like;
- ii. The model described by Dissado in 1992 for dielectric breakdown [169] as a result of a thermal runaway resembles that developed by Todd for flash sintering [14];
- iii. Both FS and DB are sensitive to sample thickness, requiring thin specimens higher field/ incubation time for reproduce flash sintering [56,61] and having higher dielectric strength [171–173];
- iv. FS and DB are characterized by an incubation time, and it is in both the cases it decreases with field strength [28,41,174–176].

Now the question is: "How can be possible that a pre-breakdown behavior is observed with field of only 750 V/cm?" In fact, breakdown in insulators is usually observed with field higher than 10^5 - 10^6 V/cm[168,169].

Several points can help to answer the question. First of all, DB experiments are usually carried out at room temperature, while in this work FS was reproduced at 1200°C. The high temperature dielectric strength of alumina was studied by Miyazawa[177], Yoshimura[173] and co-workers. According to their results the dielectric strength for alumina at 1200°C is reduced down to values of 10^4 V/cm or slightly higher. Therefore, the difference between the fields needed for FS and DB is one order of magnitude.

Other considerations deserve to be pointed out. Yoshimura and Miyazawa have carried out their measures on dense and thin (40 - 1250 μm) samples. It is well known that an increase in thickness reduces the dielectric strength [171–173], for larger sample being easier to dissipate the heat produced by Joule effect. The samples used in DB experiments are at least one order of magnitude or more smaller than those used for FS; this can account for a partial decrease of the dielectric strength.

In addition, one should take in account of the porosity effect. In fact, it is well known that porosity decreases the dielectric strength [178–180] according to[181,182]:

$$E^{cr} \propto \exp(-bP) \quad (38)$$

where E^{cr} is the dielectric strength, P the porosity load, and b a numerical constant. When comparing the results on DB obtained by Miyazawa and Yoshimura with the onset field for FS measured in this work it should be taken in account that the samples that reproduces FS were porous while DB was carried out on dense specimens.

The last consideration is that the material used by Yoshimura[173] was high purity alumina (impurities ~ 10 ppm) while the powder used in this work are 99.8% pure. The purity content changes the FS behavior: while high purity alumina (99.99% pure) was never flash sintered using $E = 1000$ V/cm at 1400°C[39], 99.8% pure alumina is successfully flashed at ~1000 °C using the same field.

The combined effect of all these factors can reasonably reduce the dielectric strength down to values similar to those needed for FS. The experimental results and the literature review are, therefore, suggesting that FS and DB represents the same process in α -alumina.

4.1.5 Electrode Material Effect

The results reported in this section are referred to the experimental set up n.1; using a constant heating rate of 20°C/min.

Figure 51 provides a comparison of the flash sintering behavior of alumina treated with different electrode materials; applied as conductive pastes between the platinum wire and the ceramic. The materials used in this work are platinum, carbon and silver-based pastes. One can observe that using different electrodes the sintering process is changing in its effectiveness and in its onset temperature.

In particular one can notice that:

- i. The specimens treated with silver shrink less than the others upon sintering;
- ii. The application of a field of 250 V/cm improves the sintering behavior in the case of carbon –based electrodes, conversely, no particular advantages can be observed in the case of Pt paste application;
- iii. The samples treated with silver are sintered at lower temperature.

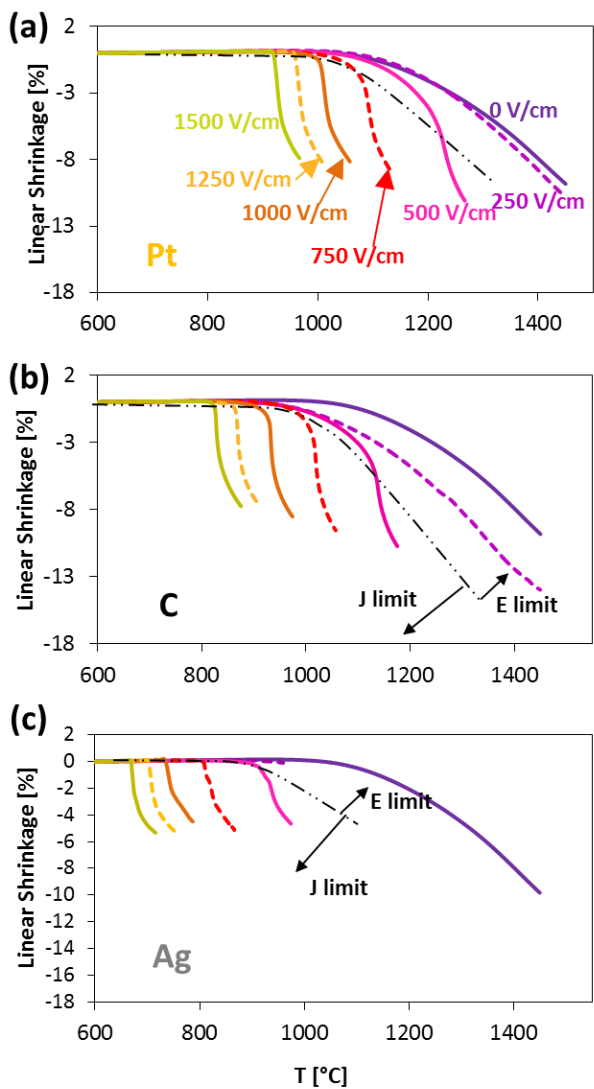


Figure 51: Dilatometric plots for samples treated using a current limit of 2 mA/mm² and different electrode materials: platinum (a), carbon (b) and silver (c).

The onset temperature for FS for the different electrodes are reported in Figure 52 as a function of the applied field. One can notice that the samples treated with Ag electrodes are flash sintered at temperatures ~ 250°C lower than those treated with Pt ones. The specimens treated with carbon-based cement exhibit an intermediate behavior.

These results are quite surprising and their interpretation is not completely clarified; also considering that the differences in activation energy for conduction for the three different electrodes is limited (section: "4.1.2 Electrical behavior"). One can argue that carbon and silver can produce some reaction at metal/ceramic interface; while Pt, being a noble element, does not produce any reaction. It is possible to speculate that carbon paste, whose stability up to 1200°C was proved via TG analysis (not reported), can promote some oxy-reductive reaction; i.e. by the combined effect of E/J and a change of the oxidation state of C the formation of a partially-reduced alumina can be promoted, leading to electrical conductivity increase.

Regarding silver electrodes different hypothesis can be proposed:

- i. Silver work function (4.5 – 4.7 eV) [183][184] is lower when compared with that of Pt (5.1-5.9 eV)[183][184]. Hence, it is more easy for electrons to be removed from the electrode and enter in the ceramic body.
- ii. Silver produces monovalent ions that can substitute Al^{3+} leading to the formation of oxygen vacancies for balancing the charge.
- iii. Although silver was not detected by EDS in the center of the gage section, silver ions diffusion in alumina it is known to be much more fast when compared with Al and O self-diffusion process[185][186]. A conduction mechanism based on Ag^+ diffusion can be proposed, explaining the anticipate flash event.

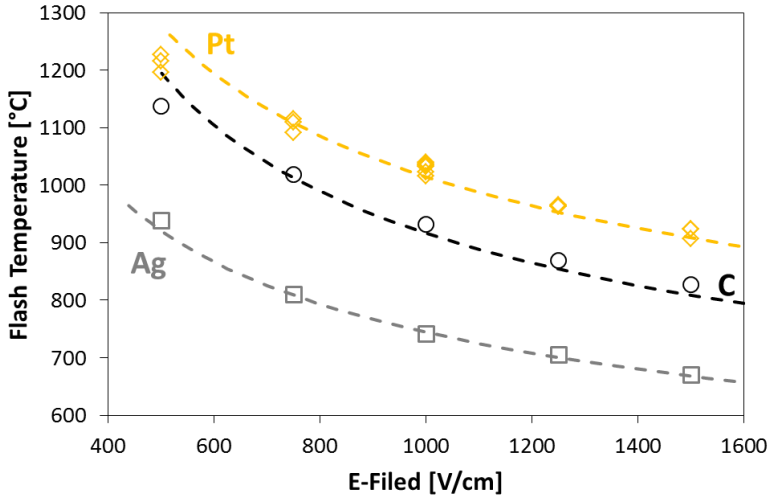


Figure 52: Onset temperature for FS as a function of the applied field strength for different electrode materials. Modified from [55].

The data in Figure 52 were fitted using the model developed by Todd et al. for the thermal runaway for FS[14]. This model, as described in section “1.4.1 Thermal runaway and Joule heating”, defines the onset condition for FS when the curves representing the heat dissipated by radiation and the electrical power (as a function of the sample temperature) are tangent. Under this condition the following equations should be satisfied:

$$\frac{E^2 V}{\rho_0} \exp\left(\frac{-Q}{R(T_f + \Delta T)}\right) = S\sigma\epsilon((T_f + \Delta T)^4 - T_f^4) \quad (39)$$

$$\frac{E^2 V}{\rho_0} \frac{Q}{R(T_f + \Delta T)^2} \exp\left(\frac{-Q}{R(T_f + \Delta T)}\right) = 4 S\sigma\epsilon(T_f + \Delta T)^3 \quad (40)$$

where ΔT is the overheating of the tangent point with respect to the furnace temperature. Eq. 40 can be rearranged, allowing to explicate the electric field:

$$E^2 = \frac{4 S\sigma\epsilon R \rho_0}{V} \frac{(T_f + \Delta T)^5}{Q} \exp\left(\frac{Q}{R(T_f + \Delta T)}\right) = D \frac{(T_f + \Delta T)^5}{Q} \exp\left(\frac{Q}{R(T_f + \Delta T)}\right) \quad (41)$$

where D is a numerical constant. Combining Eq.39 and 40 a quintic equation is obtained:

$$\frac{4R}{Q} T_s^5 - T_s^4 + T_f^4 = 0 \quad (42)$$

with $T_s = T_f + \Delta T$. This model represent an approximation; in fact it is based on the assumption that the sample temperature is homogenous and the time needed for the thermal runaway, once that the onset is reached, is negligible. Nevertheless, a similar delay is present in all samples and the sample thickness was limited reducing thermal gradients.

The experimental data were fitted by recursive method, following these steps:

- i. A first value for the activation energy was assumed equal to 0.52 eV;
- ii. Using Eq. 42 and the experimental data for the onset furnace temperature (T_f), T_s was calculated for each sample using NSolve function in Mathematica®;
- iii. A new value for Q and for the constant D was calculated from Eq .41 by FindFit command in Mathematica®;
- iv. With the new Q value, all the operations were repeated until convergence: i.e. the activation energy changing less than 0.0005 eV between two successive iterations.

The best fit was obtained using Q equal to 1.57, 1.37 and 1.32 eV for platinum, carbon and silver electrodes, respectively. These values are not far from those obtained from the power dissipation plots and from the light emission/conductivity relation. As shown in Figure 52 the fit (dashes lines) is nearly perfect for Ag electrodes, the error being always lower than 17°C.

A deviation from the interpolating curves is observed for the samples treated with 500 V/cm and Pt/C electrodes, the experimental onset temperature for flash sintering being lower than the calculated one. This can be considered a result of fact that the sample is changing its electrical properties upon heating:

- i. The samples treated with 500 V/cm (Pt and C) are partially shrunk when the flash condition is reached; this is leading to a field intensification, being the gage section reduced.
- ii. The material is partially sintered before the current limit is reached. The neck formation provides a continuous path for current flow and may enhance conductivity.

The electrode material changes also the densification achieved during the process; in fact, Figure 51 points out that different shrinkage are obtained by changing the used conductive paste. The results are confirmed by density/porosity measurements, reported in Figure 53. One can observe that the densification of the specimens treated with Pt and C is very similar and the main difference consists in the samples treated with 500 V/cm. This is due to the fact that before FS these specimens are already partially shrunk as a result of thermal/FAST sintering (see “4.1.1 Densification behavior and microstructural evolution”); thus, the samples treated with C being flash sintered at a temperature approximately 100°C lower than those treated with Pt, the densification phenomena prior to FS are limited. This has an effect on the density measured on the sintered bodies.

Conversely, the samples sintered with Ag electrodes are always less densified. Another difference is that in the case of Pt/C electrodes the densification is reduced by increasing the field (as a result of the sintering shrinkage prior to FS), while in the samples treated with Ag an opposite behavior can be pointed out.

In order to understand the densification behavior the estimated sample temperatures, for different emissivity values, are reported in Table IX. One can point out that the samples treated with Ag electrodes reached lower temperatures during the flash, as a result of the fact that they were flash sintered at lower temperatures, when compared with those treated with Pt or C. The difference could be also underestimated. In fact, in the case of the specimens treated with silver the onset temperature for FS ranges between 670 and 940°C, thus a partial contribution of convection (not calculated) should be taken in account, leading to a further decrease of sample temperature.

Nevertheless, this is not explaining why in the case of specimens treated with silver electrodes the density increases with E, the sample treated with 500 V/cm being

more porous. One can speculate that this sample was treated at a temperature close to silver melting, thus a partial diffusion of silver ions can be suggested within the sample. The diffusion would be enhanced by the E-field which drives the cation migration. If the conduction is mainly based on silver diffusion the partially reduced-alumina (see “4.1.2 Electrical behavior”) would be only weakly formed; retarding the densification mechanisms. One can also speculate that Ag can sublime (at 1200°C its vapor tension is about 0.2 Tor) and promote charge transport in its ionized vapors. This point is, in any case, not completely clarified and deserves further analysis.

Although the mechanisms are not completely clarified, in this chapter we showed that the electrodes play an important role on the flash sintering behavior of alumina. This may open a new way for future studies and allow a further reduction of the sintering temperatures.

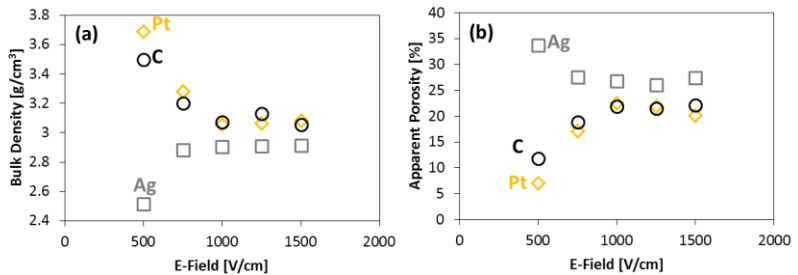


Figure 53: Bulk density (a) and apparent (b) of sample treated using different electrode materials and a current limit of 2 mA/mm². Modified from [55].

Table IX: Estimated sample temperature [°C] during FS for samples treated with different electrodes as a function of the field strength (current limit = 2mA/mm²).

$\epsilon = 0.9$	E [V/cm]
------------------	----------

		500	750	1000	1250	1500
Electrode	Pt	1360	1270	1223	1222	1206
	C	1324	1226	1177	1153	1153
	Ag	1143	1117	1112	1087	1111

$\varepsilon = 0.7$		E [V/cm]				
		500	750	1000	1250	1500
Electrode	Pt	1389	1308	1268	1273	1260
	C	1291	1271	1225	1207	1212
	Ag	1185	1172	1176	1150	1181

$\varepsilon = 0.5$		E [V/cm]				
		500	750	1000	1250	1500
Electrode	Pt	1437	1338	1362	1343	1344
	C	1379	1342	1302	1291	1302
	Ag	1253	1258	1272	1247	1286

4.2 Flash sintering of glass-containing alumina

4.2.1 Densification behavior and Microstructural Evolution

Figure 54 shows the dilatometric plots referred to pure Alumina (A) and magnesia-silicate Glass-Containing Alumina (MgGCA) flash sintered using different fields and a current limit of 2 mA/mm² (the current limit was maintained for 2 min). The results point out the beneficial effect of glass addition on the field-assisted sintering behavior of the material; being the MgGCA samples characterized by much higher sintering rates (i.e. the slope of the dilatometric plot) and higher sintering shrinkage. This is a result of the different sintering mechanisms which consist in solid state sintering and

liquid phase sintering for A and MgGCA, respectively. The presence of liquid phase provides a fast diffusion path for the ionic species and allows, through dissolution/precipitation mechanisms, a rapid densification[3]. Additionally, the liquid phase presence enhance the sintering stresses via capillarity forces, increasing the attractive load between particles and thus, also, the sintering rates [3]. An exception is represented by the samples treated using 1500 V/cm; in this case the glass-containing material is not densified. A possible explanation of the observed behavior can be related to the fact that these samples were flash sintered at a very low furnace temperature (650 – 750 V/cm) and this leads to a decrease of the specimen temperature during the third stage of FS.

A second consideration that deserves to be underline is that the MgGCA dilatometric curves present two main shrinkage events (Figure 54(b)). The first event takes place at low temperature and it is responsible for a moderate shrinkage ($\sim 2\%$); whereas the second happens at higher temperature, once the current limit is reached, and it is responsible for the main part of the densification. Indeed, it is well-known that Liquid Phase Sintering (LPS) can be divided in different stages and each stage can lead to different shrinkage events that can be observed via dilatometric test.

At first, particles rearrangement due to liquid phase formation takes place; leading to a moderate shrinkage. The temperature at which this phenomenon happens is influenced by the field strength as it can be observed in Figure 54 (b); the phenomenon being anticipated by increasing E. Since in these experiments the liquid is provided by the softening of the glassy phase we can state that the field changes the viscous properties of the glass. Nevertheless, the magnitude of this first, moderate shrinkage does not change too much changing the field strength. Therefore, we can state that the E-field application modifies the temperature at which particle rearrangement happens but it does not influence, at a first approximation, the shrinkage that can be obtained.

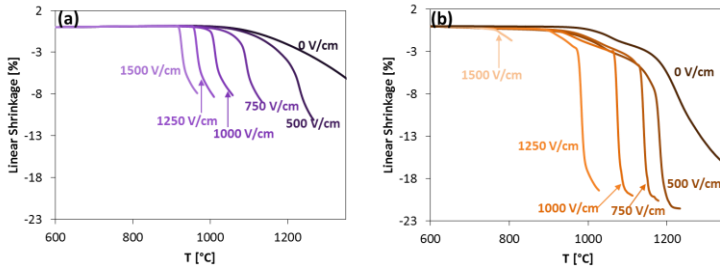


Figure 54: Dilatometric plots for pure alumina (a) and 10 wt% magnesia silicate glass-containing alumina (b) using different field strength and a current limit of 2 mA/mm². Green density ~ 1.76 g/cm³, current limit maintained for 2 min. Modified form [187].

The second part of the shrinkage, as reported by Rahaman[3], is due to “*Densification. . .by solution-precipitation*”. During the field-assisted sintering experiments it is mainly obtained after the current limit reaching. This phenomenon is reproduced at lower temperature via E-field application and its rate is drastically increased in FS experiments when compared with conventionally sintered sample (0 V/cm in Figure 54 (b)).

In order to point out the glass composition effect on flash sintering, a pure silica glass, produced via sol gel method, was added to alumina powder, following the same procedures described for magnesia-silicate glass. The sample was treated with 1000 V/cm up to 1220°C and then the experiment was interrupted because of sparking. This material do not reproduce the flash event, pointing out that the presence of Mg²⁺ ions is fundamental in field-assisted sintering experiments. This is due to the fact that pure silica is extremely resistive and it does not allow the thermal runaway process. Conversely, Mg²⁺ diffusion increases conductivity and power dissipation, triggering FS.

Figure 55 compares the physical properties of A and MgGCA flash sintered bodies. As expected, glass-containing material is more densified and it is characterized by much lower amount of open pores. The differences are less marked when bulk density is taken in account; nevertheless, the theoretical density for the two materials is different. In fact, the theoretical density for corundum is 3.95 g/cm³; while for MgGCA (under the assumption that the density of the glass is 2.20 g/cm³) it is only

3.66 g/cm³. An exception is represented, once again, by the specimens treated with 1500 V/cm. In this case the glass-containing material is not densified, coherently with the dilatometric plot results (Figure 54).

These results have important technological implications because they suggest that, by glass addition, it is possible to reduce the current needed for densification and the power dissipation during the process. This leads to clear advantages in terms of power consumption and it avoid the risk of electrodes melting and sparking.

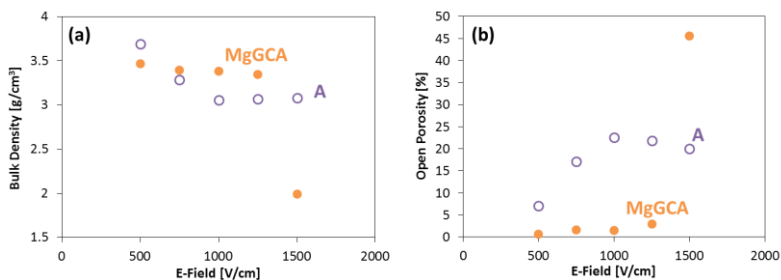


Figure 55: Bulk density (a) and open porosity (b) values measured on A and 10 wt% MgGCA samples flash sintered using different fields and a current limit of 2 mA/mm² (current limit maintained for 2 min). Modified form [187].

The effect of the current limit on the densification behavior of MgGCA is reported in Figure 56. One can observe that, similarly to what reported in the previous section for pure alumina, the current density is the key parameter controlling bulk density and open porosity. In addition, it should be pointed out that, if a relatively high current is applied (i.e. 2 mA/mm²), the densification is independent from the field strength and the material is well densified (excluding the samples treated with 1500 V/cm). Conversely, in the case of the use of lower current the density rises by decreasing the field. This is due to the fact that the samples treated with lower field are already partially shrunk when FS happens and it has an effect also on the final density of the sintered bodies.

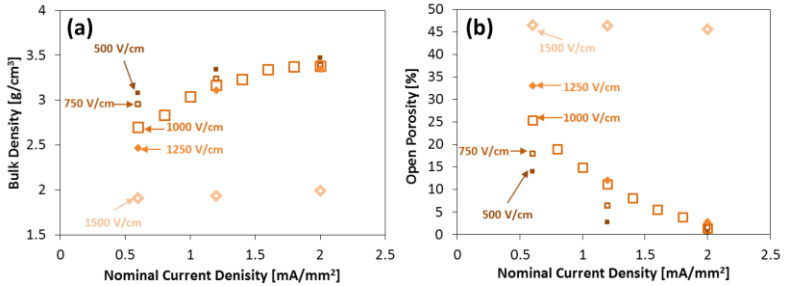


Figure 56: Bulk density (a) and open porosity (b) as a function of the current density for 10 wt% MgGCA specimens. Green density $\sim 1.76 \text{ g/cm}^3$, current limit maintained for 2 min. Modified form [187].

Current density and powder composition have also an effect on the obtained microstructures (Figure 57). In particular we can observe that, using the same condition of field (1000 V/cm) and current (2 mA/mm²), the glass-containing sample is more dense and characterized by a lower amount of porosity when compared with the pure alumina one. Nevertheless, SEM micrographs point out that different fracture mechanisms are involved in the two materials: intergranular and transgranular for A and MgGCA, respectively. These microstructures provide indication about the sintering mechanism; in fact, it is well known that alumina presents intergranular fracture in case of solid state sintering, whereas it is transgranular when the densification happens via liquid phase sintering. The micrographs are therefore an evidence that MgGCA is densified by a sort of liquid phase flash sintering process. In addition, comparing Figure 57(b) and (c) it is possible to observe the current effect on the microstructure of the glass-containing material: although lowering the current down to 0.6 mA/mm² the porosity increases (coherently with density measurement), the material always presents microstructural features that can be ascribed to liquid phase sintering.

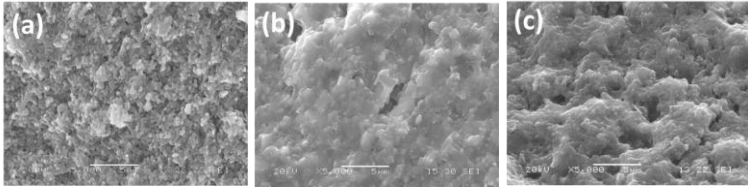


Figure 57: SEM micrographs of the fracture surfaces of A (a) and MgGCA (b) samples treated using 1000 V/cm and 2 mA/mm². One can also observe the current effect on densification by comparing the MgGCA samples treated using 2 mA/mm² (b) and 0.6 mA/mm²(b). Modified form [187].

Additional microstructural details can be observed in Figure 58, where the microstructures of the polished MgGCA specimens are reported before and after HF etching. One can observe that a lot of porosity gets opened by etching; this is in other words meaning that a lot of glass is still present in the sintered bodies. Furthermore, one can notice that the porosity, that is created during the etching process, is characterized by very sharp and elongated shapes. Therefore, we can state that during FS the glass is able to flow between the solid alumina grains, even if the treating time was very limited (2 min). This is an additional evidence that a liquid phase sintering takes place during flash sintering of MgGCA.

The decrease of glass viscosity that allows an effective liquid phase sintering process resembles what has been reported by McLaren et al. describing the electric field-induced glass softening[119]. They observed that at a given combination of field/temperature the glass changes its flowing properties with an abrupt drop of its viscosity. Simultaneously, the material becomes electrical conductive and a strong light emission has been observed. Nevertheless, the mechanisms that leads to electric-field induced softening have not been completely clarified and they “may include non-uniform Joule heating, dielectric breakdown, and electrolysis”[119].

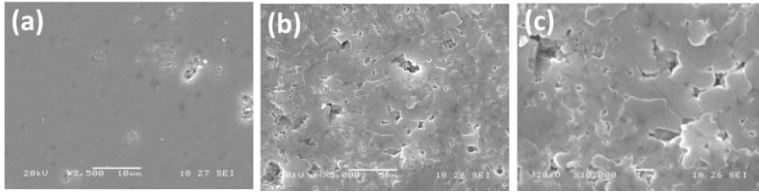


Figure 58: SEM micrographs of MgGCA polished (a) and polished and HF etched (b,c) specimens treated using 1000 V/cm and 2 mA/mm². Modified form [187].

The last microstructural feature that deserves to be analyzed is the grain size evolution after the flash sintering treatments for MgGCA samples. In order to perform this measure, the fracture surfaces of the samples were HF etched. The removal of the intergranular glassy phase allows to highlight the grain boundaries as it is shown in Figure 59. First of all we should underline that the grains are generally equiaxial and very few elongated grains can be observed. The formation of elongated grains has been often recorded in alumina sintered with glass formers addition [188]; in fact, the dissolution/precipitation phenomena can happen along preferential crystallographic orientations. The fact that in flash sintered bodies this phenomenon is poorly observed is probably related to the very short treating time that do not allow consistent grain coalescence.

The grain size, measured by linear intercept method in the center of the gage section, are summarized in Table X. The average grain size is in all the cases sub-micrometric, even if in the case of the samples treated with 2 mA/mm² some large grains (larger than 1 μm) can be observed (Figure 59). Abnormal grain growth has been reported also in conventionally sintered alumina with the addition of a liquid phase [129], thus the result is not particularly surprising. Furthermore one can notice that, similarly to what reported for pure alumina, the key parameter controlling the grain size is the current density: being the grain size increasing by increasing the current density. Nevertheless, the samples treated with 1500 V/cm present grains substantially smaller when compared with those treated with lower fields and, even increasing the current up to 2 mA/mm², a very poor grain coalescence can be observed.

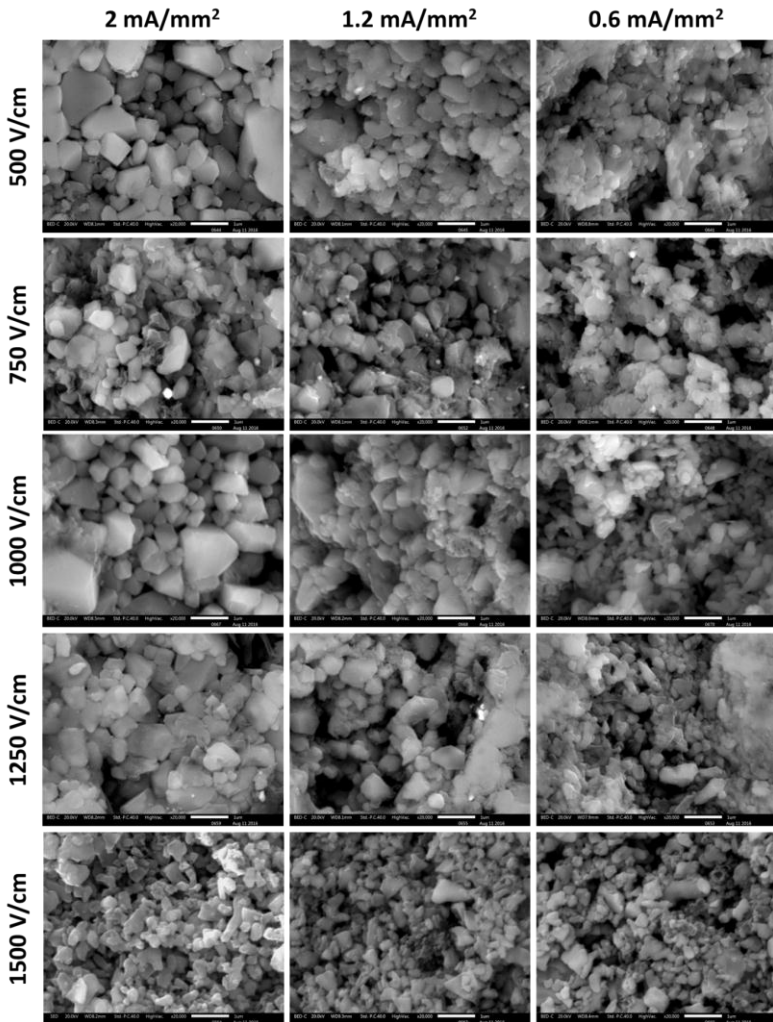


Figure 59: SEM micrographs of HF etched sample (MgGCA) treated using different combination of E and J (the inter-granular porosity is opened by the etching process). Modified form [187].

Table X: Average grain size and standard deviation [nm] of flash sintered MgGCA samples treated using different field and current.

		J [mA/mm ²]		
		0.6	1.2	2.0
E [V/cm]	500	359 ± 58	453 ± 52	532 ± 98
	750	321 ± 42	411 ± 85	492 ± 65
	1000	315 ± 35	470 ± 70	518 ± 40
	1250	317 ± 70	396 ± 60	502 ± 54
	1500	315 ± 25	345 ± 47	402 ± 51

At this point, the obtained microstructures should be compared with those obtained via conventional sintering processes. For this purpose it is first necessary to estimate the sample temperature during the steady stage of FS. The specimen temperature was estimated by using the power balance equation (Eq.10) assuming different values for the emissivity. The results are summarized in Table XI. Coherently with what was observed for pure alumina, the current density is the main parameter controlling the sample temperature; nevertheless, the equilibrium temperature decreases by increasing the field as a result of the different onset for FS. The samples treated with 1500 V/cm are substantially colder than the others, since they were flash sintered at very low furnace temperature. This could be the reason explaining why they were not densified efficiently.

Table XI: Average sample temperature during the third stage of flash sintering of MgGCA for different values of ϵ .

$\epsilon = 0.9$		$J \text{ [mA/mm}^2\text{]}$							
		0.6	0.8	1.0	1.2	1.4	1.6	1.8	2.0
$E \text{ [V/cm]}$	500				1224				1314
	750				1242				1266
	1000	1176	1193	1204	1221	1226	1239	1256	1255
	1250				1163				1200
	1500				1027				1108

$\epsilon = 0.7$		$J \text{ [mA/mm}^2\text{]}$							
		0.6	0.8	1.0	1.2	1.4	1.6	1.8	2.0
$E \text{ [V/cm]}$	500				1298				1338
	750				1263				1292
	1000	1194	1217	1230	1245	1254	1268	1289	1292
	1250				1194				1242
	1500				1087				1175

$\epsilon = 0.5$		$J \text{ [mA/mm}^2\text{]}$							
		0.6	0.8	1.0	1.2	1.4	1.6	1.8	2.0
$E \text{ [V/cm]}$	500				1325				1377
	750				1298				1334
	1000	1224	1257	1270	1286	1301	1316	1343	1352
	1250				1247				1309
	1500				1179				1277

One further point should be considered: even assuming a low emissivity value (i.e. 0.5) the estimated temperatures are in almost all the cases lower than 1355°C which is the liquidus temperature of the ternary system MgO – SiO₂ – Al₂O₃. This is quite surprising considering the obtained microstructures that suggested an effective liquid phase sintering process. In fact, being the first thermodynamically stable liquid formed at 1355°C a conventional liquid phase sintering treatment should be carried out at higher temperatures; otherwise, the glass would soften and then it rapidly

crystallizes forming solid crystals which do not improve sintering. The glass crystallization could be also quickened by the presence of a huge amount of surfaces and interfaces between alumina grains and the glass. Such mechanism prevents an efficient conventional densification at temperature lower than 1355°C. In order to prove this statement a MgGCA sample was conventionally sintered at 1350 °C with a dwelling time of 2 h (heating rate = 10°C/min). A very porous microstructure is obtained (Figure 60 (a)) with a density of 2.99 g/cm³. The formation of new crystalline phases, mainly a magnesium-aluminum silicate (sapphirine), was detected by XRD (Figure 60(b)). Even repeating the treatment at a higher temperature (1370°C) the density increases only up to 3.11 g/cm³. In fact, at 1355°C a liquid phase is formed but, in such temperature range its content is very limited and does not allow a complete densification.

Therefore, we can conclude that by flash sintering it is possible to obtain an effective densification of MgGCA at sample temperatures lower than the thermodynamic liquidus in a very short time (2 min). This cannot be accounted for by conventional sintering mechanisms even assuming long soaking times (up to 2 h), but it can be based on mechanisms similar to those reported for electric field- induced softening. In this chapter we showed the applicability of flash sintering to glass-containing ceramics, allowing a consistent expansion of the application field of FS. The densification takes place via liquid phase sintering mechanisms, as in conventional processes in similar materials; however, the densification rates seem to be remarkably accelerated by the current flow.

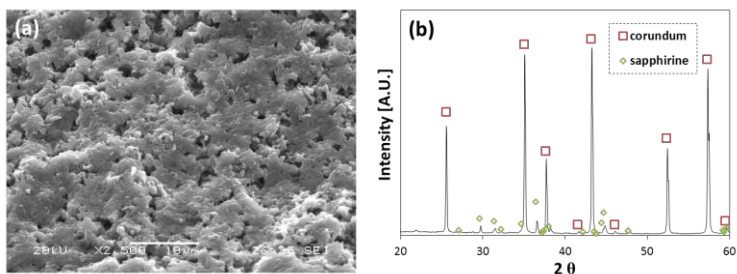


Figure 60: SEM micrograph (a) and XRD pattern (b) of a MgGCA specimen treated at 1350°C for 2 h. Modified form [187].

4.2.2 Electrical behavior and onset for flash sintering

The onset temperature for flash sintering for pure alumina and glass-containing alumina are reported in Figure 61. First of all one can notice that the behavior of A system is regular, with an exponential-like shape. In fact, it is coherent with the model for the thermal runaway for flash sintering as previously reported.

Conversely, MgGCA presents a much more complex and non-regular relation. In particular, if an high field is applied (1500 V/cm) MgGCA is flash sintered at a very low temperature when compared with pure alumina; whereas, by decreasing the field the onset for flash sintering is delayed in the glass-containing material. Finally, in the case of a low field application (500 V/cm) the flash event takes place at the same temperature in the two systems.

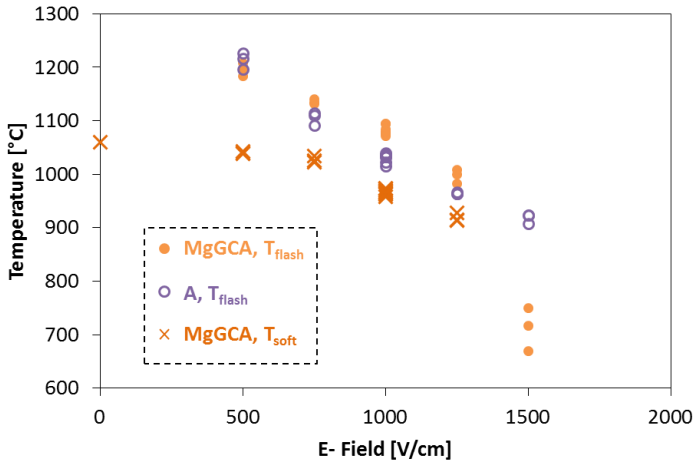


Figure 61: Onset temperature for flash sintering in MgGCA and A systems as a function of the field strength. The temperature at which the maximum shrinkage rate is reached during glass-softening (MgGCA) is also reported. Modified form [187].

This non-regular relation is due to the electrical behavior of the material; in fact, the onset for FS is related to the electrical conductivity. A comparison between the specific power dissipation in pure alumina and MgGCA is provided in Figure 62 (a). One can observe that at low temperature (right portion of the plot), the glass-

containing material is more conductive and the power dissipation plot is characterized by a different slope when compared with pure alumina. In particular, the activation energy is 1.2 ± 0.2 and 0.7 ± 0.1 eV for A and MgGCA, respectively. Thus, the conduction mechanisms in the two systems are undoubtedly different and the glassy phase enhances the total conductivity of the material; this suggesting that, the glass is more conductive than the alumina powder in this temperature region. The estimated activation energy for conduction of the glass-containing system is much lower than the energy barrier for diffusion in silicates and glasses (2.0 – 4.3 eV) [189–193] and far different from the band gap in fused silica (8.3 eV)[2]. This can be related to the fact that the glass was produced via sol-gel method, therefore it presents structures far from equilibrium. Precedent works have point out that the energy barrier for diffusion in sol-gel glasses is lower when compared with bulk materials and this results also in an increase diffusivity (even one order of magnitude higher)[194]. In Figure 62 (b) it is possible to observe that the sample treated with 1500 V/cm presents a different activation energy; in fact, the slope of the plot is higher (1.6 eV). This can be related to the field-induced activation of different conduction mechanisms [195,196].

When the temperature increases, MgGCA becomes more resistive than pure alumina (Figure 62(a)) and this is responsible for the delayed FS event ($E = 750 - 1250$ V/cm). In the same temperature region, it is also possible to observe that the power dissipation plot of the glass-containing material presents a certain instability, producing a sort of hill. First, the power dissipation starts increasing as before FS; but, after few minutes, the concavity turns downward and MgGCA becomes less conductive than A.

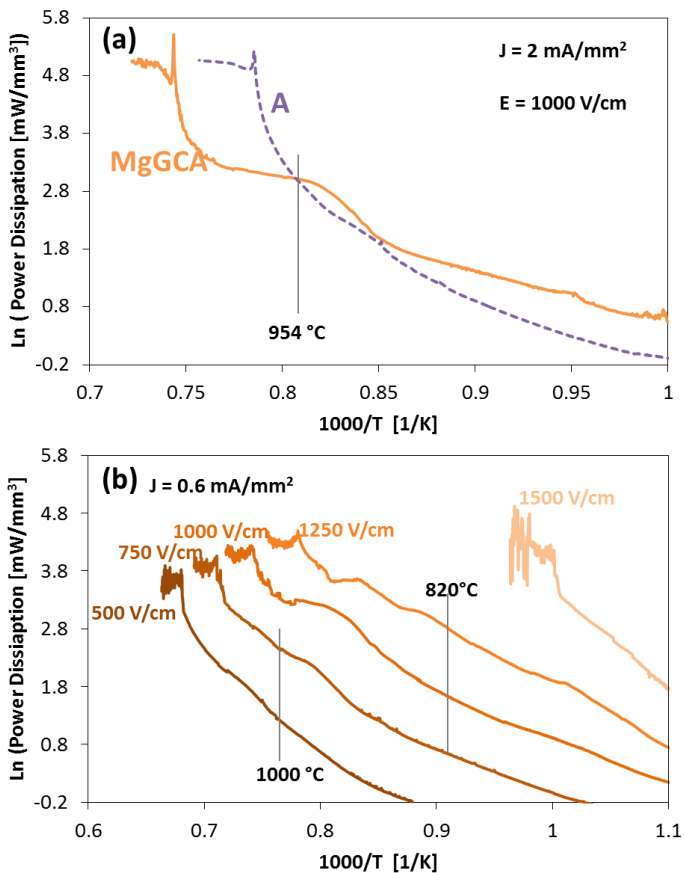


Figure 62: Comparison between specific power dissipation in pure alumina and MgGCA (a) using 1000 V/cm and 2 mA/mm^2 . The effect of the field strength on the power dissipation of MgGCA is also reported (b). Modified form [187].

In order to analyze this instability a DSC analysis was performed on the glass-containing powder and it is reported in Figure 63. One can notice the presence of an exothermic peak at $\sim 860 \text{ }^\circ\text{C}$. This peak is very likely related to some modification in the glassy phase, like a partial crystallization. In fact, by comparing the XRD pattern (not reported) obtained on the glassy powder before and after a thermal treatment up to $900 \text{ }^\circ\text{C}$ (heating rate = $20 \text{ }^\circ\text{C/min}$) it is possible to state that some magnesium

silicate (enstatite) is formed during the process. The precipitation of enstatite decreases the magnesium load in the glass, which becomes more resistive. This leads to the curvature change in the power dissipation plots and to the delayed flash sintering phenomenon in MgGCA using field in the range 750 – 1250 V/cm. Conversely, the specimens treated with 1500 V/cm are flash sintered before this exothermic peak, thus in a temperature region in which the glass is much more conductive than alumina. This accounts for the anticipate flash sintering of the glass-containing powder using 1500 V/cm.

Finally, in the case of the treatment with 500 V/cm the two materials present a very similar onset temperature, even if it is well higher than the crystallization peak. This can be explained considering that at such temperatures MgGCA samples are already partially shrunk before FS (~ 8%), much more than pure alumina (~ 4%). This results in a significant field intensification (being the system in voltage control) that anticipate FS of the glass-containing powder.

One last consideration from Figure 61 deserves to be drawn and it is related to the glass softening behavior. One can observe that if high field is applied ($E > 750$ V/cm), the temperature at which the maximum shrinkage rate is obtained during glass softening (due to particles rearrangement) is following a behavior very similar to the onset for flash sintering: being the particles rearrangement preceding FS of 80 – 110°C. This can be related to the fact that Joule heating takes place during the incubation of FS and this leads to an anticipate glass softening event. Nevertheless, if a lower field is applied ($E < 750$ V/cm), the softening temperature is weakly changing, even decreasing the field down to 0 V/cm. This can be due to the fact that in these cases the softening temperature is enough far from the onset for flash sintering, so the Joule effect can be neglected. Additionally, in such a temperature region the glass is more resistive than alumina (power dissipation plot in Figure 62), thus it is marginally involved in the charge transport mechanisms.

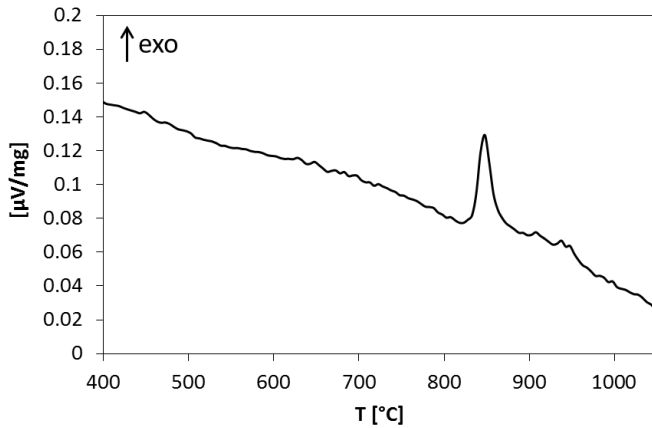


Figure 63: DSC of MgGCA powder (heating rate = 20°C/min).

At this point the attention should be focused on the electrical behavior of MgGCA during the third stage of FS, after the current limit reaching. Indeed, the sample temperature is unknown because of Joule heating. Therefore, similarly to what reported for pure alumina, we estimate the sample temperature using the power balance equation (Eq.10) in the second minute after the flash event. The plot is based on the approximation that the sample temperature is considered to be homogeneous. This is not the real condition because a temperature asymmetry close the two electrodes takes place. Figure 35 pointed out that the anode is hotter than the cathode when pure alumina is flash sintered; similarly Fig. 5 in Ref. [119] reveals that one electrode is brighter than the other. Nevertheless, we can notice that in both the cases the sample volume where such asymmetry is present is very limited with respect to the total volume of the sample. Therefore, the assumption of homogeneous specimen temperature seems not to be so unreasonable.

The best fit of the experimental results was obtained using an emissivity of 0.54 and an activation energy of 2.5 eV (Figure 64). Several considerations arise from the observation of Figure 64:

- i. The sample temperature is in almost all cases lower than the liquidus temperature as previously shown.

- ii. The estimated emissivity is not far from data available in literature[197–199].
- iii. The material during the third stage of FS is more conductive than what expected from the conductivity measurements carried out before the flash event. This can be related to the activation of different diffusion paths during the process.
- iv. The activation energy for conduction is different before and after the flash even. In particular during the third stage of FS the activation energy is 2.5 eV, and even changing the emissivity in a wide range (0.2 – 1.0), Q is always higher than 1.1 eV. These values are far higher than the energy barrier for conduction estimated during the incubation (0.7 eV); highlighting the activation of different mechanisms. The value of Q during the third stage of FS is well comparable with the activation energy for diffusion in silicate melts and glasses; in fact value in the range between 1.1–2.9 eV have been previously reported for Si^{4+} , Mg^{2+} and O^{2-} diffusion [193,200–204]. This is suggesting that the glassy phase is playing a central role in the charge transport mechanisms during the flash.

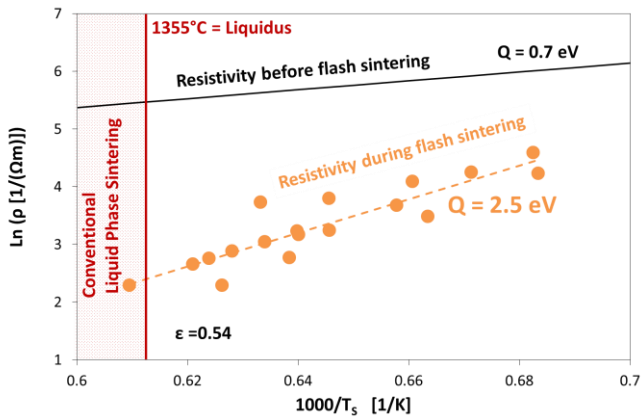


Figure 64: Resistivity during the third stage of FS as a function of the estimated sample temperature for MgGCA. One can observe that the behavior is different from what measured during the incubation of the process (black line). Modified form [187].

A comparison between the estimated resistivity during FS for the two systems: pure alumina and glass-containing alumina is provided in Figure 65. The figure refers to two different values for emissivity: 0.5 and 0.7; these values were chosen since in this emissivity range the best were obtained. One can observe that the two systems present far different behavior. First, the activation energy for conduction (i.e. the slope of the plots) is higher in the glass-containing system. Thus, the conduction mechanisms for the two materials are undoubtedly different: whereas for pure alumina conduction is probably mainly electronic and enhanced by the formation of partially-reduced structures, in the case of glass-containing alumina a central ionic contribution can be point out, according to the Q values.

Second, we can observe that the two resistivity plots are somehow intersecting each other. This suggests that if the temperature is low (right portion of the plot) MgGCA is more resistive, while increasing the temperature MgGCA becomes more conductive. This is not particularly strange considering that the point acquired at low temperature are closer to the pre-flash behavior: MgGCA being more resistive than pure alumina in the temperature range before the flash event (Figure 62). Conversely, increasing the applied current and the sample temperature, the glassy phase rapidly decreases its viscosity allowing faster conduction via liquid phase diffusion.

The presence of ionic conduction for MgGCA is yet proved only by the resistivity plots; nevertheless, some other experimental evidences can prove this phenomenon. Figure 66 provides an EDS linescan analysis of the Mg concentration close to the anode and cathode for a sample treated using 2 mA/mm² and 750 V/cm. One can observe that an higher Mg concentration was recorded in the cathodic area, while a lack of magnesium is present close to the anode. Moving from the electrodes, the Mg counts reached a plateau at ~ 700 and ~ 300 μm from the cathode and anode, respectively; starting from these pints the concentration is constant in whole the gage section.

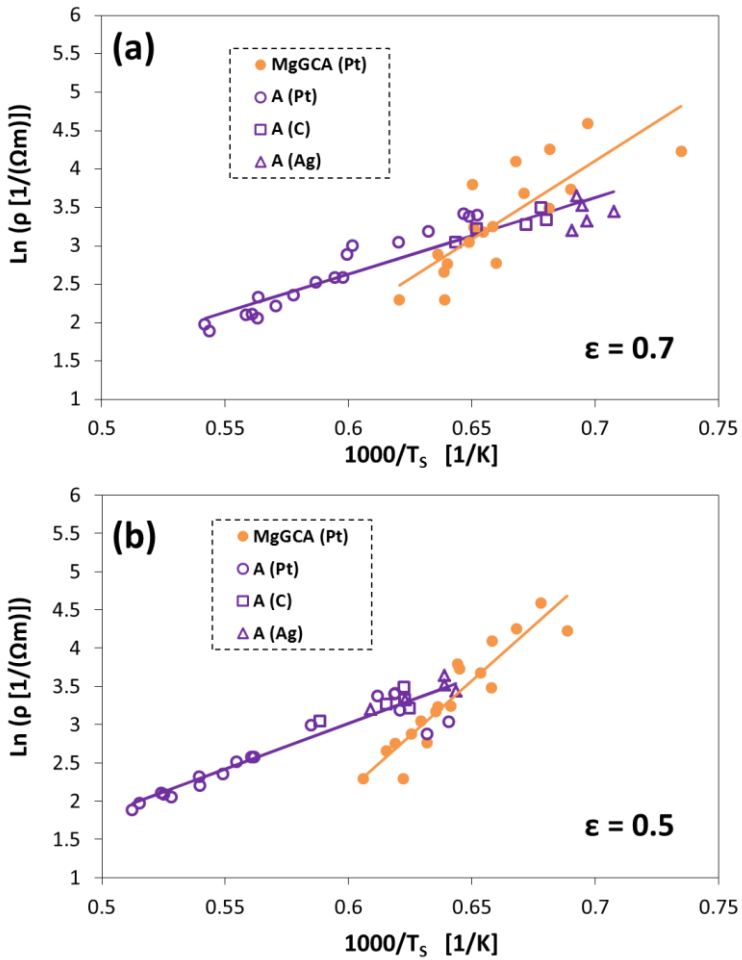


Figure 65: Electrical resistivity as a function of sample temperature for pure alumina and magnesia silicate glass-containing alumina assuming $\epsilon = 0.5$ (a) and 0.7 (b).

Similar results can be observed also by EDS maps. Figure 67 points out the formation of a magnesium enriched area close to the cathode; while the concentration of silicon is substantially constant. The Mg enriched area grows with the applied field and it forms a quite wide stain using $E \geq 1000$ V/cm. The results are

therefore clearly showing that a contribution of Mg^{2+} migration to conduction during the process is present.

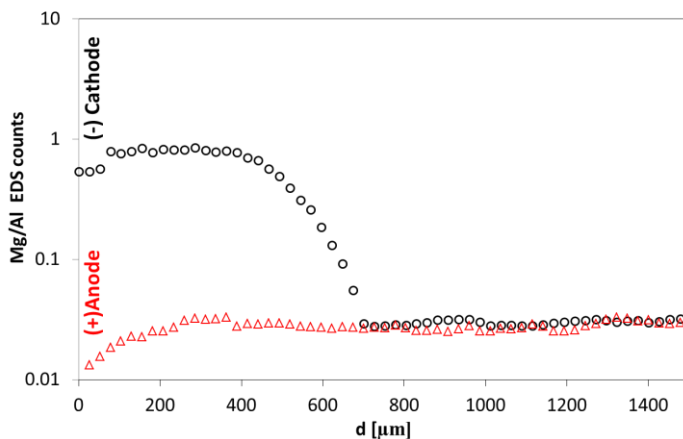


Figure 66: Ratio between magnesium and aluminum EDS counts at different distances from the cathode (black circles) and anode (red triangles) in a MGCA sample treated with 750V/cm and 2 mA/mm². Modified form [187].

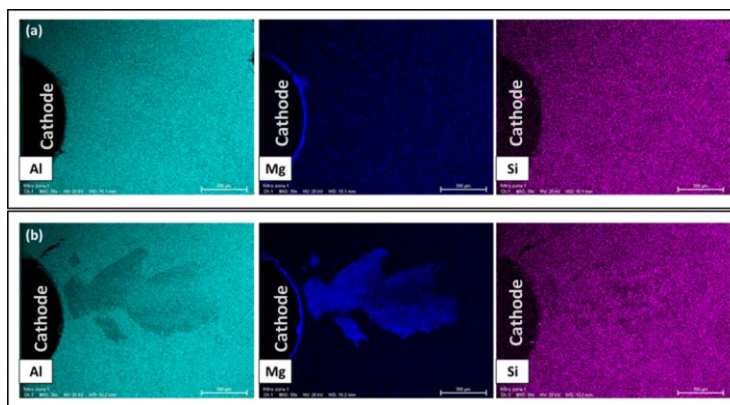


Figure 67: EDS concentration maps for Al, Mg and Si in the cathodic area of a MgCA sample treated with 2 mA/mm² under 500 (a) and 1000V/cm (b). Taken form [187].

Additional information can be obtained by XRD analysis. The spectra collected on a MgGCA specimen treated using 1000 V/cm and 2 mA/mm² are reported in Figure 68. The spectra are referred to different areas of the sample: cathode, anode center of the gage section. One can observe that in the central part of the specimen the only crystalline phase present is corundum; this is in agreement with the microstructural results discussed in the previous section, which suggested that the glass was not crystallized during the treatment.

Conversely, in the anodic area the peaks of mullite are recorded and a small signal related to MgO·Al₂O₃ spinel can be observed. In this zone the glass was therefore, at least partially, crystallized. At the cathode mullite is still present; nevertheless, the main crystalline phase, excluding corundum, is the spinel. This is a result of the Mg migration toward the cathode, which lead to the formation of a MgO enriched area, allowing the spinel formation. The precipitation of the new phase could be accelerated by the presence of the melt and by the high temperature, which is probably reached close to the electrode as a result of current concentration.

Finally, it is possible to notice, in the spectrum collected close to the cathode, the presence a two small peaks that could be related to metallic silicon. Although quite limited, some blackened areas are present in this region; these are probably associated to a partial reduction of the material, which in some cases leads to a complete reduction of the silica glass. Obviously, the reduction starts from the less stable oxide and, according to Ellingham diagrams, silica is characterized by an higher free energy of formation when compared with alumina or magnesia[205], therefore it is "easier" to be reduced. This accounts for the fact that only for silicon the metallic specie is observed. The experimental results are therefore suggesting that at the cathode SiO₂ is progressively reduced and MgO reacts with Al₂O₃ forming the spinel.

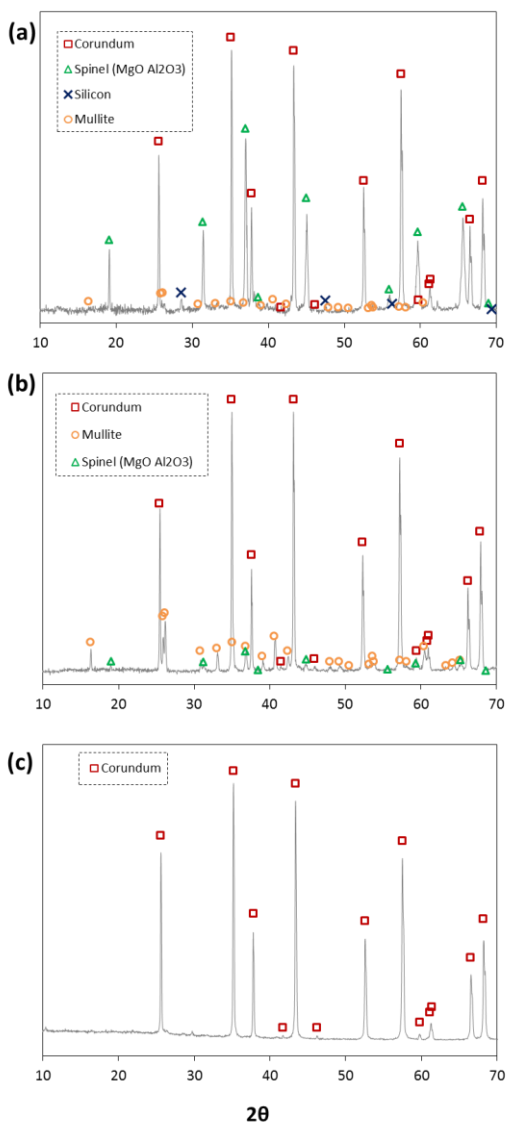
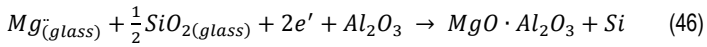
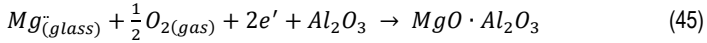
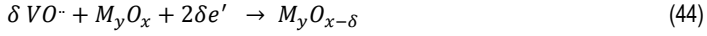


Figure 68: XRD spectra collected on the cathode (a), anode (b) and center of the gage section (c) on a MgGCA sample treated using 1000 V/cm and 2 mA/mm².

Several cathodic reactions, involving ionic species, can be proposed at metal-ceramic interface:



While at the anode could take place:



Additionally, an electronic contribution to conduction cannot be completely excluded, even if the activation energy during FS is in good agreement with ionic diffusion. So, the system is for sure very complex. Nevertheless, some consideration deserves to be proposed.

Reactions 43 and 44 could occur both on the glass and on alumina, similarly to what reported in the section regarding FS for pure alumina. These two reaction deals with the possible annihilation mechanism for charged oxygen vacancy: the first referred to a system in which the molecular oxygen reduction is enough fast, the latter referred to an oxygen deficient system leading to a partial reduction of the oxides.

Reactions 45 and 46 involves magnesium and explains spinel formation ($MgO \cdot Al_2O_3$). Reaction 45 is referred to a system in which Mg^{2+} reacts with gaseous oxygen and electrons in order to form MgO which is incorporated in the spinel structure. Nevertheless, while sintering is proceeding reaction 45 becomes progressively slower as a result of the decrease in surface area (the reaction with O_2

can take place only on the pores surface). Hence, the silica itself becomes a source of oxygen and the MgO formation happens at the expense of SiO₂. Silica is impoverished of oxygen and Si⁴⁺ is thus reduced by the electrons consumed at the cathode. It is nice to observe that the blackened areas in MgGCA sample were always located under the sample surface, within the specimen. In other words, the reduced areas are formed where molecular oxygen cannot be provided, preventing reaction 45 to occur, thus enhancing reaction 46.

Mg⁺⁺ motion toward the cathode (-) leads to the asymmetry observed in magnesium distribution (Figure 66, Figure 67) and to spinel formation (Figure 68). Yet, it is not completely clear how the glass structure is modified once that Mg⁺⁺ is removed from the vitreous reticulum. When the O-Mg-O ionic bond is broken, magnesium starts to move toward the negative electrode as a sort of positive interstitial in the glass. Nevertheless, this would lead to the formation of two adjacent non-bridging oxygen with negative charge. This structure is obviously unstable; therefore it could be stabilized if another Mg⁺⁺, coming from the positive electro side, falls between the two non-bridging oxygen. This mechanism could partially explain the behavior but it leaves two open points:

- i. The motion of each Mg⁺⁺ should be well coordinated with the other magnesium ions;
- ii. This mechanism is just shifting the problem closer to the electrodes.

Another possible mechanism is shown in Figure 69. This mechanism is derived from what reported by Varshneya [206] describing the structural rearrangement of the glassy structure when alkali ions are moving. In this case the two non-bridging oxygen with -1 charge collapse forming a bridging oxygen and a O²⁻ free ion which moves as an interstitial toward the anode. This anion would be oxidized in the anodic region forming molecular oxygen, according to Reaction 46.

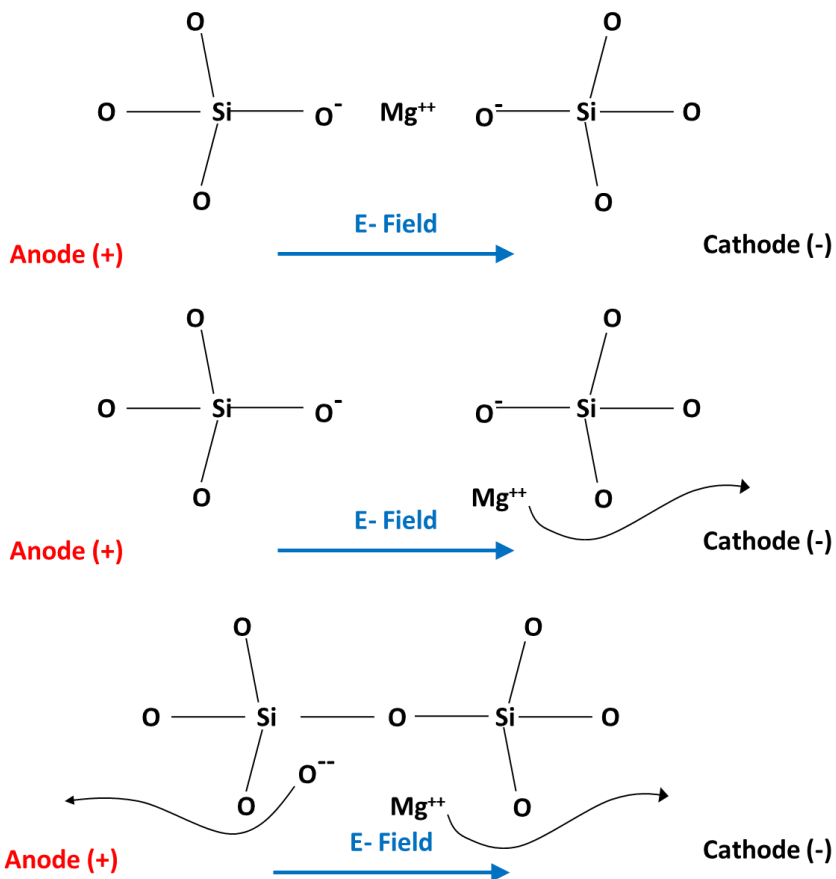


Figure 69: Structural rearrangement of glass structure during E-Field induced magnesium migration.

Yet, oxygen deficient structures can be formed during the process; this is a fact confirmed by the formation of the blackened areas. If we assume, similarly to what reported for pure alumina sample, that also in MgGCA different degree of reduction could be produced out from the black zone this could explain several open points. First, the absence of some oxygen ions can produced a wide series of defect which, in many cases, interrupt the glass chain structure[207]. This could lead to a change in the viscous properties of the glass and, reasonably, to a decrease in glass

viscosity which allows a fast densification. Therefore, the formation of non-stoichiometric SiO_2 could be at the base of the observed sintering behavior which cannot be accounted only by Joule heating (as reported in “4.2.1 Densification behavior and Microstructural Evolution”).

Additionally, it has been reported that oxygen-deficient silica is characterized by slower crystallization process when compared with stoichiometric SiO_2 [208,209]. This could account for the fact that mullite was formed close to the anode while in the central part of the gage section and the cathodic area the mullite signal is very weak. In fact, the oxygen vacancy migration toward the cathode and interstitial oxygen motion toward the anode lead to the formation of oxygen deficient-structures only far from the anodic area. The formation of non-stoichiometric SiO_2 can therefore explain both the crystallization and densification properties observed during FS experiments.

One final point deserves to be point out: the blackening behavior of MgGCA is asymmetric when compared with pure alumina. In fact, in pure alumina the blackening process started from the anode, whereas in glass-containing alumina it starts from the cathode (similarly to what reported for YSZ). This behavior has two different reasons:

- i. A central contribution to the formation of the blackened areas in MgGCA is given by Mg ions migration toward the cathode (-); this mechanism would not be observed in pure alumina.
- ii. The mobility of VO^\cdot in the glass is much higher than in crystalline corundum. This lead to the formation of an oxygen vacancy reach area close to the cathode (-) in MgGCA. Conversely, in pure alumina the conduction during FS is mainly electronic and, when a vacancy is produced at the anode (Reaction 47), it is suddenly reduced leading to the formation of the partially-reduced blackened structures.

In this chapter we showed that also in magnesia silicate glass-containing alumina the material can be partially reduced during DC flash sintering experiments. Such reduction presents features different from those observed in pure alumina: the

blackening in MgGCA is located at the cathode, while in pure alumina it starts from the anode. These results point out that the electrical characteristic of the system can strongly interact with this phenomenon, which can be at the base of the rapid mass transport phenomena observed in FS.

5 Conclusions

In this work we showed that flash sintering can be successfully applied also to insulating ceramics like α -alumina. In particular, 99.8% pure alumina can be flash sintered, achieving almost complete densification, at 900°C in 2 min using 1500 V/cm and 6 mA/mm². A further decrease of the firing temperature is obtained by using different conductive pastes at the metal electrode-ceramic interface. In particular, the use of silver paste or carbon-based cement allows a consistent reduction of the onset flash sintering temperature.

The applicability of flash sintering was also extended to magnesia-silicate glass-containing alumina. The results show that glass addition allows faster densification via liquid phase sintering mechanisms. The electric field/current application interact with the different stages of liquid phase sintering: it lowers the temperature at which particles rearrangement take place, this being associated with the vitreous phase softening. Nevertheless, the magnitude of the shrinkage related to this stage is almost independent from the field. Much more significant field/current effects can be observed at higher temperature when the system reaches the current limit. In this case, glass addition allows an almost instantaneous densification with modest power dissipation in the specimen.

The photoemission spectra obtained during the II and III stage of flash sintering are in all the cases coherent with a thermal radiation. The black body model represent the best interpretation for the optical phenomena during the flash event. These results shade some light on this point and provide a different interpretation from those actually available in the scientific literature, mainly based on electroluminescence.

A deep literature study allowed to point out strong affinities between flash sintering and dielectric breakdown in α -alumina. The analogies are both theoretical and phenomenological. The experimental results show that the flash event can be easily reproduced in porous alumina, rather than in dense specimens. This conclusion is in agreement with the behavior observed in dielectric breakdown experiments. Moreover, we show that during the incubation of flash sintering a pre-breakdown conduction behavior can be pointed out.

Singular phenomena were observed during flash sintering experiments: a drop of the activation energy for conduction (pure alumina), abnormal and oriented grain growth, formation of blackened areas and unusually fast mass transport phenomena and densification. A possible explanation could be based on electrolytic reaction during the flash process, which lead to the formation of a non-stoichiometric oxide. This explanation, confirmed by XPS and PL measurements, is coherent with the formation of partially reduced regions often observed in DC flash experiments.

6 Future Perspectives

This work provides an insight into the flash sintering behavior of commercially pure α -alumina and glass-containing alumina. It also provides a discussion about the possible mechanisms involved in flash sintering of oxide ceramics. However, it still lacks in the scale up the process toward an industrial application.

Future activities can be therefore focused on the definition of procedures and methodologies that allow an industrial application of this technology. The process based on the so called "travelling electrodes", sliding or rolling on the specimen, seems one of the most promising one.

Furthermore, other scientific points still deserves to be investigated. Among them, the atmosphere effect on the onset flash sintering temperature is one of the most interesting. I.e. it has been shown that the flash event in Ar is anticipated of hundreds degrees with respect to air; but it is still not clear if this is associated to a change of the material conductivity in inert atmosphere or to an interparticle plasma formation due to the low dielectric strength of argon. Tests in other inert atmospheres with different dielectric strength (like N₂) can shades some light on this point.

List of abbreviation and acronyms

AC	Alternate Current
CVD	Chemical Vapor Deposition
DC	Direct Current
ECAS	Electric Current-Assisted Sintering
EDS	Energy Dispersive X-ray Spectrometry
FAST	Field-Assisted Sintering Techniques
FE	Flash Event
FS	Flash Sintering
FSPS	Flash Spark Plasma Sintering
GCA	Glass-Containing Alumina
IR	Infrared
LSCF	Lanthanum-Strontium-Cobalt Ferrite
LVDT	Linear Variable Differential Transformer
MgGCA	Magnesia Silicate Glass-Containing Alumina
NIR	Near Infrared
PVD	Physical Vapor Deposition
SEM	Scanning Electron Microscopy
SIGCA	Silicate Glass-Containing Alumina
SPS	Spark Plasma Sintering
TEOS	Tetraethyl Orthosilicate
TRD	Thermo-Reactive Deposition
UV	Ultraviolet
VIS	Visible light
XPS	X-Ray Photoelectron Spectroscopy
XRD	X-Ray Diffraction
YSZ	Yttria-Stabilized Zirconia
ZAS	Zirconia-Alumina-Silica

References

- [1] J.-C. Boch, P.; Niepce, Ceramic materials, ISTE, Newport Beach, USA, 2007.
- [2] C.B. Carter, M.G. Norton, Ceramic Materials Science and Engineering, in: Int. Sci. Colloq. Model. Mater. Process., Springer, 2007.
- [3] M.N. Rahaman, Ceramic processing and sintering, Marcel Dekker, New York, USA, 1996.
- [4] European Comission, Reference Document on Best Available Techniques in the Ceramic Manufacturing Industry, (2007).
- [5] Confindustria, The Italian ceramic industry consist of 265 companies with 36,000 employees, (n.d.). <http://www.confindustriaceramica.it/site/en/home/articolo7818.html> (accessed October 18, 2016).
- [6] M. Cologna, B. Rashkova, R. Raj, Flash sintering of nanograin zirconia in <5 s at 850°C, *J. Am. Ceram. Soc.* 93 (2010) 3556–3559. doi:10.1111/j.1551-2916.2010.04089.x.
- [7] M. Cologna, A.L.G. Prette, R. Raj, Flash-sintering of cubic yttria-stabilized zirconia at 750°C for possible use in SOFC manufacturing, *J. Am. Ceram. Soc.* 94 (2011) 316–319.
- [8] J.A. Downs, V.M. Sglavo, Electric field assisted sintering of cubic zirconia at 390°C, *J. Am. Ceram. Soc.* 96 (2013) 1342–1344.
- [9] J. Downs, Mechanisms of Flash Sintering in Cubic Zirconia, University of Trento, 2013. <http://eprints-phd.biblio.unitn.it/976/>.
- [10] Cutting-Edge Flash-Sintering Technology, (n.d.). <http://www.fastceramics.com/innovative-research.html> (accessed October 28, 2016).
- [11] E. Zapata-Solvas, D. Gómez-García, A. Domínguez-Rodríguez, R.I. Todd, Ultra-fast and energy-efficient sintering of ceramics by electric current concentration, *Sci. Rep.* 5 (2015) 8513.
- [12] N. Shomrat, S. Baltianski, C.A. Randall, Y. Tsur, Flash sintering of potassium-niobate, *J. Eur. Ceram. Soc.* 35 (2015) 2209–2213.
- [13] S. Grasso, Y. Sakka, N. Rendtorff, C. Hu, G. Maizza, H. Borodianska, O. Vasykiv, Modeling of the temperature distribution of flash sintered zirconia, *J. Ceram. Soc. Japan.* 119 (2011) 144–146.
- [14] R.I. Todd, E. Zapata-Solvas, R.S. Bonilla, T. Sneddon, P.R. Wilshaw, Electrical characteristics of flash sintering: Thermal runaway of Joule heating, *J. Eur. Ceram. Soc.* 35 (2015) 1865–1877.
- [15] Y. Zhang, J. Il Jung, J. Luo, Thermal runaway, flash sintering and asymmetrical microstructural development of ZnO and ZnO-Bi₂O₃ under direct currents, *Acta Mater.* 94 (2015) 87–100.
- [16] M. Biesuz, P. Luchi, A. Quaranta, V.M. Sglavo, Theoretical and

- phenomenological analogies between flash sintering and dielectric breakdown in α -alumina, *J. Appl. Phys.* 120 (2016) 145107.
- [17] K. Terauds, J.M. Lebrun, H.H. Lee, T.Y. Jeon, S.H. Lee, J.H. Je, R. Raj, Electroluminescence and the measurement of temperature during Stage III of flash sintering experiments, *J. Eur. Ceram. Soc.* 35 (2015) 3195–3199.
- [18] J.M. Lebrun, R. Raj, A first report of photoemission in experiments related to flash sintering, *J. Am. Ceram. Soc.* 97 (2014) 2427–2430.
- [19] S.K. Jha, K. Terauds, J. Lebrun, R. Raj, Beyond flash sintering in 3 mol % yttria stabilized zirconia, *J. Ceram. Soc. Japan.* 124 (2016) 283–288.
- [20] K. Naik, S.K. Jha, R. Raj, Correlations between conductivity, electroluminescence and flash sintering, *Scr. Mater.* 118 (2016) 1–4.
- [21] S.K. Jha, J.M. Lebrun, K.C. Seymour, W.M. Kriven, R. Raj, Electric field induced texture in titania during experiments related to flash sintering, *J. Eur. Ceram. Soc.* 36 (2016) 257–261.
- [22] J.M. Lebrun, T.G. Morrissey, J.S.C. Francis, K.C. Seymour, W.M. Kriven, R. Raj, Emergence and Extinction of a New Phase during On-Off Experiments Related to Flash Sintering of 3YSZ, *J. Am. Ceram. Soc.* 98 (2015) 1493–1497.
- [23] E. Zapata-Solvas, S. Bonilla, P.R. Wilshaw, R.I. Todd, Preliminary investigation of flash sintering of SiC, *J. Eur. Ceram. Soc.* 33 (2013) 2811–2816.
- [24] Anshu Gaur, Flash-Sintering of MnCo_2O_4 and $(\text{La}, \text{Sr})(\text{Co}, \text{Fe})\text{O}_3$ Ceramics for Potential Application in SOFC, Dr. Thesis, Univ. Trento. (2014).
- [25] R. Muccillo, E.N.S. Muccillo, Shrinkage control of yttria-stabilized zirconia during ac electric field-assisted sintering, *J. Eur. Ceram. Soc.* 34 (2014) 3871–3877.
- [26] R. Muccillo, E.N.S. Muccillo, An experimental setup for shrinkage evaluation during electric field-assisted flash sintering : Application to yttria-stabilized zirconia, *J. Eur. Ceram. Soc.* 33 (2013) 515–520.
- [27] M. Biesuz, V.M. Sglavo, Field-assisted sintering of silicate glass-containing alumina, *Ceram. Eng. Sci. Proc.* 36 (2015) 75–81.
- [28] J.S.C. Francis, R. Raj, Influence of the field and the current limit on flash sintering at isothermal furnace temperatures, *J. Am. Ceram. Soc.* 96 (2013) 2754–2758.
- [29] J. Narayan, A new mechanism for field-assisted processing and flash sintering of materials, *Scr. Mater.* 69 (2013) 107–111.
- [30] R. Chaim, Liquid Film Capillary Mechanism for Densification of Ceramic Powders during Flash Sintering, *Materials (Basel)*. 9 (2016) 280.
- [31] G. Corapcioglu, M.A. Gulgun, K. Kisslinger, S. Sturm, S.K. Jha, R. Raj,

- Microstructure and microchemistry of flash sintered $K_{0.5}Na_{0.5}NbO_3$, *J. Ceram.* 124 (2016) 321–328.
- [32] M. Biesuz, G. Dell'Agli, L. Spiridigliozzi, C. Ferone, V.M. Sglavo, Conventional and field-assisted sintering of nanosized Gd-doped ceria synthesized by co-precipitation, *Ceram. Int.* 42 (2016) 11766–11771.
- [33] X. Hao, Y. Liu, Z. Wang, J. Qiao, K. Sun, A novel sintering method to obtain fully dense gadolinia doped ceria by applying a direct current, *J. Power Sources.* 210 (2012) 86–91.
- [34] A. Akbari-Fakhrabadi, R. V. Mangalaraja, F.A. Sanhueza, R.E. Avila, S. Ananthakumar, S.H. Chan, Nanostructured Gd-CeO₂ electrolyte for solid oxide fuel cell by aqueous tape casting, *J. Power Sources.* 218 (2012) 307–312.
- [35] S. Ghosh, A.H. Chokshi, P. Lee, R. Raj, A huge effect of weak dc electrical fields on grain growth in zirconia, *J. Am. Ceram. Soc.* 92 (2009) 1856–1859.
- [36] J. Narayan, Grain growth model for electric field-assisted processing and flash sintering of materials, *Scr. Mater.* 68 (2013) 785–788.
- [37] T.B. Holland, U. Anselmi-Tamburini, D. V. Quach, T.B. Tran, A.K. Mukherjee, Effects of local Joule heating during the field assisted sintering of ionic ceramics, *J. Eur. Ceram. Soc.* 32 (2012) 3667–3674.
- [38] J.S.C. Francis, M. Cologna, D. Montinaro, R. Raj, Flash sintering of anode-electrolyte multilayers for SOFC applications, *J. Am. Ceram. Soc.* 96 (2013) 1352–1354.
- [39] M. Cologna, J.S.C. Francis, R. Raj, Field assisted and flash sintering of alumina and its relationship to conductivity and MgO-doping, *J. Eur. Ceram. Soc.* 31 (2011) 2827–2837.
- [40] R. Raj, M. Cologna, J.S.C. Francis, Influence of externally imposed and internally generated electrical fields on grain growth, diffusional creep, sintering and related phenomena in ceramics, *J. Am. Ceram. Soc.* 94 (2011) 1941–1965.
- [41] K.S. Naik, V.M. Sglavo, R. Raj, Flash sintering as a nucleation phenomenon and a model thereof, *J. Eur. Ceram. Soc.* 34 (2014) 4063–4067.
- [42] J. Janek, C. Korte, Electrochemical blackening of yttria-stabilized zirconia – morphological instability of the moving reaction front, *Solid State Ionics.* 116 (1999) 181–195.
- [43] C. Bonola, P. Camagni, P. Chiodelli, G. Samoggia, Study of defects introduced by electroreduction in YSZ, *Radiat. Eff. Defects Solids.* 119–121 (1991) 457–462. doi:10.1080/10420159108224920.
- [44] R. E. W. Casselton, Blackening in yttria stabilized zirconia due to cathodic processes at solid platinum electrodes, *J. Appl.*

- Electrochem. 4 (1974) 25–48.
- [45] H.P.B. D. S. THORP, The dielectric constants of current- blackened single crystal yttria-stabilized zirconia, *J. Mater. Sci.* 8 (1973) 1401–1408.
- [46] F.K. Moghadam, T. Yamashita, D.A. Stevenson, Characterization of the current-blackening phenomena in scandia stabilized zirconia using transmission electron microscopy, *J. Mater. Sci.* 18 (1983) 2255–2259.
- [47] R. Muccillo, M. Kleitz, E.N.S. Muccillo, Flash grain welding in yttria stabilized zirconia, *J. Eur. Ceram. Soc.* 31 (2011) 1517–1521.
- [48] W. Qin, H. Majidi, J. Yun, K. van Benthem, Electrode Effects on Microstructure Formation During FLASH Sintering of Yttrium-Stabilized Zirconia, *J. Am. Ceram. Soc.* 99 (2016) 2253–2259.
- [49] S.W. Kim, S.G. Kim, J. Il Jung, S.J.L. Kang, I.W. Chen, Enhanced grain boundary mobility in yttria-stabilized cubic zirconia under an electric current, *J. Am. Ceram. Soc.* 94 (2011) 4231–4238.
- [50] I.-W.C. Pei-Lin Chen, Grain boundary mobility in Y2O3 defect mechanism and dopant effects.pdf, *J. Am. Ceram. Soc.* 79 (1996) 1801–1809.
- [51] P. Chen, I. Chen, Role of Defect Interaction in Boundary Mobility and Cation Diffusivity of CeO₂, *J. Am. Ceram. Soc.* 77 (1994) 2289–97. doi:10.1111/j.1151-2916.1994.tb04596.x.
- [52] J.G.P. da Silva, H.A. Al-Qureshi, F. Keil, R. Janssen, A dynamic bifurcation criterion for thermal runaway during the flash sintering of ceramics, *J. Eur. Ceram. Soc.* 36 (2016) 1261–1267.
- [53] Y. Dong, I.-W. Chen, Predicting the Onset of Flash Sintering, *J. Am. Ceram. Soc.* 98 (2015) 2333–2335. doi:10.1111/jace.13679.
- [54] Y. Dong, I.W. Chen, Onset Criterion for Flash Sintering, *J. Am. Ceram. Soc.* 98 (2015) 3624–3627.
- [55] M. Biesuz, V.M. Sglavo, Flash sintering of alumina: Effect of different operating conditions on densification, *J. Eur. Ceram. Soc.* 36 (2016) 2535–2542.
- [56] E. Bichaud, J.M. Chaix, C. Carry, M. Kleitz, M.C. Steil, Flash sintering incubation in Al₂O₃/TZP composites, *J. Eur. Ceram. Soc.* 35 (2015) 2587–2592.
- [57] C.E.J. Dancer, Flash sintering of ceramic materials, *Mater. Res. Express.* 3 (2016) 102001.
- [58] A. Karakuscu, M. Cologna, D. Yarotski, J. Won, J.S.C. Francis, R. Raj, B.P. Uberuaga, Defect structure of flash-sintered strontium titanate, *J. Am. Ceram. Soc.* 95 (2012) 2531–2536.
- [59] T. Jiang, Z. Wang, J. Zhang, X. Hao, D. Rooney, Y. Liu, W. Sun, J. Qiao, K. Sun, Understanding the flash sintering of rare-earth-doped ceria for solid oxide fuel cell, *J. Am. Ceram. Soc.* 98 (2015) 1717–1723.

- [60] A.L.G. Prette, M. Cologna, V. Sglavo, R. Raj, Flash-sintering of Co₂MnO₄ spinel for solid oxide fuel cell applications, *J. Power Sources*. 196 (2011) 2061–2065.
- [61] TEDLA YESHITILA ALEMU, Thickness effect in flash sintering behavior of Mn (Co , Fe) 2 O 4 for effective SOFC Interconnect Coating Acknowledgement, University of Trento, 2014.
- [62] J.S.C.Francis, M. Cologna, R. Raj, Particle size effects in flash sintering, *J. Am. Ceram. Soc.* 95 (2012) 138–146.
- [63] J.S.C. Francis, R. Raj, Flash-sinterforging of nanograin zirconia: Field assisted sintering and superplasticity, *J. Am. Ceram. Soc.* 95 (2012) 138–146.
- [64] Y. Zhang, J. Luo, Promoting the flash sintering of ZnO in reduced atmospheres to achieve nearly full densities at furnace temperatures of 120°C, *Scr. Mater.* 106 (2015) 26–29.
- [65] R. Raj, Joule heating during flash-sintering, *J. Eur. Ceram. Soc.* 32 (2012) 2293–2301.
- [66] J. Park, I.W. Chen, In situ thermometry measuring temperature flashes exceeding 1,700°C in 8 mol% Y₂O₃-stabilized zirconia under constant-voltage heating, *J. Am. Ceram. Soc.* 96 (2013) 697–700.
- [67] H. Yoshida, K. Morita, B.N. Kim, Y. Sakka, T. Yamamoto, Reduction in sintering temperature for flash-sintering of yttria by nickel cation-doping, *Acta Mater.* 106 (2016) 344–352.
- [68] A. Gaur, V.M. Sglavo, Flash-sintering of MnCo₂O₄ and its relation to phase stability, *J. Eur. Ceram. Soc.* 34 (2014) 2391–2400.
- [69] H. Yoshida, Y. Sakka, T. Yamamoto, J.M. Lebrun, R. Raj, Densification behaviour and microstructural development in undoped yttria prepared by flash-sintering, *J. Eur. Ceram. Soc.* 34 (2014) 991–1000.
- [70] Mikron, Table of emissivity of various surfaces, (n.d.). http://www-eng.lbl.gov/~dw/projects/DW4229_LHC_detector_analysis/calculations/emissivity2.pdf.
- [71] J.-M. Lebrun, S.K. Jha, W.M. Kriven, R. Raj, Broadening of Diffraction Peak Widths and Temperature Non-Uniformity during Flash Sintering Experiments, *J. Am. Ceram. Soc.* (2015) 1–6.
- [72] R. Baraki, S. Schwarz, O. Guillon, Effect of electrical field/current on sintering of fully stabilized zirconia, *J. Am. Ceram. Soc.* 95 (2012) 75–78.
- [73] M.C. Steil, D. Marinha, Y. Aman, J.R.C. Gomes, M. Kleitz, From conventional ac flash-sintering of YSZ to hyper-flash and double flash, *J. Eur. Ceram. Soc.* 33 (2013) 2093–2101.
- [74] I.J. Hewitt, A.A. Lacey, R.I. Todd, A Mathematical Model for Flash Sintering, *Math. Model. Nat. Phenom.* (2015) 1–16.
- [75] M. Cologna, R. Raj, Surface diffusion-controlled neck growth kinetics in early stage sintering of zirconia, with and without

- applied DC electrical field, *J. Am. Ceram. Soc.* 94 (2011) 391–395.
- [76] A. Gaur, V.M. Sglavo, Densification of La_{0.6}Sr_{0.4}Co_{0.2}Fe_{0.8}O₃ ceramic by flash sintering at temperature less than 100 °C, *J. Mater. Sci.* 49 (2014) 6321–6332.
- [77] V. Esposito, E. Traversa, Design of Electroceramics for Solid Oxides Fuel Cell Applications: Playing with Ceria, *J. Am. Ceram. Soc.* 91 (2008) 1037–1051.
- [78] W. Lerdprom, R.K. Chinnam, D.D. Jayaseelan, W.E. Lee, Porcelain production by direct sintering, *J. Eur. Ceram. Soc.* 36 (2016) 4319–4325.
- [79] J. Rufner, D. Anderson, K. Van Benthem, R.H.R. Castro, Synthesis and Sintering Behavior of Ultrafine (< 10 nm) Magnesium Aluminate Spinel Nanoparticles, *J. Am. Ceram. Soc.* 96 (2013) 2077–2085.
- [80] D.E. Garcia, J. Seidel, R. Janssen, N. Claussen, Fast Firing of Alumina, *J. Eur. Ceram. Soc.* 15 (1995) 935–938.
- [81] J.C. M’Peko, J.S.C. Francis, R. Raj, Field-assisted sintering of undoped BaTiO₃: Microstructure evolution and dielectric permittivity, *J. Eur. Ceram. Soc.* 34 (2014) 3655–3660.
- [82] K.S. Naik, V.M. Sglavo, R. Raj, Field assisted sintering of ceramic constituted by alumina and yttria stabilized zirconia, *J. Eur. Ceram. Soc.* 34 (2014) 2435–2442.
- [83] R. Muccillo, E.N.S. Muccillo, Electric field-assisted flash sintering of tin dioxide, *J. Eur. Ceram. Soc.* 34 (2014) 915–923.
- [84] H. Gao, T.J. Asel, J.W. Cox, Y. Zhang, J. Luo, L.J. Brillson, Native point defect formation in flash sintered ZnO studied by depth-resolved cathodoluminescence spectroscopy, *J. Appl. Phys.* 120 (2016) 105302.
- [85] Y. Du, A.J. Stevenson, D. Vernat, M. Diaz, D. Marinha, Estimating Joule heating and ionic conductivity during flash sintering of 8YSZ, *J. Eur. Ceram. Soc.* 36 (2016) 749–759.
- [86] J.C. M’Peko, J.S.C. Francis, R. Raj, Impedance spectroscopy and dielectric properties of flash versus conventionally sintered yttria-doped zirconia electroceramics viewed at the microstructural level, *J. Am. Ceram. Soc.* 96 (2013) 3760–3767.
- [87] D. Liu, J. Liu, Y. Gao, F. Liu, K. Li, J. Xia, Y. Wang, L. An, Effect of the applied electric field on the microstructure and electrical properties of flash-sintered 3YSZ ceramics, *Ceram. Int.* (2016).
- [88] R. Raj, Analysis of the Power Density at the Onset of Flash Sintering, *J. Am. Ceram. Soc.* 99 (2016) 3226–3232.
- [89] H.-D. Wiemhofer, U. Vohrer, Spectroscopy and Thermodynamics of Electrons in Yttria-Stabilized Zirconia, *Ber. Bunsenges. Phys. Chem.* 96 (1992) 1646–1652.
<http://onlinelibrary.wiley.com/doi/10.1002/bbpc.19920961123/ab>

- stract.
- [90] V.R. Paiverneker, A.N. Petelin, F.J. Crowne, D.C. Nagle, Color-center-induced band-gap shift in yttria-stabilized zirconia, *Phys. Rev. B.* 40 (1989) 8555–8557.
- [91] S. Heiroth, R. Ghisleni, T. Lippert, J. Michler, A. Wokaun, Optical and mechanical properties of amorphous and crystalline yttria-stabilized zirconia thin films prepared by pulsed laser deposition, *Acta Mater.* 59 (2011) 2330–2340.
- [92] R. Muccillo, E.N.S. Muccillo, Light emission during electric field-assisted sintering of electroceramics, *J. Eur. Ceram. Soc.* 35 (2015) 1653–1656.
- [93] M. Gaft, R. Reisfeld, G. Panczer, *Modern Luminescence Spectroscopy of Minerals and Materials, II*, Springer Mineralogy, 2015.
- [94] J.H. Lienhard IV, J.H. Lienhard V, *A heat transfer textbook, III*, Phlogiston Press, 2008.
- [95] J.I. Eldridge, C.M. Spuckler, K.W. Street, J.R. Markham, Infrared radiative properties of yttria-stabilized zirconia thermal barrier coatings, *Ceram. Eng. Sci. Proc.* 23 (2002) 417–430.
- [96] W.W. Coblenz, Selective radiation from the Nernst glower, *Bull. Bur. Stand.* 4 (1908) 533–551.
- [97] O. Vasylykiv, H. Borodianska, Y. Sakka, D. Demirskyi, Flash spark plasma sintering of ultrafine yttria-stabilized zirconia ceramics, *Scr. Mater.* 121 (2016) 32–36. doi:10.1016/j.scriptamat.2016.04.031.
- [98] D. Liu, Y. Gao, J. Liu, F. Liu, K. Li, H. Su, Y. Wang, L. An, Preparation of Al₂O₃ – Y₃Al₅O₁₂ – ZrO₂ eutectic ceramic by flash sintering, *Scr. Mater.* 114 (2016) 108–111.
- [99] R. Muccillo, E.N.S. Muccillo, M. Kleitz, Densification and enhancement of the grain boundary conductivity of gadolinium-doped barium cerate by ultra fast flash grain welding, *J. Eur. Ceram. Soc.* 32 (2012) 2311–2316.
- [100] L.B. Caliman, R. Bouchet, D. Gouvea, P. Soudant, M.C. Steil, Flash sintering of ionic conductors: The need of a reversible electrochemical reaction, *J. Eur. Ceram. Soc.* 36 (2016) 1253–1260.
- [101] H. Yoshida, A. Uehashi, T. Tokunaga, Formation of grain boundary second phase in BaTiO₃ polycrystal under a high DC electric field at elevated temperatures, *J. Ceram.* 124 (2016) 388–392.
- [102] T. Jiang, Y. Liu, Z. Wang, W. Sun, J. Qiao, K. Sun, An improved direct current sintering technique for proton conductor - BaZr_{0.1}Ce_{0.7}Y_{0.1}Yb_{0.1}O₃: The effect of direct current on sintering process, *J. Power Sources.* 248 (2014) 70–76.
- [103] L.M. Jesus, R.S. Silva, R. Raj, J.C. M'Peko, Electric field-assisted flash sintering of CaCu₃Ti₄O₁₂: Microstructure characteristics and dielectric properties, *J. Alloys Compd.* 682 (2016) 753–758.

- [104] I. Bajpai, Y. Han, J. Yun, J. Francis, S. Kim, I. Bajpai, Y. Han, J. Yun, J. Francis, S. Kim, R. Raj, Preliminary investigation of hydroxyapatite microstructures prepared by flash sintering, *Adv. Appl. Ceram.* 115 (2016) 276–281. doi:10.1080/17436753.2015.1136777.
- [105] Y. Zhang, J. Nie, J. Luo, Effects of phase and doping on flash sintering of TiO₂, *J. Ceram. Soc. Japan.* 124 (2016) 296–300.
- [106] D. Liu, Y. Gao, J. Liu, K. Li, F. Liu, Y. Wang, SiC whisker reinforced ZrO₂ composites prepared by flash-sintering, *J. Eur. Ceram. Soc.* 36 (2016) 2051–2055.
- [107] S.K. Jha, R. Raj, The effect of electric field on sintering and electrical conductivity of Titania, *J. Am. Ceram. Soc.* 97 (2014) 527–534.
- [108] S.K. Jha, R. Raj, Electric Fields Obviate Constrained Sintering, *J. Am. Ceram. Soc.* 97 (2014) 3103–3109. doi:10.1111/jace.13136.
- [109] C. Schmerbauch, J. Gonzalez-julian, R. Roder, C. Ronning, O. Guillon, Flash Sintering of Nanocrystalline Zinc Oxide and its Influence on Microstructure and Defect Formation, *J. Am. Ceram. Soc.* 97 (2014) 1728–1735.
- [110] S. Grasso, E.Y. Kim, T. Saunders, M. Yu, A. Tudball, S.H. Choi, M. Reece, Ultra-Rapid Crystal Growth of Textured SiC Using Flash Spark Plasma Sintering Route, *Cryst. Growth Des.* 16 (2016) 2317–2321.
- [111] S. Grasso, T. Saunders, H. Porwal, B. Milsom, A. Tudball, M. Reece, Flash Spark Plasma Sintering (FSPS) of alpha and beta SiC, *J. Am. Ceram. Soc.* 95 (2016) 1534–1543.
- [112] C. Wang, D. Wu, S. Grasso, T. Saunders, E. Castle, H. Yan, M.J. Reece, Growth of SiC platelets using contactless flash technique, *J. Ceram. Soc. Japan.* 124 (2016) 845–847.
- [113] B. Niu, F. Zhang, J. Zhang, W. Ji, W. Wang, Z. Fu, Ultra-fast densification of boron carbide by flash spark plasma sintering, *Scr. Mater.* 116 (2016) 127–130. doi:10.1016/j.scriptamat.2016.02.012.
- [114] T. Saunders, S. Grasso, M.J. Reece, Ultrafast-Contactless Flash Sintering using Plasma Electrodes, *Sci. Rep.* 6:27222 (2016) 1–6. doi:10.1038/srep27222.
- [115] V.M. Candelario, R. Moreno, R.I. Todd, A.L. Ortiz, Liquid-phase assisted flash sintering of SiC from powder mixtures prepared by aqueous colloidal processing, *J. Eur. Ceram. Soc.* 37 (2017) 485–498.
- [116] E.A. Olevsky, S.M. Rolfing, A.L. Maximenko, Flash (Ultra-Rapid) Spark-Plasma Sintering of Silicon Carbide, *Sci. Rep.* 6 (2016) 33408.
- [117] S. Grasso, T. Saunders, H. Porwal, O. Cedillos-Barraza, D.D. Jayaseelan, W.E. Lee, M.J. Reece, Flash spark plasma sintering (FSPS) of pure ZrB₂, *J. Am. Ceram. Soc.* 97 (2014) 2405–2408.
- [118] J.G. Julian, J. Kevin, K. Speer, L. Liu, R. Jan, M. Knapp, H. Ehrenberg,

- M. Bram, O. Guillon, Effect of internal current flow during the sintering of zirconium diboride by Field Assisted Sintering Technology, *J. Am. Ceram. Soc.* 99 (2016) 35–42.
- [119] C. McLaren, W. Heffner, R. Tessarollo, R. Raj, H. Jain, Electric field-induced softening of alkali silicate glasses, *Appl. Phys. Lett.* 107 (2015) 184101.
- [120] J. Gonzalez-Julian, O. Guillon, Effect of Electric Field/Current on Liquid Phase Sintering, *J. Am. Ceram. Soc.* 98 (2015) 2018–2027. doi:10.1111/j.1527-0901.2015.03111.x
- [121] S. Grasso, T.G. Saunders, Spark plasma sintering in a flash, *Am. Ceram. Soc. Bull.* 95 (2016) 32–34.
- [122] E. Castle, R. Sheridan, S. Grasso, A. Walton, M. Reece, Rapid sintering of anisotropic, nanogained Nd-Fe-B by flash-spark plasma sintering, *J. Magn. Mater.* 417 (2016) 279–283.
- [123] M. Yu, S. Grasso, R. Mckinnon, T. Saunders, M. Reece, Review of flash sintering : Materials , Mechanisms and Modelling, *Adv. Appl. Ceram. Struct. , Funct. Bioceram.* (2016).
- [124] D. Yang, R. Raj, H. Conrad, Enhanced sintering rate of zirconia (3Y-TZP) through the effect of a weak dc electric field on grain growth, *J. Am. Ceram. Soc.* 93 (2010) 2935–2937.
- [125] D. Yang, H. Conrad, Enhanced sintering rate of zirconia (3Y-TZP) by application of a small AC electric field, *Scr. Mater.* 63 (2010) 328–331.
- [126] S.K. Jha, J.M. Lebrun, R. Raj, Phase transformation in the alumina-titania system during flash sintering experiments, *J. Eur. Ceram. Soc.* 36 (2016) 733–739. doi:10.1016/j.jeurceramsoc.2015.10.006.
- [127] M. Sutcu, Development of Dense Ceramic Tiles from Mixtures of Alumina Powders with Different PSD, Izmir Institute of Technology, 2004.
- [128] S.I. Bae, S. Baik, Determination of Critical Concentrations of silica and/or calcia for abnormal grain growth in alumina, *J. Am. Ceram. Soc.* 76 (1993) 1065–1067.
- [129] I. Bae, S. Baik, Abnormal Grain Growth of Alumina, *J. Am. Ceram. Soc.* 80 (1997) 1149–1156.
- [130] C. Greskovich, J.A. Brewer, Solubility of Magnesia in Polycrystalline Alumina at High Temperatures, *J. Am. Ceram. Soc.* 84 (2004) 420–425.
- [131] N.D.M. Hine, W.M.C. Foulkes, M.W. Finnis, a H. Heuer, Bulk Diffusion in Alumina : Solving the Corundum Conundrum, (n.d.). http://www.tcm.phy.cam.ac.uk/~mdt26/esdg_slides/hine030609.pdf.
- [132] A. Tewari, U. Aschauer, P. Bowen, Atomistic modeling of effect of Mg on oxygen vacancy diffusion in α -alumina, *J. Am. Ceram. Soc.* 97 (2014) 2596–2601.
- [133] K.P.D. Lagerlof, R.W. Grimes, The Defect Chemistry of Sapphire,

- Acta Mater. 46 (1998) 5689–5700.
- [134] R.W. Rice, Mechanical properties of ceramics and composites, Marcel Dekker, New York, USA, 2000.
- [135] A.M. WITTENBER, Total Hemispherical Emissivity of Sapphire, J. Opt. Soc. Am. 55 (1965) 432–435.
- [136] Emissivity Coefficients of some common Materials, (n.d.). http://www.engineeringtoolbox.com/emissivity-coefficients-d_447.html (accessed October 17, 2016).
- [137] J. Pan, J. Öijerholm, B. Belonoshko, A. Rosengren, C. Leygraf, Self-diffusion activation energies in α -Al₂O₃ below 1000°C – measurements and molecular dynamics calculation, Philos. Mag. Lett. 84 (2004) 781–789.
- [138] Y. Oishi, W.D. Kingery, Self-diffusion of oxygen in single crystal and polycrystalline aluminum oxide, J. Chem. Phys. 33 (1960) 480–486.
- [139] J. Pappis, W.D. Kingery, Electrical Properties of Single-Crystal and Polycrystalline Alumina at High Temperatures, J. Am. Ceram. Soc. 44 (1961) 459–464.
- [140] P.J. Harrop, Self-diffusion in simple oxides (A bibliography), J. Mater. Sci. 3 (1968) 206–222.
- [141] S.K. Mohapatra, F.A. Kroger, Defect Structure of α -Al₂O₃ Doped with Magnesium, J. Am. Ceram. Soc. 60 (1977) 141–148.
- [142] J. Öijerholm, J. Pan, C. Leygraf, In-situ measurements by impedance spectroscopy of highly resistive α -alumina, Corros. Sci. 48 (2006) 243–257.
- [143] H.A. Rahnamaye Alibad, S.R. Ghorbani, Structural and Spin Polarization Effects of Cr, Fe and Ti Elements on Electrical Properties of α -Al₂O₃ by First Principle Calculations, J. Mod. Phys. 2 (2011) 158–161.
- [144] H.A. Aliabad Rahnamaye, M.R. Benam, H. Arabshahi, Theoretical studies of the effect of Ti, Zr and Hf substitutions on the electronic properties of alpha-alumina, Int. J. Phys. Sci. 4 (2009) 437–442.
- [145] A.F. Lima, J.M. Dantas, M. V. Lalic, An ab-initio study of electronic and optical properties of corundum Al₂O₃ doped with Sc, Y, Zr, and Nb, J. Appl. Phys. 112 (2012) 93709.
- [146] I. Costina, R. Franchy, Band gap of amorphous and well-ordered Al₂O₃ on Ni₃Al(100), Appl. Phys. Lett. 78 (2001) 4139–4141.
- [147] R.J. BROOK, J. YEE, F.A. KRÖGER, Electrochemical Cells and Electrical Conduction of Pure and Doped Al₂O₃, J. Am. Ceram. Soc. 54 (1971) 444–451.
- [148] H.M. Kizilyalli, P.R. Mason, DC and AC electrical conduction in single crystal alumina, Phys. Status Solidi. 36 (1976) 499–508.
- [149] K. Kitazawa, R.L. Coble, Chemical Diffusion in Polycrystalline Al₂O₃ as Determined from Electrical Conductivity Measurements, J. Am. Ceram. Soc. 57 (1974) 250–253. d

- [150] K. Kitazawa, R.L. Coble, Electrical Conduction in Single Crystal and Polycrystalline Al₂O₃ at High Temperatures, *J. Am. Ceram. Soc.* 57 (1974) 245–250.
- [151] H.P.R. Frederikse, W.R. Hosler, High temperature electrical conductivity of aluminum oxide, in: *Mass Transp. Phenom. Ceram.*, 1975.
- [152] A.H. Heuer, Oxygen and aluminum diffusion in α -Al₂O₃: How much do we really understand?, *J. Eur. Ceram. Soc.* 28 (2008) 1495–1507.
- [153] A.E. Paladino, R.L. Colbe, Effect of Grain Boundaries on Diffusion-Controlled Processes in Aluminum Oxide, *J. Am. Ceram. Soc.* 46 (1963) 133–136.
- [154] T. Nakagawa, I. Sakaguchi, N. Shibata, K. Matsunaga, E. Al., Yttrium doping effect on oxygen grain boundary diffusion in α -Al₂O₃, 55 (2007) 6627–6633.
- [155] N.M. Tallan, H.C. Graham, Interfacial Polarization and Electrical Conductivity in Sapphire, *J. Am. Ceram. Soc.* 48 (1965) 512–516.
- [156] J.H. Harding, K.J.W. Atkinson, R.W. Grimes, Experiment and Theory of Diffusion in Alumina, *J. Am. Ceram. Soc.* 86 (2003) 554–559.
- [157] P.W.M. Jacobs, E.A. Kotomin, Defect energies for pure corundum and for corundum doped with transition metal ions, *Philos. Mag. A.* 68 (1993) 695–709.
- [158] Y. Oishi, K. Ando, Y. Kubota, Y. Oishi, K. Ando, Y. Kubota, Self-diffusion of oxygen in single crystal alumina, *J. Chem. Phys.* 73 (1980) 1410–1412.
- [159] D. Martin, D. Duprez, Mobility of Surface Species on Oxides . 1 . Isotopic Exchange of ¹⁸O₂ with ¹⁶O of SiO₂, Al₂O₃, ZrO₂, MgO, CeO₂, and CeO₂-Al₂O₃. Activation by Noble Metals. Correlation with Oxide Basicity, *J. Phys. Chemistry.* 100 (1996) 9429–9438.
- [160] W. Shin, W. Seo, K. Koumoto, Grain-boundary Grooves and Surface Diffusion in Polycrystalline Alumina Measured by Atomic Force Microscope, *J. Euro.* 18 (1998) 595–600.
- [161] I. Pozniak, A. Pechenkov, A. Shatunov, Electrical Conductivity Measurement of Oxides Melts, in: *Int. Sci. Colloq. Model. Mater. Process.*, Riga, 2006: pp. 155–160.
- [162] E.C. Kouroukla, I.K. Bailiff, I. Terry, L. Bowen, Luminescence characterisation of alumina substrates using cathodoluminescence microscopy and spectroscopy, *Radiat. Meas.* 71 (2014) 117–121.
- [163] M. Ghamnia, C. Jardin, M. Bouzlama, Luminescent centres F and F⁺ in α -alumina detected by cathodoluminescence technique, *J. Electron Spectros. Relat. Phenomena.* 133 (2003) 55–63.
- [164] I.I. Milman, E. V. Moiseykin, S. V. Nikiforov, S.G. Mikhailov, V.I. Solomonov, Luminescence properties of α -Al₂O₃ dosimetric crystals exposed to a high-current electron beam, *Radiat. Meas.* 38

- (2004) 443–446.
- [165] S. Oss, L.M. Gratton, T. Lopez-Arias, Spark spectroscopy and the emission spectrum of air made easy, *Phys. Educ.* 426 (2013) 426–429.
- [166] M. Fujimoto, *Physics of classical electromagnetism*, Springer, 2007.
- [167] T.B. Holland, U. Anselmi-Tamburini, D. V. Quach, T.B. Tran, A.K. Mukherjee, Local field strengths during early stage field assisted sintering (FAST) of dielectric materials, *J. Eur. Ceram. Soc.* 32 (2012) 3659–3666.
- [168] J. Frenkel, On Pre-Breakdown Phenomena in Insulators and Electronic Semi-Conductors, *Phys. Rev.* 54 (1938) 647–648.
- [169] L.A. Dissado, C. Fothergill, *Electrical Degradation and Breakdown in Polymers* Electrical Degradation and Breakdown in Polymers, Peter Peregrinus Ltd., London, UK, 2008.
- [170] A. Zafar, Z. Imran, M. Rafiq, M. Hasan, Evidence of Pool-Frankel conduction mechanism in Sr-doped Lanthanum Ferrite La_{1-x}Sr_xFeO₃ (0 ≤ x ≤ 1) system, *Electron. Commun. Photonics Conf. (SIEPCPC)*. 3 (2011) 1–4.
- [171] H.K. Kim, F.G. Shi, Thickness Dependent Dielectric Strength of a Low-permittivity Dielectric Film, *IEEE Trans. Dielectr. Electr. Insul.* 8 (2001) 248–252.
- [172] P. Auerkari, *Mechanical and physical properties of engineering alumina ceramics*, VTT, 1996.
- [173] M. Yoshimura, H.K. Bowen, Electrical Breakdown Strength of Alumina at High Temperatures, *J. Am. Ceram. Soc.* 64 (1981) 404–410.
- [174] J.F. Verweij, J.H. Klootwijk, Dielectric breakdown I: A review of oxide breakdown, *Microelectronics J.* 27 (1996) 611–622.
- [175] S. Yamamichi, A. Yamamichi, D. Park, T. King, C. Hu, Impact of Time Dependent Dielectric Breakdown and Stress-Induced Leakage Current on the Reliability of High Dielectric Constant (Ba , Sr) TiO Thin-Film Capacitors for Gbit-Scale DRAM ' s, *IEEE Trans. Electron Devices.* 46 (1999) 342–347.
- [176] D. Pei, M.T. Nichols, S.W. King, J.S. Clarke, Y. Nishi, J.L. Shohet, D. Pei, M.T. Nichols, S.W. King, J.S. Clarke, using mercury and solid metal probes Time-dependent dielectric breakdown measurements of porous organosilicate glass using mercury and solid metal probes, *J. Vac. Sci. Technol. A.* 32 (2014) 51509.
- [177] H. Miyazawa, J. Okada, On the breakdown of alumina at higher temperature, *J. Phys. Soc. Japan.* 6 (1951) 55–59.
- [178] R. Gerson, T.C. Marshall, Dielectric Breakdown of Porous Ceramics, *J. Appl. Phys.* 30 (1959) 1650.
- [179] O. Jongprateep, V. Petrovsky, F. Dogan, Effects of Yttria Concentration and Microstructure on Electric Breakdown of Yttria

- Stabilized Zirconia, *J. Met. Mater. Miner.* 18 (2008) 9–14.
- [180] K. Vanstreels, I. Ciofi, Y. Barbarin, M. Baklanov, Influence of porosity on dielectric breakdown of ultralow-k dielectrics Influence o, *J. Vac. Sci. Technol. B.* 31 (2013) 50604.
- [181] R.W. Rice, *Porosity of ceramics*, Marcel Dekker, 1998.
- [182] R. Riedel, C. IW, *Ceramics Science and Technology: Vol. 1 Structures*, 2008.
- [183] D.R. Lide, *Handbook of chemistry and physics*, CRC Press, 2004.
- [184] M.N. Avadhanulu, P.G. Kshirdagar, *A Textbook of Engineering Physics*, S.Chand & Co. Ltd., New Delhi, India, 2013.
- [185] L. Badrour, E.G. Moya, J. Bernardini, F. Moya, Fast diffusion of silver in single and polycrystals of α -alumina, *J. Phys. Chem. Solids.* 50 (1989) 551–561.
- [186] E.G. Gontier-Moya, J. Bernardini, F. Moya, Silver and platinum diffusion in alumina single crystals, *Acta Mater.* 49 (2001) 637–644.
- [187] M. Biesuz, V.M. Sglavo, Liquid phase flash sintering in magnesia silicate glass-containing alumina, *J. Eur. Ceram. Soc.* 37 (2017) 705–713.
- [188] M.M. Seabaugh, I.H. Kerscht, G.L. Messing, Texture Development by Templated Grain Growth in Liquid Phase Sintered α -Alumina, *J. Am. Ceram. Soc.* 80 (1997) 1181–1188.
- [189] R. Freer, Diffusion in silicate minerals and glasses: A data digest and guide to the literature, *Contrib. to Mineral. Petrol.* 76 (1981) 440–454.
- [190] D.J. Cherniak, Diffusion in Quartz, Melilite, Silicate Perovskite, and Mullite, *Rev. Mineral. Geochemistry.* 72 (2010) 735–756.
- [191] M. Morioka, Cation diffusion in olivine-I. Cobalt and magnesium, *Geochim. Cosmochim. Acta.* 44 (1980) 759–762.
- [192] H. Bracht, E. Haller, R. Clark-Phelps, Silicon Self-Diffusion in Isotope Heterostructures, *Phys. Rev. Lett.* 81 (1998) 393–396.
- [193] T. Dunn, Oxygen diffusion in three silicate melts along the join diopside-anorthite, *Geochim. Cosmochim. Acta.* 46 (1982) 2293–2299.
- [194] K. Sunder, M. Grofmeier, R. Staskunaite, H. Bracht, Dynamics of Network Formers and Modifiers in Mixed Cation Silicate Glasses, *Zeitschrift Für Phys. Chemie.* 224 (2010) 1677–1705.
- [195] R.H. Doremus, *Glass Science*, Wiley, New York, USA, 1994.
- [196] R.J. Maurer, Deviations from Ohm’s law in Soda Lime Glass, *J. Chem. Phys.* 9 (1941) 579–584. doi:10.1063/1.1750958.
- [197] <http://www.engineering.com/Library/ArticlesPage/tabid/85/ArticleID/151/> (accessed November 2, 2016).
- [198] E.C. Guyer, *Handbook of Applied Thermal Design*, Hamilton Printing, Castleton, NY, USA, 1999.
- [199] F. Kreith, *The CRC Handbook of Thermal Engineering*, CRC Press

- LLC, Danvers, USA, 2000.
- [200] Y. Oishi, R. Terai, H. Ueda, Oxygen diffusion in liquid silicates and relation to their viscosity, in: *Mater. Sci. Res.*, Plenum Press, New York, USA, 1975.
- [201] Y. Zhang, H. Ni, Y. Chen, Diffusion Data in Silicate Melts, *Rev. Mineral. Geochemistry*. 72 (2010) 311–408.
- [202] E.L. Williams, Diffusion of Oxygen in Fused Silica, *J. Am. Ceram. Soc.* 48 (1965) 190–194.
- [203] Y. Zhang, H. Ni, Diffusion of H, C, and O Components in Silicate Melts, *Rev. Mineral. Geochemistry*. 72 (2010) 171–225. doi:10.2138/rmg.2010.72.5.
- [204] C.E. Leshner, R.L. Hervig, D. Tinker, Self diffusion of network formers (silicon and oxygen) in naturally occurring basaltic liquid, *Geochim. Cosmochim. Acta*. 60 (1996) 405–413.
- [205] <http://image.slidesharecdn.com/ellinghamdiagram-120924085031-phpapp02/95/ellingham-diagram-1-728.jpg?cb=1348476684> (accessed November 2, 2016).
- [206] A.K. Varshneya, *Fundamentals of inorganic glasses*, Academic Press, Inc, 1994.
- [207] L. Skuja, Optically active oxygen-deficiency-related centers in amorphous silicon dioxide, *J. Non. Cryst. Solids*. 239 (1998) 16–48. doi:10.1016/S0022-3093(98)00720-0.
- [208] F.E. Wagstaff, K.J. Richards, Preparation and Crystallization Behavior of Oxygen-Deficient, *J. Am. Ceram. Soc.* 48 (1965) 382–383.
- [209] F.E. Wagstaff, Crystallization resistant vitreous silica formed by the addition of silicon to silica, 1968.

Scientific Production

- I. M. Biesuz, V. M. Sglavo, Chromium and vanadium carbide and nitride coatings obtained by TRD techniques on UNI 42CrMoS4 (AISI 4140) steel, *Surf. Coat. Tech.* 286 (2016) 319-326.
- II. M. Biesuz, G. Dell'Agli, L. Spiridigliozzi, C. Ferone, V.M. Sglavo, Conventional and field-assisted sintering of nanosized Gd-doped ceria synthesized by co-precipitation, *Ceram. Internationa* 42 (2016) 11766-11771.
- III. M. Biesuz, V.M. Sglavo, Flash sintering of alumina: Effect of different operating conditions on densification, *J. Eur. Ceram. Sos.* 36 (2016) 2535-2542.
- IV. M. Biesuz, V.M. Sglavo, Field Assisted Sintering of Silicate Glass-Containing Alumina" in *Ceram. Eng. Sci. Proc.* 36 [6] (2015) 75-81.
- V. L. Emanuelli, M. Biesuz, S. Libardi, P. Marconi, A. Molinari, Shot peening of a sintered Ni-Cu-Mo steel produced by diffusion bonded powders, *La Metallurgia Italiana*, 107 [3] (2015) 23-28.
- VI. M. Biesuz, P. Luchi, A. Quaranta, V.M. Sglavo, Theoretical and phenomenological analogies between flash sintering and dielectric breakdown in α -alumina, *J. Appl. Phys.* 120 (2016) 145107.
- VII. M. Biesuz, V.M. Sglavo, Liquid phase flash sintering in magnesia silicate glass-containing alumina, *J. Eur. Ceram. Soc.* 37 (2017) 705–713.
- VIII. M. Biesuz, V.M. Sglavo, Flash sintering of alumina and its microstructural evolution, *Ceram. Eng. Sci. Proc.* 37 (2016).

- IX. M. Biesuz, L. Spiridigliozi, M. Frasnelli, G. Dell'Agli, V.M. Sglavo, Rapid densification of Samarium-doped Ceria ceramic with nanometric grain size at 900–1100° C, *Mater. Lett.* 190 (2017) 17-19.
- X. L. Spiridigliozi, G. Dell'Agli, M. Biesuz, V. M. Sglavo, M. Pansini, Effect of the Precipitating Agent on the Synthesis and Sintering Behavior of 20 mol Sm-Doped Ceria, *Adv. Mater. Sci. Eng.* (2016).
- XI. L. Spiridigliozi, M. Biesuz, G. Dell'Agli, E. Di Bartolomeo, F. Zurloc, V.M. Sglavo, Microstructural and electrical investigation of flash sintered Gd/Sm-doped ceria, *J. Mater. Sci.* TO BE PUBLISHED (2017).

Participation to Congresses, Schools and Workshops

- I. "39th International Conference and Expo on Advanced Ceramics and Composites", Daytona, USA, 25-30th January 2015. Oral presentation given by Prof. V. M. Sglavo: M. Biesuz, V.M. Sglavo, "Field assisted sintering of Silicate Glass containing Alumina".
- II. "14th International Conference of the European Ceramic Society", Toledo, Spain, 21-25th June 2015. Oral presentation: M. Sglavo: M. Biesuz, V.M. Sglavo, "Field Assisted Sintering of Alumina-Silica Composites".
- III. "40th International Conference and Expo on Advanced Ceramics and Composites", Daytona, USA, 24-29th January 2016. Oral presentation: M. Sglavo: M. Biesuz, V.M. Sglavo, "Flash sintering of alumina".
- IV. Conference on "Fuel Cells Science and Technology", Glasgow, UK, 13-14 April 2016. Poster presentation given by Mr. L. Spiridigliozzi: L. Spiridigliozzi, M. Biesuz, G. Dell'Agli, E. Di Bartolomeo, V.M. Sglavo, "Flash Sintering of variously-doped ceria materials".
- V. ECI Conference on "Electric field assisted sintering and related phenomena far from equilibrium", Tomar, Portugal, 06-11th March 2016. Oral presentation: M. Sglavo: M. Biesuz, V.M. Sglavo, "Flash sintering of glass-containing alumina bodies".
- VI. Forum Nazionale Giovani Ricercatori INSTM, Ischia, Italy, 11-14th July 2016. Oral presentation: M. Sglavo: M. Biesuz, V.M. Sglavo, "Flash sintering of alumina".

Poster presentation: M. Sglavo: M. Biesuz, V.M. Sglavo, "Effect of glass addition on flash sintering of alumina".

Oral presentation given by Mr. L. Spiridigliozzi: L. Spiridigliozzi, M. Biesuz, G. Dell'Agli, V.M. Sglavo, E. Di Bartolomeo, "Effect of flash sintering on gadolinium-doped ceria".

- VII. VI International Workshop on Oxide-based Materials, Naples, Italy, 21st - 24th September 2016. Poster presentation given by Mr. L. Spiridigliozzi: L. Spiridigliozzi, M. Biesuz, G. Dell'Agli, V.M. Sglavo, E. Di Bartolomeo, "Flash sintering of ceria-based ceramics".
- VIII. La radiobiologia in INFN, Trento, ITALY, May 2016.
- IX. School on scientific writing and reading, prof. Trevor Day, Trento, Settembre 2016.
- X. Third Joint CNR-FBK-UNITN Workshop on: Electron Matter Interaction as a tool for Materials analysis: Theory and Experiment (EMI2015), Trento, Italy, 16th June 2015.

Teaching Activities

- I. September-December 2014: Lab activity tutor of the course of Ceramic Processing and Engineering, University of Trento, Master Course in Materials Engineering.
- II. September-December 2015: Lab activity tutor of the course of Ceramic Processing and Engineering, University of Trento, Master Course in Materials Engineering.
- III. September-December 2016: Lab activity tutor of the course of Ceramic Processing and Engineering, University of Trento, Master Course in Materials Engineering.
- IV. March-June 2016: Tutor of Physic 1 course, University of Trento, Bachelor Course in Civil Engineering.